QATAR UNIVERSITY

COLLEGE OF ENGINEERING

MODEL-BASED DIAGNOSTICS OF SIMULTANEOUS TOOTH CRACKS IN SPUR GEARS

BY

AHMED SAEED ABDELFATTAH MOHAMED IBRAHIM

A Thesis Submitted to the Faculty of
the College of Engineering
in Partial Fulfillment
of the Requirements
for the Degree of
Master of Science in Mechanical Engineering

January 2017

COMMITTEE PAGE

The members of the Committee approve the Thesis of Ahmed Ibrahim defended on 08/01/2017.

Dr. Sadok Sassi
Thesis Supervisor

Dr. Mustafa Arafa
Committee Member

Dr. Mohammed F. M. Hussein
Committee Member

Dr. Mohammad Roshun Paurobally
Committee Member

Approved:

Dr. Khalifa Al-Khalifa, Dean, College of Engineering

ABSTRACT

Ibrahim, Ahmed, S., Masters: January: [2017], Masters of Science in Mechanical Engineering

Title: Model-Based Diagnostics of Simultaneous Tooth Cracks in Spur Gears

Supervisor of Thesis: Sadok, Sassi.

This study aims at developing a numerical model that could be used to simulate the effect of tooth cracks on the vibration behavior of spur gears. Gears are a key component that is widely used in various rotating equipment in order to transmit power and change speed. Any failure of this vital component may cause severe disturbance to production and incur heavy financial losses. The tooth fatigue crack is amongst the most common causes of gear failure. Early detection of tooth cracks is crucial for effective condition-based monitoring and decision making. The scope of this work was widened to include the influence of multiple simultaneous tooth cracks on the time and frequency domain responses at various locations and with different severity levels.

As cracks significantly alter the gear mesh stiffness, a finite element analysis was performed to determine the stiffness variation with respect to the angular position for different combinations of crack lengths. A simplified six degrees of freedom nonlinear lumped parameter model of a one-stage gearbox was developed to simulate the vibration response of faulty spur gears with the consideration of inter-tooth friction. Four different multiple crack scenarios were proposed and studied. The performances of various statistical fault detection indicators were investigated.

The vibration simulation results of the gearbox obtained using MATLAB were verified with those stated in the published research articles. It was observed that as the severity of a single crack increased, the values of the time-domain statistical indicators increased, with different rates. However, the number of cracks had an adverse effect on the values of all the performance indicators, except the RMS indicator. The number and amplitude of the sidebands in the frequency spectrum were also utilized to detect the severity of the faults in each scenario. It was observed that, in the case of consecutive tooth cracks, the number of spectrum peaks and the number of cracks were well consistent in the frequency range of 4 to 5 kHz. The main finding of this study was that the peak spectral amplitude is the most sensitive indicator to the number and severity of cracks.

ACKNOWLEDGEMENTS

First and foremost, all praises and thanks to Allah (God) Almighty for providing me the persistence, the patience, and the blessing to complete this thesis.

I would like to express my profound and sincere gratitude and appreciation to my supervisor, Associate Professor Dr. Sadok Sassi, for his real encouragement, wise guidance, critical comments, and correction of the thesis. Dr. Sadok entrusted me with this interesting project and provided me with all the resources necessary for accomplishing my research objectives.

Sincere thanks to all my teaching staff, colleagues and batch mates at Qatar University for their support and feedback. Last but not least, I would like to dedicate this work to my parents. Their unconditional love has encouraged me throughout the whole process of pursuing my education, and their support has enabled me to bring this work to completion.

TABLE OF CONTENTS

LIST OF TABLES

LIST OF FIGURES

Chapter 1. INTRODUCTION

This chapter gives the background information and justifications about the selected thesis topic. Different types of gears and gear tooth profiles are mentioned, as well as the main gear failure causes, and the common monitoring techniques used to detect the gear tooth cracks. Finally, the aim of the project and its objectives are stated, and the chapter ends by describing the thesis content.

1.1 Background

Gears are toothed mechanical components that are used to transmit power or motion by meshing without slippage. In a gearset regardless of which one is driving the other, the pinion is the smaller gear while the gear or wheel is the larger gear. Gears are used to change the speed or direction of rotation, or even to move the rotational motion to a different orientation. Gears can also change torque through the mechanical advantage of gear (gear ratio). They can be used with different orientation of shafts, such as parallel, nonparallel, perpendicular and intersecting, and perpendicular and nonintersecting. Also, they can be assembled with different types and sizes inside a casing as shown in Figure 1. Regarding their ability to transfer power, gears are better than both chains and belts. Concerning efficiency, a gear drive has higher efficiency than both a chain drive and a belt drive, and that is because belts and chains tend to slip while gears are positive drives. The advantage of gears is that the teeth prevent slipping that allows transmitting higher torques. Gears can mesh as well with non-rotating parts that have teeth. They are called racks and are used to produce linear motion instead of rotational one.

Figure 1: Gearbox [1]

1.1.1 Common Gear Types

The gears are classified into several types with different characteristics and applications. Gears are commonly classified by the orientation of axes, as parallel, nonparallel, intersecting, and nonintersecting axes gears. Some gear types with their categories are presented in Table 1.

Table 1: Gear types and categories [2]

Gear Type	Gears Axes Category
Spur and helical gears	Parallel
Bevel gears	Intersecting
Crossed helical and worm gears	Nonintersecting

The next section gives some details about the types of gears commonly used in industries together with their fundamental properties.

1.1.1.1 Spur Gears

The spur gear is the most common type of gears in the industry. The teeth of the spur gears are parallel to the axis of rotation. They are used to transfer rotational motion between parallel shafts and can have internal (Figure 2-a) or external (Figure 2-b) teeth. They are cheap, easy to manufacture and do not produce an axial thrust force. They have high efficiency up to 98%, but they are noisy due to intermittent meshing [3].

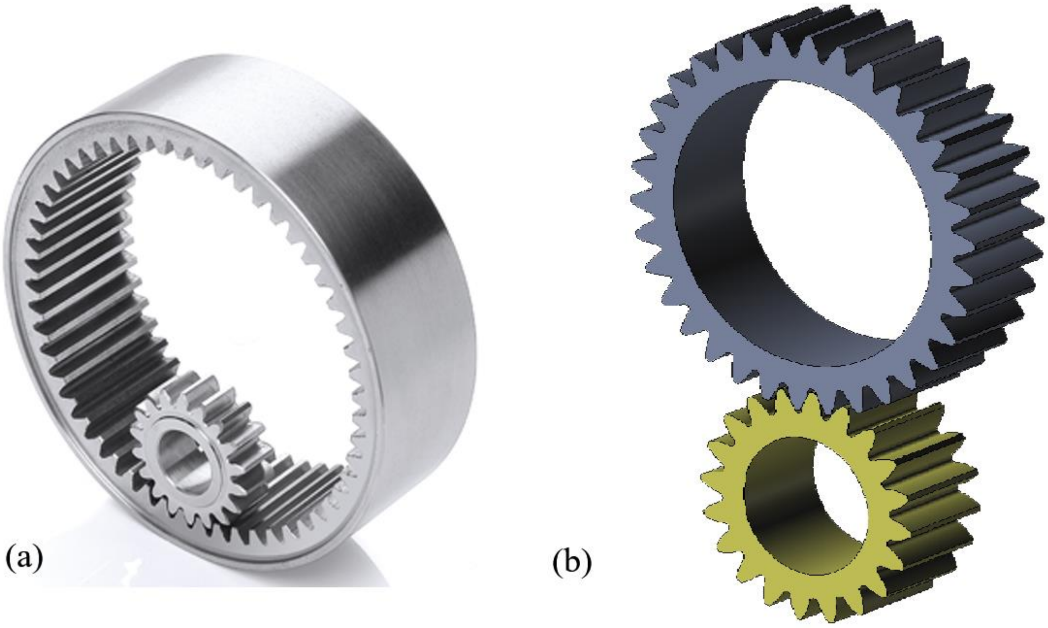

Figure 2 : Spur gear: (a) Internal [4]; (b) External [5]

1.1.1.2 Helical Gears

The evolved form of spur gears are the helical gears. Unlike the spur gears, the helical gears have teeth that are inclined to the rotation axis. They can be meshed in a parallel (Figure 3) or crossed orientations as shown in Figure 4. Helical gears were made to replace spur gears that could not stand high stresses and high rotation speed. These types of gears operate with less noise and vibration than spur gears. However, they produce an axial thrust force. The efficiency of helical gears is around 97% for parallel mesh and varies between 50% and 90% for crossed mesh [6].

Figure 3: Parallel mesh of helical gears [7]

Figure 4: Crossed mesh of helical gears [8]

1.1.1.3 Double Helical Gears

Double helical gears were developed to overcome the produced thrust force in case of using the helical gears. Double helical gears consist of two sections of teeth, one on each side, see Figure 5. During the operation of helical gears, the thrust loading generated from the right side is canceled by that generated from the left side, since the angles of the teeth are opposite to each other. Usually, there is a space between the teeth placed on the two sides of the gear. These types of gears have efficiency up to 95%, but they are very expensive [6].

Figure 5: Double helical gear [9]

1.1.1.4 Worm Gears

Worm gears teeth resemble a screw thread which mates with a worm gear, where the rotation direction of the worm determines the rotation direction of the worm wheel (Figure 6). The classification of the worm depends on the way the teeth are cut, right-hand or left-hand [6]. When large speed ratios are required, the worm gears are usually used, as the gear reductions can be greater than 100:1. Another advantage of the worm gear is that the wheel can be rotated by the worm in one direction, but depending on the helix angle value the irreversibility of the mechanism could be possible. The efficiency of this gear type is between 40% and 85% [10].

Figure 6: Worm gear meshes with a worm gear [11]

1.1.1.5 Bevel Gears

Bevel gears are cone-shaped gears usually used when the axes of the driver and driven shafts intersect forming a 90-degree angle, but they can work at other angles as well. Bevel gears can have straight (Figure 7-a), spiral (Figure 7-b) or hypoid teeth. The spiral bevel gear, which has curved teeth, has solved the problem of intermittent meshing that occurs in the straight bevel gear, as during the engagement the contact point starts at one end of the tooth and gradually moves across the whole tooth like the helical gear. Both the straight and the spiral bevel gears can be used on perpendicular shafts in the same plane only. On the other hand, the hypoid gear can be utilized with shafts in different planes as shown in Figure 8 [12].

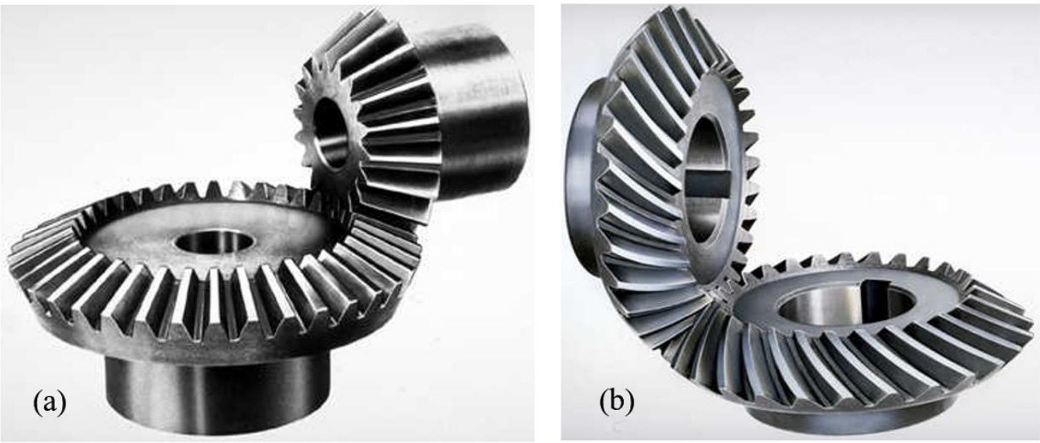

Figure 7: Bevel gear [11]: (a) Straight bevel gear; (b) Spiral bevel gear

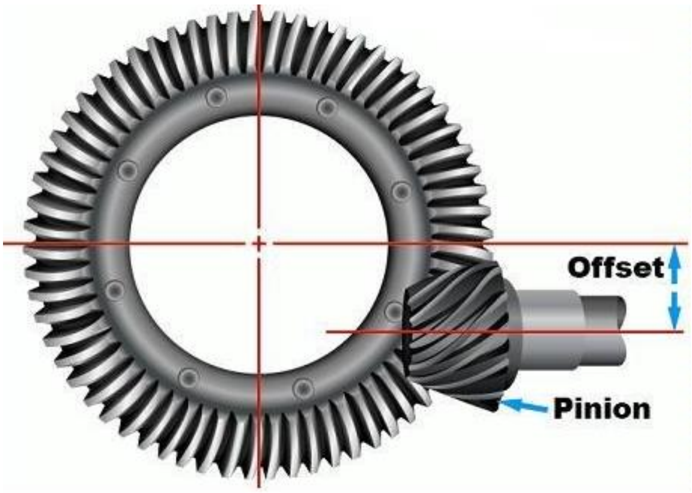

Figure 8: A hypoid reduction gear [13]

1.1.1.6 Racks (straight gears)

Another type of gears is racks. They are straight gears of infinite diameter meshed with a pinion gear making them the only gear type that can convert rotational motion to translational motion, see Figure 9. They transmit power efficiently and offers better precision than other conversion methods. Also, they can be joined with each other to make any desired length. The radius of the pinion relates the velocity and the force of the rack with the angular velocity and the torque of the pinion [2].

Figure 9: Spur tooth rack and pinion [14]

1.1.2 Law of Gearing

For producing a constant velocity ratio, the curved profiles of the mating teeth must be such that the law of gearing is satisfied. This law states that: “In order to have a constant angular velocity ratio, the tooth curves must be so shaped that the common normal to the tooth profiles at the point of contact will always pass through the pitch point, irrespective of the position of the point of contact during the course of action.” [6]. For gears used in tools that require accuracy during operation, stability in the angular velocities is necessary. However, before meshing gears together, some conditions must be taken into consideration to achieve smooth running of the machine and prevent the occurrence of any problem. The essential conditions for a correct meshing are that the gears must have:

1) The same pressure angle
2) The same size of teeth (same module or circular pitch)

The pressure angle of a standard gear is the angle between the line tangent to the pitch circle, and the line normal to the tooth profile at the pitch circle. There is a relation between the pressure angle, the noise generated, and the strength of the gear tooth. Higher pressure angles provide higher strengths since the base of the tooth is wider, and the teeth are not susceptible to undercutting at low numbers of teeth. However, that makes the teeth produce more noise due to the high friction forces. Some standard pressure angles include 14.5^o, 20^0, and 25^o. A pressure angle of 20^o is the most widely used as it is a good compromise between smoothness, power transmission, and strength.

The size of gear teeth can be measured by the circular pitch, P_c, which is the distance between adjacent teeth around the pitch circle, where the circular pitch is expressed as:

$$P_c = \frac{\pi\ x\ pitch\ diameter}{Number\ of\ teeth} \qquad \text{Eq. 1}$$

Since it is a must to have the circular pitch of the pinion to be equal to that in the gear for meshing to be possible, thus:

$$\text{For pinion: } P_c = \frac{\pi\ x\ d_1}{z_1} \qquad \text{Eq. 2}$$

$$\text{For gear: } P_c = \frac{\pi\ x\ d_2}{z_2} \qquad \text{Eq. 3}$$

where Z_1 and Z_2 are the numbers of pinion and gear teeth, respectively. While d_1 and d_2 are the pitch diameters of the pinion and the gear, respectively.

From Eq. 2 and Eq. 3:

$$\frac{d_1}{z_1} = \frac{d_2}{z_2} = \frac{P_c}{\pi} = \text{Constant} = \text{Module } (m) \qquad \text{Eq. 4}$$

Therefore,

$$\frac{d_1}{d_2} = \frac{z_1}{z_2} \qquad \text{Eq. 5}$$

Figure 10 depicts two curved bodies in contact with each other. Body 1, with center at *O_1* and having angular velocity ω_1, is driving, while Body 2, with center *O_2* and due to the action of Body 1, Body 2 is having angular velocity ω_2, is driven. At this instant, the point of contact is at *M*, where the two surfaces are tangent to each other, and the common tangent to the curve is *T*-*T*, while the forces are transmitted along the common normal P_1P_2, also known as the line of action. The line of centers O_1O_2 intersects the line of action at the pitch point *A*. Although the two gears have different angular velocities ω_1 and ω_2 at point *M*, their linear velocities along P_1P_2 have the same direction and magnitude. Otherwise, the two surfaces would separate from each other.

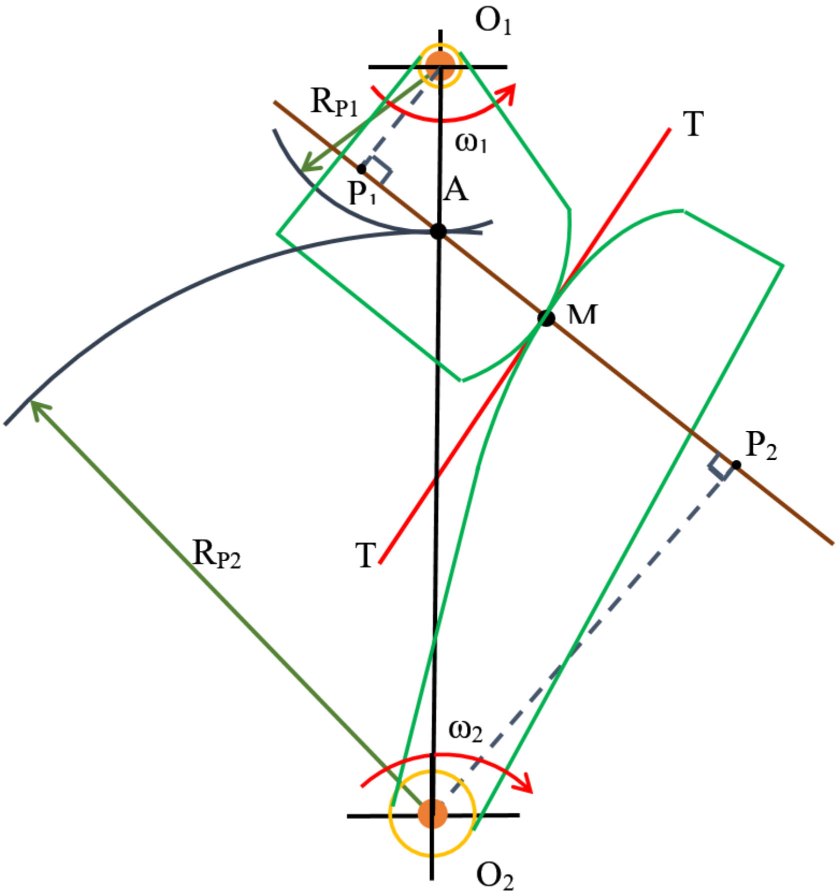

Figure 10: Transmission of motion and conjugate action

Therefore,

$$O_1P_1 . \omega_1 = O_2P_2 . \omega_2 \qquad \text{Eq. 6}$$

Or

$$\frac{\omega_1}{\omega_2} = \frac{O_2P_2}{O_1P_1} \qquad \text{Eq. 7}$$

The ratio between the angular velocities of the driving gear to the driven gear is known as the angular velocity ratio or the gear ratio, which is constant and given by:

$$GR = \frac{\omega_1}{\omega_2} = \text{constant} \qquad \text{Eq. 8}$$

The position of *M* should remain fixed, for a constant angular velocity ratio. Thus, the transmission motion between the two gears will be equivalent to that between two imaginary slipless cylinders with radii Rp_1 and Rp_2.

$$V_1 = \omega_1 . R_{p1} \qquad \text{Eq. 9}$$

$$V_2 = \omega_2 . R_{p2} \qquad \text{Eq. 10}$$

$$R_{p1} = \frac{mZ_1}{2} \qquad \text{Eq. 11}$$

$$R_{p2} = \frac{mZ_2}{2} \qquad \text{Eq. 12}$$

So the gear ratio can also be expressed as:

$$GR = \frac{\omega_1}{\omega_2} = \frac{R_{p2}}{R_{p1}} = \frac{Z_2}{Z_1} = \text{constant} \qquad \text{Eq. 13}$$

1.1.3 Gear Tooth Profiles Satisfying the Law of Gearing

A constant velocity ratio is maintained in a pair of meshing gears, as the tooth curves are designed in a way that at the contact point the common normal will always pass through the pitch point. The curves satisfying such a condition are termed as conjugate curves. It has been established that the two families of curves, the involutes, and the cycloids, satisfy the law of gearing, and these curves are adopted for all practical purposes.

“The involute curve of a circle is a path traced by the end of a string initially wrapped on a circle when the string is unwrapped from the circumference of the circle called the base circle” (Figure 11-a) [15]. The geometric relation between the base circle and the involute curve is shown in Figure 11-b.

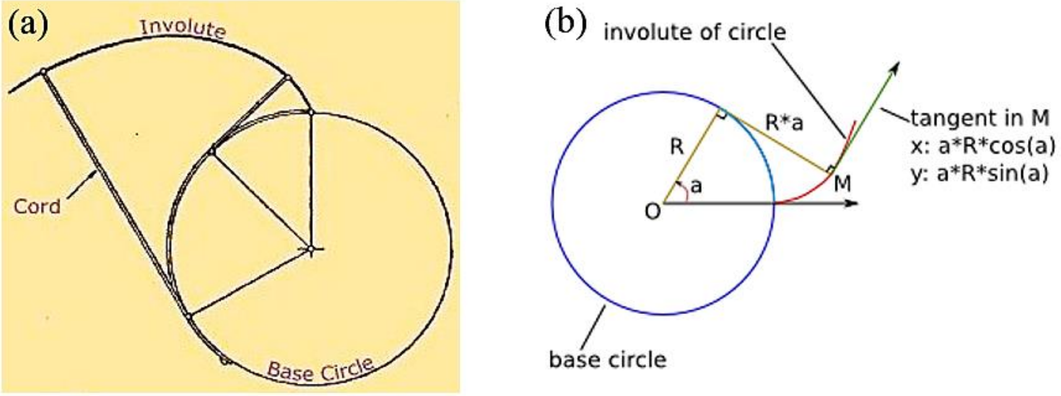

Figure 11: (a) Involute creation [15]; (b) Involute geometry [16]

The other type is the Cycloid curve, which consists of an epicycloid and a hypocycloid curve. The epicycloid is generated when a circle rolls outside another circle, while if it rolls inside another circle, then the generated curve will be hypocycloid. Cycloidal gears are those whose teeth profile is made up of cycloidal curves as shown in Figure 12.

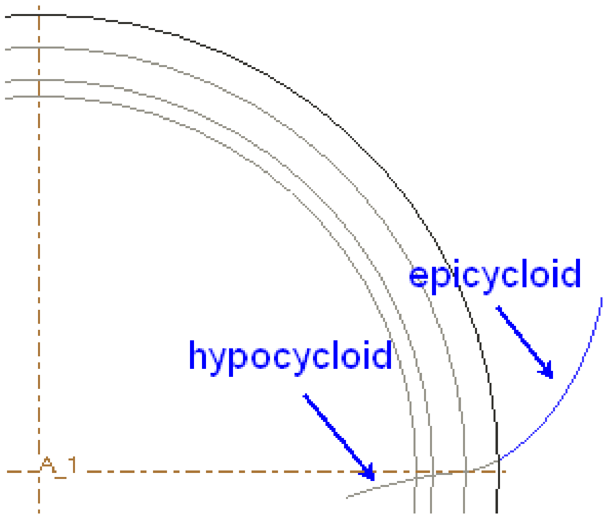

Figure 12: Cycloid curve generation [17]

The advantages of the involute curve, however, are so numerous that the involute gear is the most commonly used tooth form for power transmission today [2]. Involute gears can be seen in car gearbox, ships, robotics application, home appliances, machine tools, while cycloidal gears are found mainly in mechanical clocks and watches.

1.1.3.1 Advantages of The Involute Gears

1) The velocity ratio almost does not change as long as the center distance stays within certain limits, on the contrary, the cycloidal gears require maintaining the exact center distance.
2) The pressure angle remains constant throughout the teeth engagement, providing smooth running and less wear of gears. On the other hand, in the cycloidal gears, the pressure angle reaches its maximum at the beginning and the end of the engagement, while it reaches zero at the pitch point, leading to rough running and more wear of gears.

3) The contact surface is always perpendicular to the plane of contact; this helps reducing torque variation, and thus involute gear gives silent operation.
4) The involute gears are easier to manufacture than the cycloidal gears, as only one curve is needed to generate the face and the flank of the involute teeth, unlike the cycloidal gears where two curves, which are the hypocycloid and the epicycloid, are required.

1.1.3.2 Disadvantage of The Involute Gears

The main disadvantage of the involute teeth is that for gears having a small number of teeth, interference might occur. However, this may be prevented by changing the addendum and the dedendum values of the mating teeth or by altering the pressure angle.

1.1.4 Gear Failure Causes

Many reasons can lead to gear failure, some are pre-operation causes such as manufacturing and installation errors, and some are during operation, such as excessively applied load and insufficient lubrication. A gear failure is an unwanted event as it involves a termination of the ability of the gear to perform the required function and can entail serious and costly consequences. By implementing an appropriate maintenance strategy, the number of failures and unplanned stoppages can be reduced, and the following consequences can be kept to a minimum.

Due to cyclic loading, fatigue is induced on the teeth of the gear and cracks are initiated making the tooth fatigue one of the most common causes of gear failure. Tooth breakage is the most severe failure for a gearbox, one which may lead to the complete failure of the gear. Since the unexpected failure of a gearbox may cause significant economic loss and even threaten human life, the safety of gearboxes becomes an important factor in mechanical safety [18].

The thickness, width, and length are the parameters used to describe a gear tooth crack (Figure 13), and more importantly, the crack propagation angle (α), as shown in Figure 14.

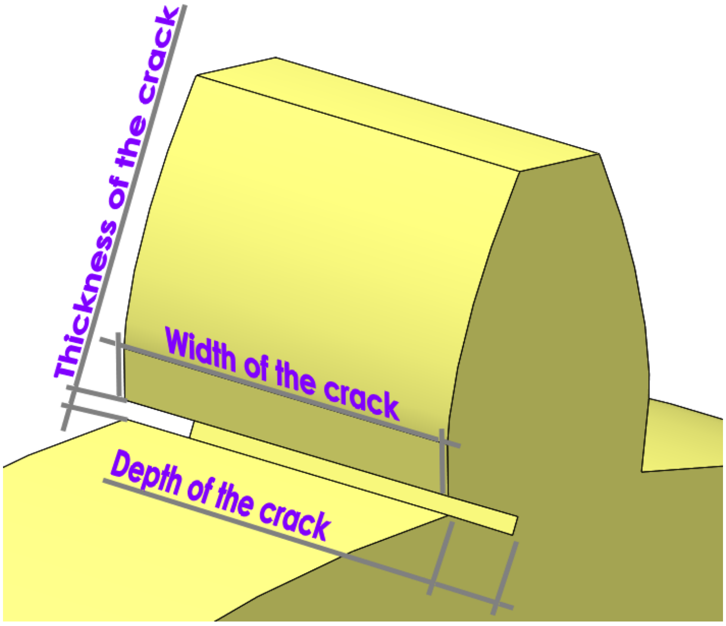

Figure 13: A 3D schematic for a crack

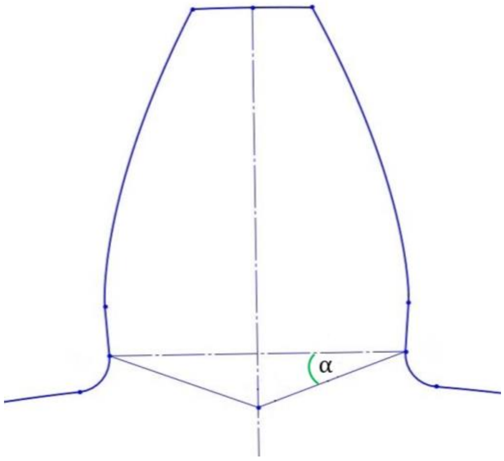

Figure 14: The crack propagation angle

Typically, a gear tooth crack in the root results from the small rim thickness in the gear, improper machining or treated material, or imperfections in the material that can lead to crack initiation. Also, severe operating conditions such as misalignment or overload or operation near the resonant frequency of the gear leads to increasing the degradation rate [19].

The crack propagation depends on the backup ratio, the ratio between the rim thickness and the tooth height [21,22] as shown in Figure 15. It was found that cracks would propagate through the teeth when high backup ratios are used (Figure 16-a), but for low backup ratios, they would propagate through the rim (Figure 16-b). The initial crack angle also accounts for the crack propagation, however, for low backup ratios, the propagation is through the rim even with low crack propagation angles. The crack propagation path, for high backup ratios, tends to be smooth with a slight curvature [21]. A backup ratio equals to three or more was found to allow crack propagation through the teeth regardless of the initial crack angle as shown in Figure 17.

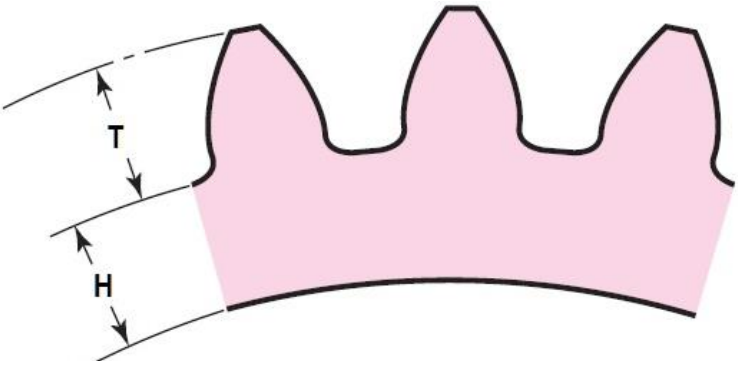

Figure 15: Schematic for the backup ratio *(H/T)*

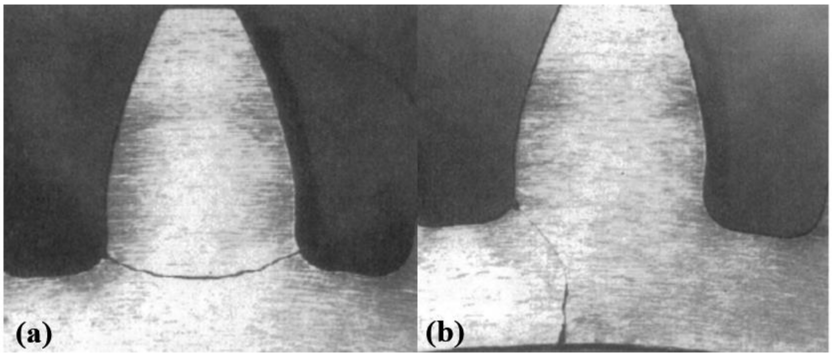

Figure 16: Crack propagation path [22]: (a) through the teeth (b) through the rim

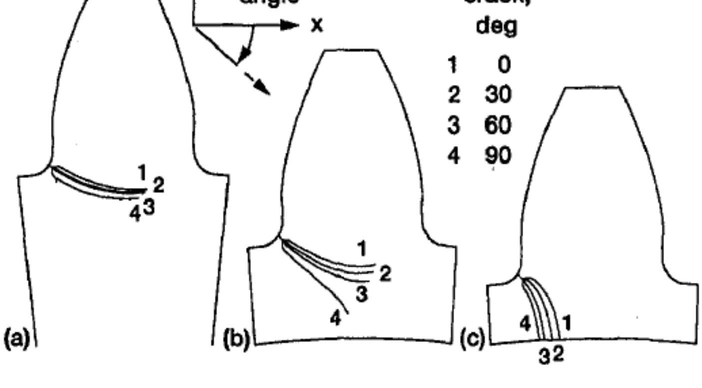

Figure 17: Crack propagation paths for different initial crack angles [22]: (a) backup ratio = 3.3, (b) backup ratio = 0.5, and (c) backup ratio = 0.3

1.1.5 Gearbox Health Monitoring

An appropriate maintenance strategy should be performed to minimize the production loss due to gears failures. Maintenance aims to increase the availability of a system, maximize the performance efficiently and regularly, and increase the reliability of the system.

1.1.5.1 Maintenance Strategies

There are three main maintenance strategies; the simplest strategy is the “corrective/breakdown maintenance”, where the maintenance is only performed when the equipment, which was left to operate, fails. This strategy is only justified when the repair costs are less than performing other maintenance strategies, and the downtimes are not critical.

The other maintenance strategy is the “preventive/scheduled maintenance”, where components are replaced based on previous data collected about their failure tendency, this is done according to a planned schedule. Therefore, the worn components are replaced before the failure happens, leading to the prevention of breakdowns and failures. This maintenance strategy is used when the production loss for total failure is huge and downtimes are critical. However, it has one main disadvantage as replacing parts based on statistical and historical data does not guarantee that failure will not occur just before they are replaced, and that will lead to sudden shutdowns. On the other hand, some parts might be replaced before they are worn out, as their actual state is not known, and that will lead to increase in cost.

Despite the drawbacks of the previous strategies, the condition based maintenance (CBM), also known as predictive maintenance, has many benefits as machinery conditions are periodically monitored and this enables appropriate actions to be taken, such as machine adjustment, repair, or overhaul. The main advantages of CBM are a reduction of cost and repair time, replacement of the deficient pieces only, and optimized scheduling of the work periods.

The condition monitoring techniques that can be used are vibration analysis, acoustic emission, lubricant analysis, infrared thermography, and electrical current measurement.

1.1.5.2 Vibration-Based Fault Detection

The vibration analysis is the most commonly used technique for CBM of rotating equipment. It provides early warnings for many serious faults such as damaged bearings or gears, lubrication problems, misalignment, unbalance, and loose fittings. Of all the various condition monitoring techniques, vibration analysis provides the greatest percentage of payback as it is relatively inexpensive. Accurate and reliable information for a variety of equipment can be obtained from the vibration analysis making it is one of the most dominant methods and the primary method for the rotating equipment [23].

Fault detection using vibration analysis technique, also known as Vibration-based fault detection, is widely applied in many industries to monitor and evaluate machine health using vibration signals. The concept of this technique is that machines are monitored to detect degradation before the occurrence of failure allowing for a properly scheduled shutdown of the whole machine to prevent catastrophic failure [24]. Vibration analysis has become highly important in fault detection in gearing systems, as any change in the vibration signal due to gear degradation can be detected, giving an early warning. For instance, when a gear has a cracked tooth, the stiffness of the tooth decreases giving a high vibration signal amplitude. In this example, the fault will be a crack in a tooth which might lead to a total system failure or at least decrease its design capacity.

1.2 Research Objectives

The aim of this study is to develop a realistic model with a view to early detecting and identifying faults in external spur gears. This model will focus on the faults developed by multiple gear tooth cracks of different sizes. Moreover, this model can also be used for tracking the evolution of crack severity. A further objective of this study is to characterize the time-domain and spectral signal features for the fault diagnosis using different statistical indicators.

1.3 Research Methodology

The methodology employed in this study is based on a 6 DOF dynamic numerical model that was developed to allow the investigation of the effect of one-stage spur gearbox tooth cracks on the vibration response. The contact analysis between the gears was carried out using a tailor made MATLAB code. The total gear mesh stiffness was estimated with respect to the pinion rotational angle using both SolidWorks and MATLAB software. Tooth root cracks were assumed to be present on the pinion only. The total mesh stiffness was then utilized to simulate the vibration response of the pinion. The inter-tooth friction is considered in this model. The assumptions utilized for the development of the dynamic model are similar to the assumption used in [25]. In order to simplify the development of the model, the influence of lubrication was ignored. All the system components were assumed to be rigid, except the gears. The stiffness of the meshing gears was considered and the error in the mesh stiffness due to this assumption can be ignored since this study investigates the difference between the healthy and faulty condition. For the vibration analysis, different statistical indicators were applied to the original and residual vibration signals in the time and frequency domains. The diagnostic performance yielded by these statistical techniques (between the original signals and residual signals) was compared and characterized based on their sensitivity. The overall organigram of the code developed is presented in Figure 18.

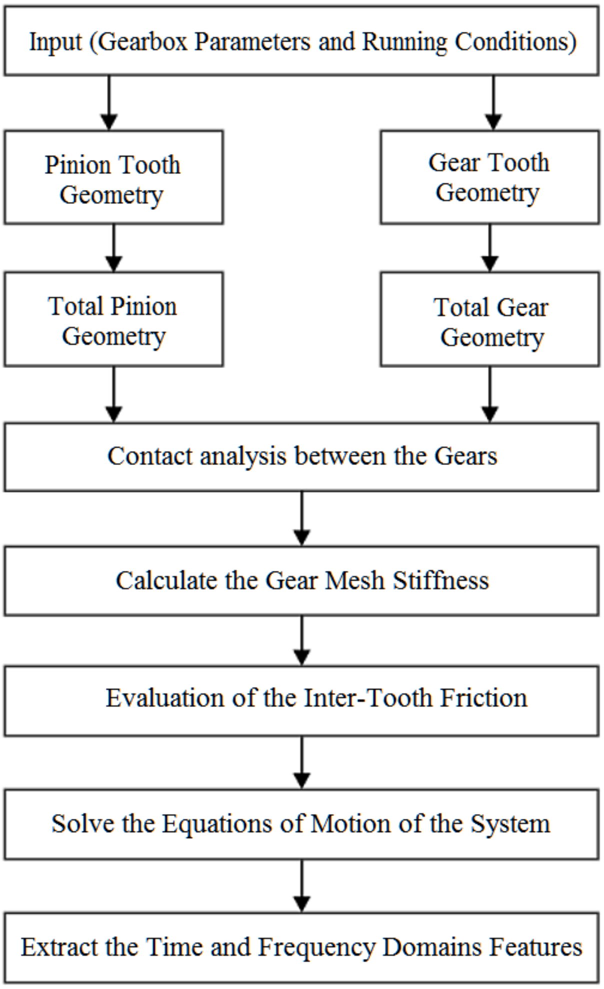

Figure 18: The overall organigram for the code developed

1.4 Organization of Thesis

This thesis is organized as follows:

Chapter 1: Introduction

This chapter introduces the research background and presents a literature survey about gear tooth cracks and crack propagation, and explaining the different methods used for vibration-based fault detection analysis. Chapter 1 also includes the research objective, research methodology, as well as outlining the thesis organization.

Chapter 2: Literature Review

This chapter further adds to the literature survey as it presents the possible initial crack position and the crack modeling with different propagation scenarios. Also, an explanation is given of the method utilized for gear mesh stiffness evaluation with the presence of a crack in the gear tooth root. Moreover, it explains briefly about adding the effect of friction in the analysis and different dynamic models that can be used. It ends with the vibration based analytical techniques for gear fault detection.

Chapter 3: Theoretical and Numerical Development

This chapter explains in detail the development of the numerical model using MATLAB software. It starts with how the gear profile is generated, then gears alignment, and the teeth contact analysis. Finally, it explains the inter-tooth friction analysis.

Chapter 4: Gear Mesh Stiffness Modeling Including Cracks

This chapter presents the crack modeling used and the gear mesh stiffness calculation. Furthermore, it explains how the individual stiffness of the tooth is obtained using SolidWorks. This method is used to get the time-varying gear mesh stiffness, which can be introduced in gear dynamic models. The proposed multiple crack scenarios are presented in this chapter as well.

Chapter 5: Dynamic Simulation of System Response of Gearbox

The gear parameters used for these models are presented in this chapter. An explanation is given of the dynamic simulation used for modeling and solving the equations of motion to obtain the dynamic response.

Chapter 6: Vibration Response in Time and Frequency Domains

This chapter presents the time-domain results and the performance of the selected statistical parameters and discusses them. The applied signal processing techniques are explained in this chapter. It ends with the influence of cracks on the frequency domain.

Chapter 7: Conclusions and Future Work

The conclusions are summarized, and the significant findings are highlighted in this chapter, and further research is proposed for future work.

Chapter 2. LITERATURE REVIEW

This chapter will illustrate different aspects about cracks in gears, including the initial crack position, the crack propagation paths, and different crack propagation scenarios. The evaluation of the gear mesh stiffness and friction force will be deliberated. The difference between various dynamic models of gear systems is clarified. The chapter also discusses different vibration-based analytical techniques for gear fault detection.

2.1 Initial Crack Position

One of the important aspects of gears degradation is the crack initial position. As for backup ratio equal 1 or less, the original crack position, at the root of the tooth, determines whether the crack will propagate along the tooth thickness or the rim. It was found that if the crack starts at point *D* or *E*, see Figure 19-a, it will propagate along the gear rim unlike points *A*, *B*, and *C* [26].

Usually, the crack position at the tooth root is described by the tangential angle ψ, “the angle between the symmetry line of the tooth and the tangent to the fillet curve” [27], as shown in Figure 19-b. Finite element models indicate that the most critical crack position is in the middle of the tooth fillet at $\psi \approx 35^o$, see Figure 20.

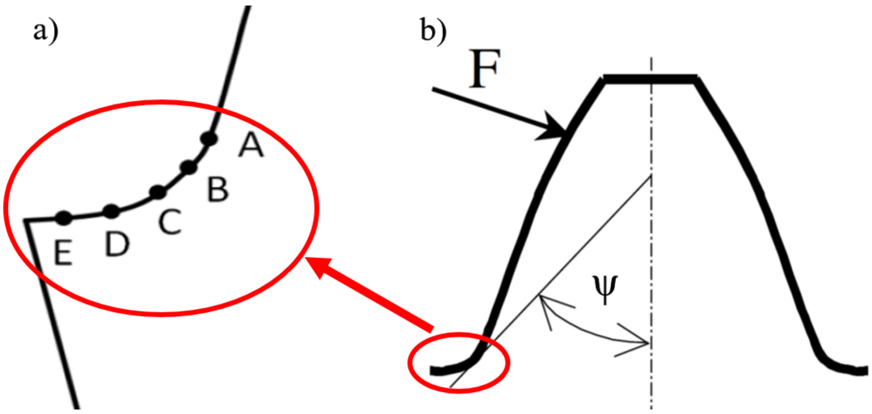

Figure 19: a) Initial crack position points [26], b) Tangential angle

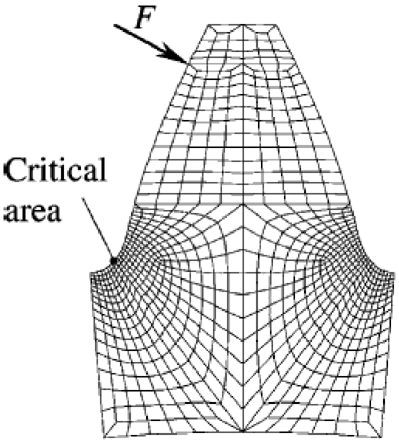

Figure 20: Critical area using finite element model [27]

2.2 Crack Propagation Paths

Many studies have been done to simulate the crack propagation path along both the tooth length and width. Different 2D and 3D gear models have been used and based on the results it was found that for the cracks propagating along the tooth root, the crack propagation takes a slight curve path starting from the tooth root and propagating towards the other root as shown in Figure 21.

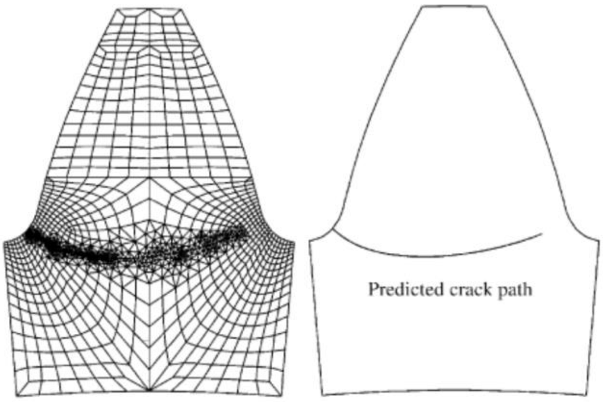

Figure 21: Crack propagation path based on computational results [27]

The crack path can be simplified and approximated by straight lines as shown in Figure 22. Considering different crack sizes, Figure 23(a-d) illustrates the approximated path taken by the crack, where the propagation angle, the angle between the central line of the tooth and the crack path, is 45°. When the crack reaches the central line of the tooth, it changes its direction and propagates towards the other root to be symmetric around the central line, and that gives an approximation for the actual crack propagation. In other studies, the crack propagation angle is taken as different values such as 20° and 57° [28].

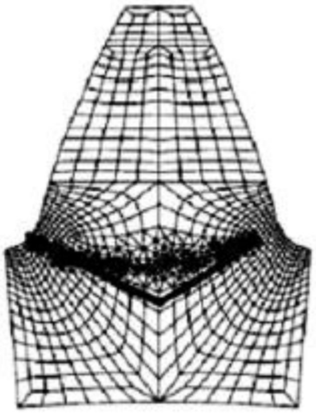

Figure 22: Crack propagation approximated path [29]

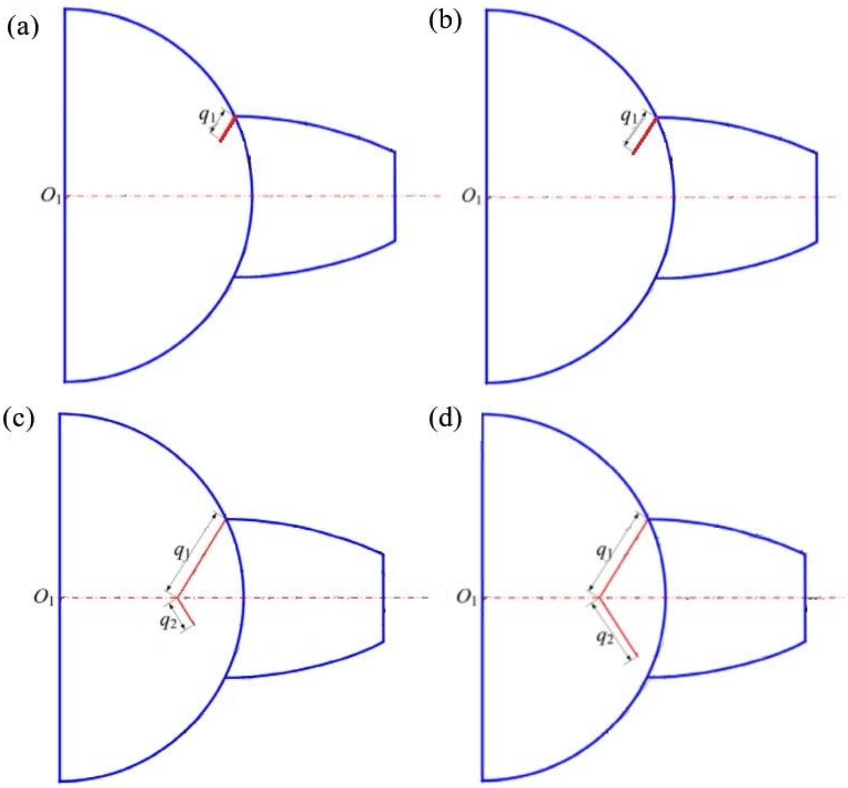

Figure 23: Different crack levels: (a) case 1, (b) case 2, (c) case 3, (d) case 4 in [29]

2.3 Crack Propagation Scenarios

Many researchers have proposed different crack propagation scenarios which can be used to model the crack propagation [30]; the most common ones are:

1) The crack is extended along the entire tooth width with the same length distribution, this scenario is adapted when a uniform distributed load is assumed (Figure 24-a), and it has been considered by [28, 31, 29]. The stiffness of a cracked tooth with such crack propagation scenario is lower than that of the other two following scenarios.

2) The crack is extended along the entire tooth width with a parabolic crack length distribution, presented in [32]. This scenario is adapted when a non-uniform distributed load is assumed (Figure 24-b). However, with such propagation scenario, the stiffness of the cracked tooth is the highest, as the cracked tooth has a limited movement.
3) The crack propagates in both the length and the width directions at the same time (Figure 24-c), illustrated in [33], which is more realistic for non-uniform load distribution cases than the previous one [30].

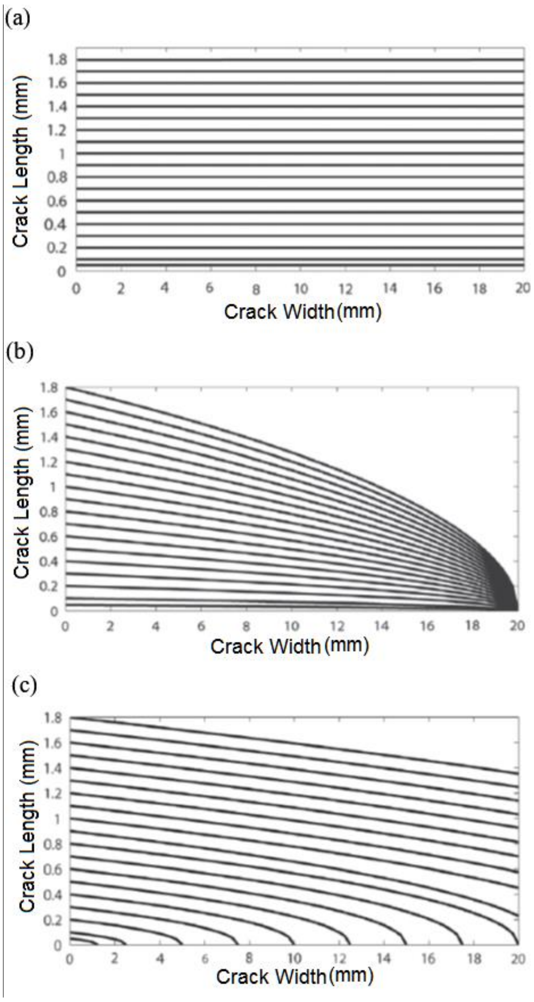

Figure 24: Three different crack propagation scenarios [30]

2.4 Gear Mesh Stiffness Evaluation

Gear mesh stiffness is a time-varying factor that depends on many parameters [28,34]. In fact, the presence of a tooth crack not only adversely affects the individual tooth stiffness but also the total mesh stiffness. The engagement of a cracked tooth decreases the total mesh stiffness, as in the case of double contact it contributes to the total effective mesh stiffness with the tooth preceding and that following it, as depicted in Figure 25.

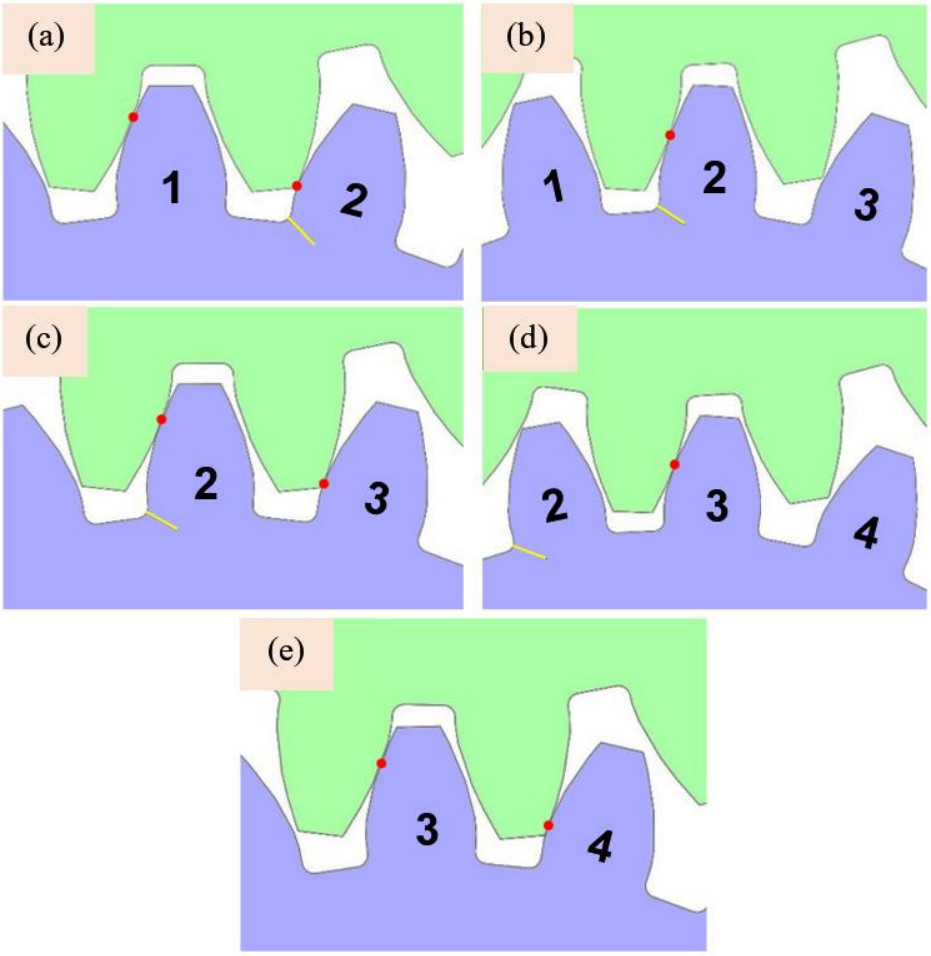

Figure 25: Sequence of engagement of a cracked tooth, (a) Double contact (Start of engagement of a cracked tooth), (b) Single contact (cracked tooth), (c) Double contact (End of engagement of a cracked tooth), (d) Single contact (healthy tooth), and (e) Double contact (healthy teeth)

The time-varying mesh stiffness (TVMS) or the gear mesh stiffness can be calculated using different approaches. The most common methods are the analytical and the Finite Element method (FEM). The analytical approach has a higher computational efficiency, while the FEM is known for giving a good calculation accuracy. Furthermore, the experimental method is also used as it is closer to the actual operation under certain measurement conditions [35]. The TVMS is affected by many parameters such as the angular position of the gear, the contact ratio, and the load applied on the teeth. Also, for a cracked tooth, the crack angle alters the mesh stiffness significantly with the same crack position and length, as shown in Figure 26. The crack initial position has an effect as well, where with a tangential angle 35° the mesh stiffness is lower than that of angle 65°, see Figure 27.

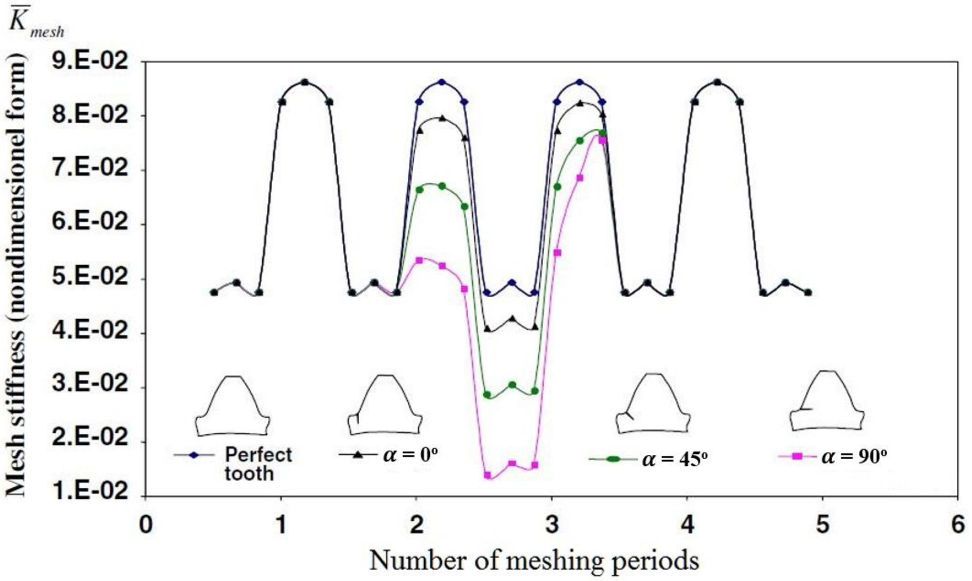

Figure 26: Mesh stiffness at different crack angle [36]

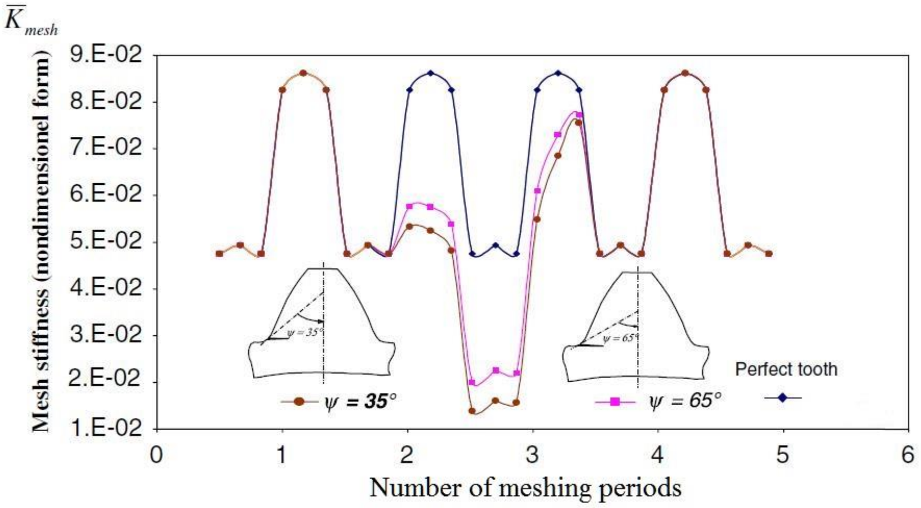

Figure 27: Mesh stiffness at different tangential angle (position) [36]

The stiffness at (a) in Figure 28 is higher than that of (c), and that is because the pinion, which has a cracked tooth is considered as the driver gear. However, if the pinion was considered as the driven, then the time-varying mesh stiffness plot will be reversed (stiffness at (a) would be lower than that at (c)) [33]. Also, the direction of rotation of the gears does not affect the stiffness value.

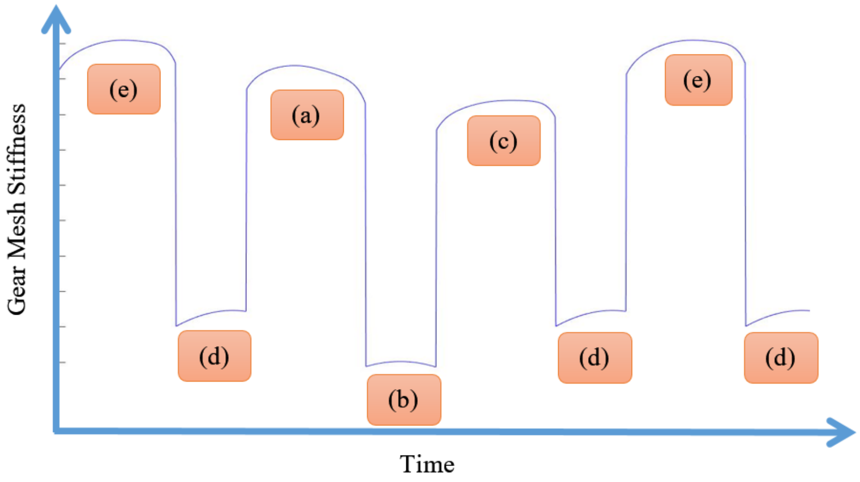

Figure 28: The variation in the gear mesh stiffness at different cases illustrated in Figure 25

Some studies were done to identify the effect of the crack length percentage (CLP) on the total mesh stiffness (Figure 29), whereas the CLP has an adverse effect on the stiffness. However, the shape of the stiffness curve when the CLP reaches 64% and 81%, presented in [29], does not reflect the real meshing stiffness as the stiffness varies a little at the start of engagement of a cracked tooth as shown in Figure 29.

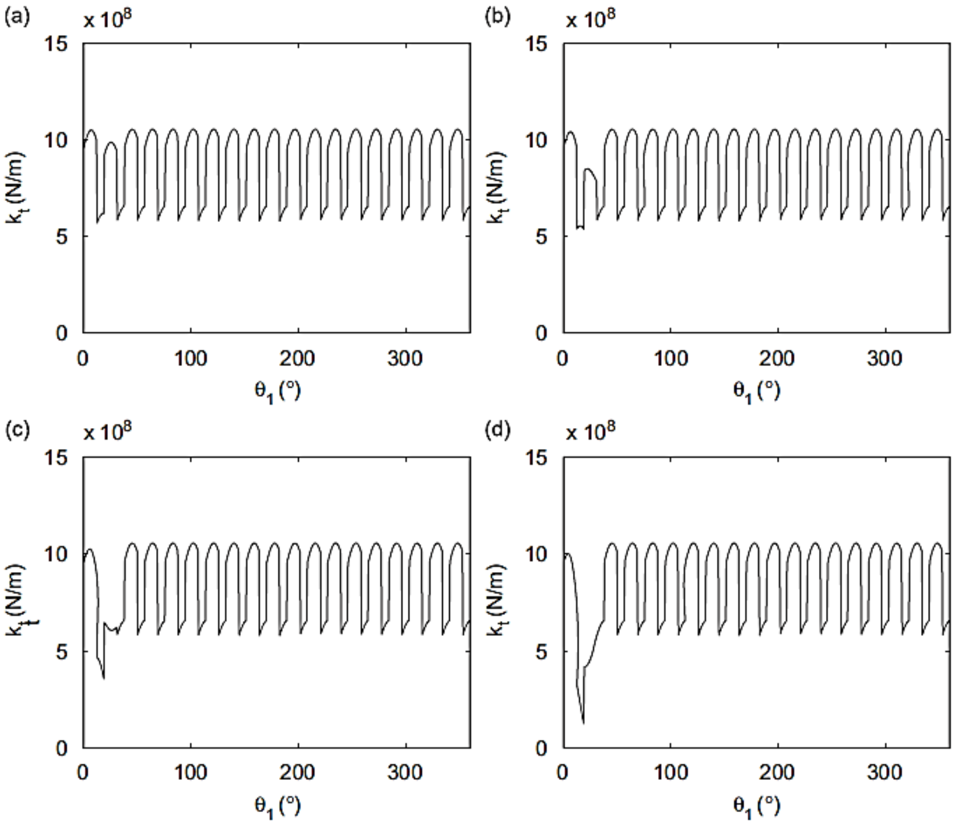

Figure 29: Total mesh stiffness with respect to the rotational angle; (a) 18% crack length (b) 40% crack length (c) 64% crack length (d) 81% crack length [29]

On the other hand, the FEM was used by [28] to obtain the TVMS (Figure 30), the parameters used are shown in Table 2, the results were verified by the analytical approach adopted by [32], see Figure 31, and that developed by [30].

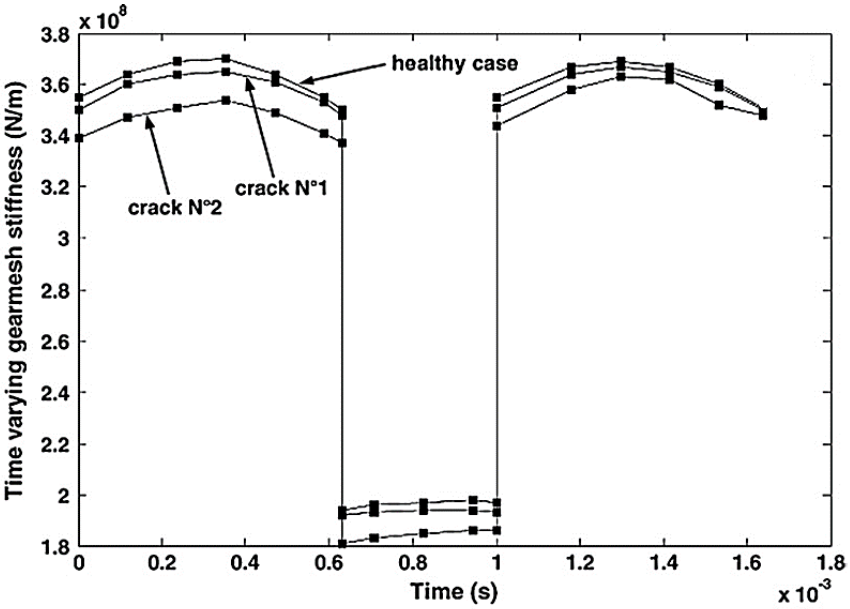

Figure 30: Gear mesh stiffness from [28], using the FEM

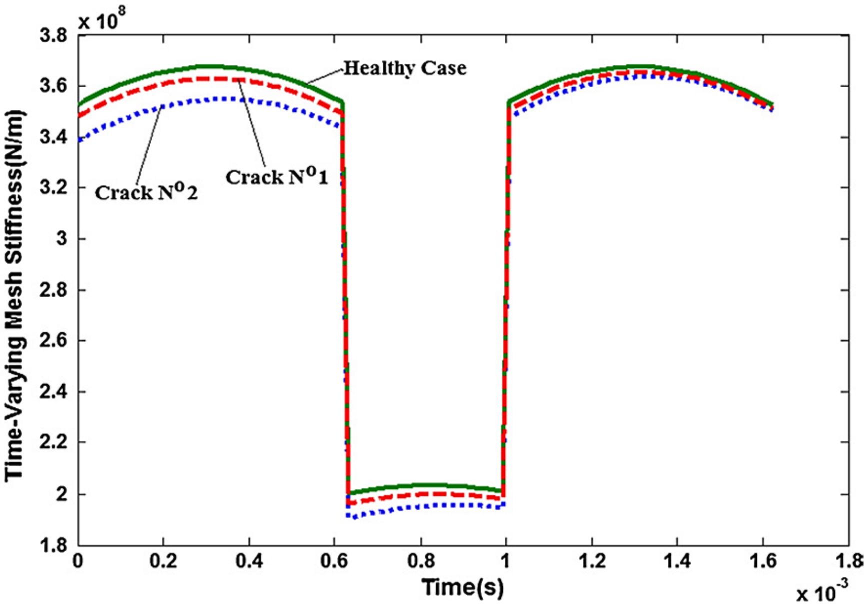

Figure 31: Gear mesh stiffness from [32], using the analytical method

The mesh stiffness also depends on the crack propagation scenario as shown in Figure 32.

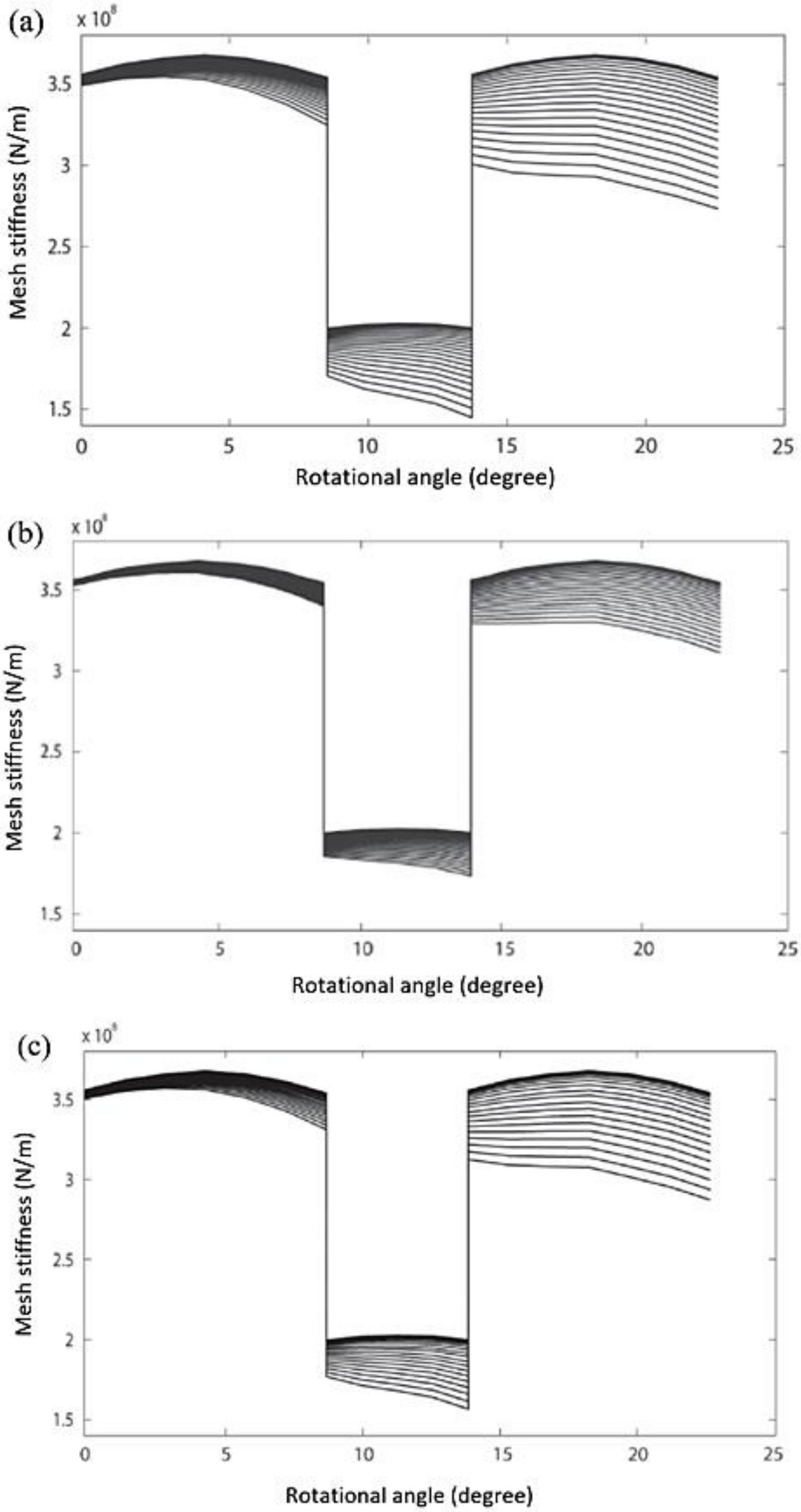

Figure 32: Total gear mesh stiffness for the different crack propagation scenarios shown in Figure 24, respectively [30]

2.4.1 Evaluation of the Mesh Stiffness Using FEM

The gear mesh stiffness can be calculated using the FEM, where the individual stiffness of a tooth is obtained by [37], as shown in Figure 33:

$$K = \frac{F}{\delta} \qquad \text{Eq. 14}$$

where δ is the displacement in the direction of the path of action, and K is Kp and Kg for the pinion and the gear tooth, respectively.

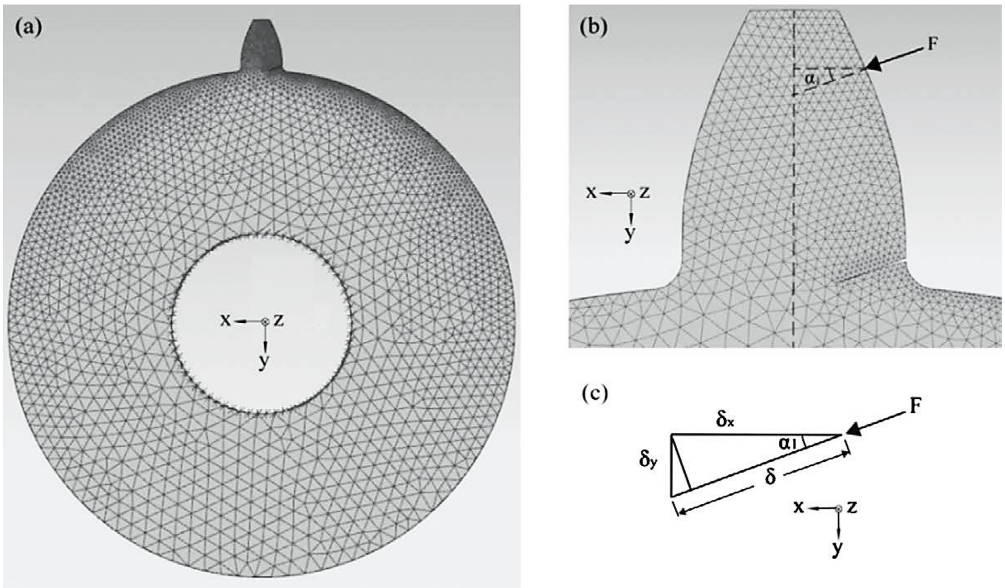

Figure 33: FE modeling: (a) FE gear model with one tooth, (b) crack modeling in the tooth root, and (c) displacement components [37]

The influence of the Hertzian contact K_h can be taken as a constant value during the whole contact period, and it is calculated as [38]:

$$K_h = \frac{\pi E W}{4\,(1-\nu^2)} \qquad \text{Eq. 15}$$

where E is the Elastic modulus, W is the tooth width, and ν is the Poisson’s ratio.

Thus, the total stiffness of one tooth pair in contact K_1 can be calculated as:

$$K_1 = \frac{1}{\frac{1}{k_{p1}}+\frac{1}{k_{g1}}+\frac{1}{k_h}} \qquad \text{Eq. 16}$$

When two pairs are in contact, the stiffness of the second pair will be:

$$K_2 = \frac{1}{\frac{1}{k_{p2}}+\frac{1}{k_{g2}}+\frac{1}{k_h}} \qquad \text{Eq. 17}$$

The equivalent mesh stiffness K_t can be calculated as:

$$K_t = K_1 + K_2 \qquad \text{Eq. 18}$$

Since the individual stiffness varies along the tooth height, where the stiffness is lowest at the tooth tip and highest at the bottom, so its value would vary with respect to the rotational angle. Thus, it is required to calculate the individual stiffness at various angles.

2.5 Friction Force (Direction and Magnitude)

The direction of the friction force between the mating gears is perpendicular to the line of action and opposite to the direction of the slip velocity. The direction of the friction force before the pitch point is opposite to that after passing the pitch point. The friction force applied to the gear is always in the opposite direction to that applied to the pinion [25].

In fact, the magnitude of the friction force depends on the dynamic friction coefficient, μ, and the contact force, F_c, between the teeth along the line of action. The frictional force, F_f, is calculated by:

$$F_f = \mu F_c \qquad \text{Eq. 19}$$

At the pitch point, the magnitude of the friction force is zero. For instance, in case the dynamic friction coefficient is equal to 0.06, it will vary with the shaft rotation between -0.06 and 0.06, with the same number of teeth in the gear and pinion, as shown in Figure 34.

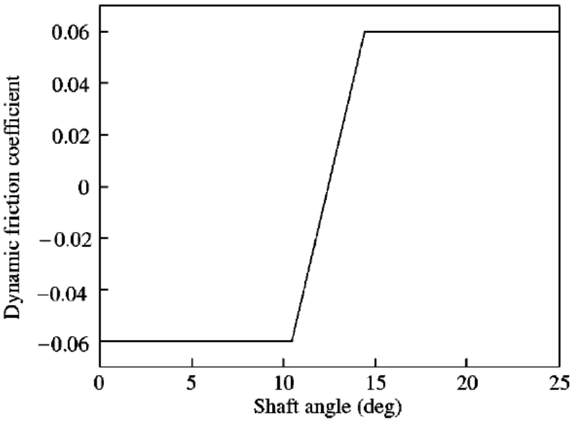

Figure 34: The variation of the dynamic friction coefficient with the rotation angle [25]

As a matter of fact, the contact force also varies with the shaft rotation and also affected by the number of contact points. The load sharing ratio along the path of contact was found using a finite element model of spur gears in mesh [39], (Figure 35).

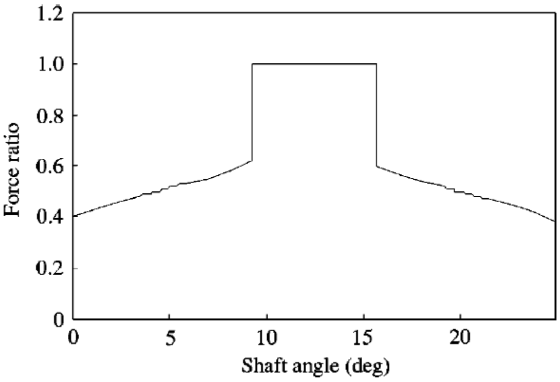

Figure 35: Variation of load sharing ratio along the line of action [25]

2.6 Dynamic Models of Gear Systems

There are mainly two dynamic models for simulating gear systems with cracks, the finite element model, and the lumped mass model [35]. The lumped mass model is usually considered in case the shafts and the bearings supporting the gears are assumed to be rigid, and with small DOFs the precision required is satisfied, while the finite element model is more applicable when flexible shafts are considered.

For the lumped mass model, different multi-degree-of-freedom models have been developed; the commonly used ones are 4 (Figure 36), 6 (Figure 37), 8 (Figure 38), 12 degree-of-freedom (DOF) models (Figure 39). The 4 DOF model includes two torsional and two lateral DOFs for a gear pair, while the 6 DOF model consists of two torsional and four lateral DOFs for a gear pair considering the tooth surface friction and the support stiffness. The 8 DOF model includes four torsional displacements for the motor, driving and driven gears and load, and four lateral DOFs for a gear pair. The 12 DOF consists of three rotational and two translational DOFs for each gear and one torsional DOF for the load and motor.

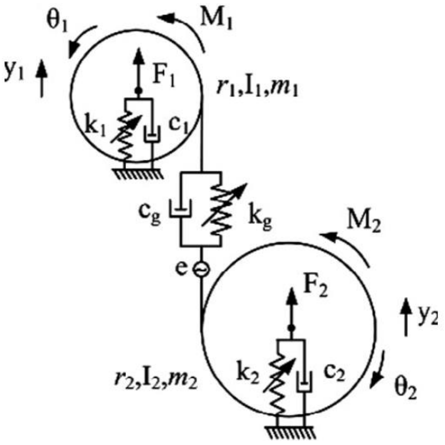

Figure 36: A four DOF model [40]

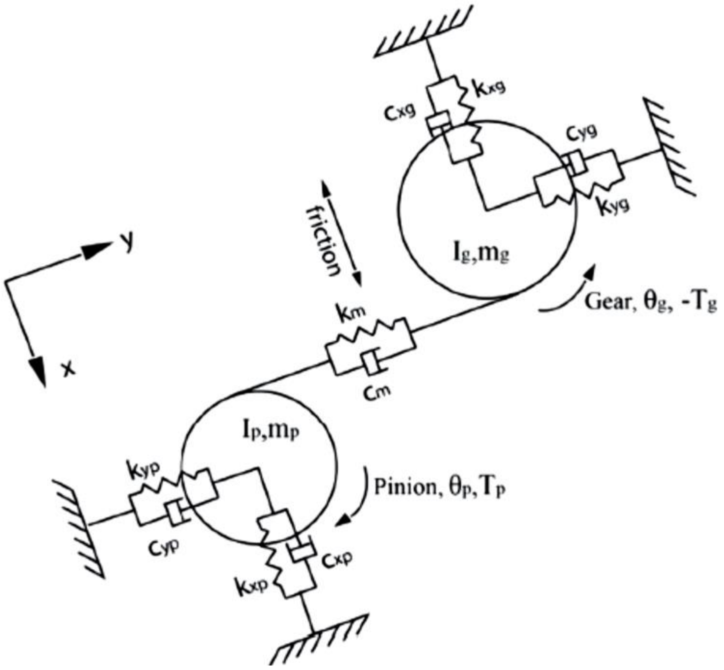

Figure 37: Dynamic model of a gearbox with six DOF [41]

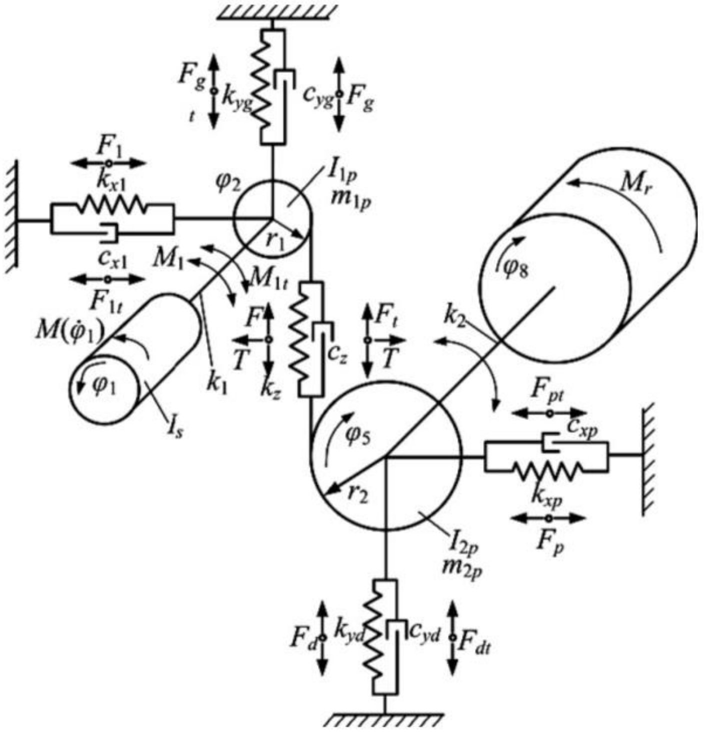

Figure 38: Eight DOF model [42]

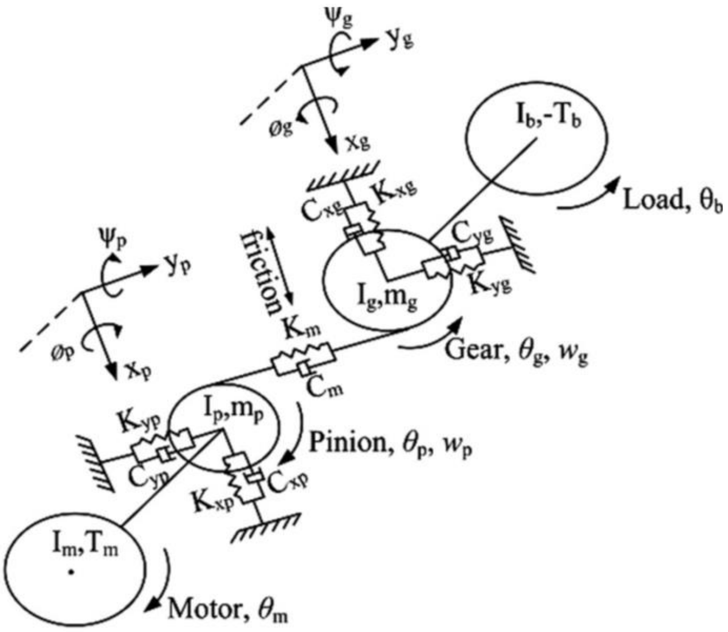

Figure 39: Twelve DOF model [41]

2.7 Vibration-Based Analytical Techniques for Gear Fault Detection

In Section 1.1.5.2, the vibration based technique was found to be the most powerful tool in detecting the defects in rotating equipment. There are mainly two vibration analysis domains reviewed in this section, known as time domain analysis and frequency domain analysis.

2.7.1 Time Domain Analysis

The time domain was the pioneer vibration analysis method before the availability of the frequency analysis. The techniques used to analysis the time domain are based on calculating different statistical parameters of the vibration signal. However, selecting the most appropriate parameter to diagnose the gearbox health effectively is a critical task and should be done carefully. The indicators that usually give accurate results are the ones that eliminate the effect of other external factors such as the machine operating conditions. Those parameters are expected to provide a certain value at a certain deterioration level and have a defined and significant trend when that level increases. Thus, the health condition and the life cycle of the machine can be easily identified. There are some widely used parameters such as peak, crest factor (CF), root mean square (RMS), and kurtosis (KU).

The peak value of the signal is defined as half the difference between the maximum and minimum vibration levels and is calculated as [43]:

$$\text{Peak} = \frac{1}{2}\ (\max\ (x(t)) - \min(x(t))) \qquad \text{Eq. 20}$$

where x(t) is the time domain signal.

The RMS, which measures the energy level of a signal defined as the square root of the arithmetic mean of the squares of the signal's amplitude, is expressed as [37]:

$$\text{RMS} = \sqrt{\frac{1}{N}\sum_{n=1}^{N}(x(n))^2} \qquad \text{Eq. 21}$$

where N is the number of samples taken in the signal, x(n) is the amplitude of the signal for the nth sample, and the mean of the signal is zero.

The CF is defined as the ratio of the crest value to the RMS of the signal [43]:

$$\text{CF} = \frac{Crest\ value}{RMS} = \frac{sup|x(n)|}{\sqrt{\frac{1}{N}\sum_{n=1}^{N}[x(n)]^2}} \qquad \text{Eq. 22}$$

where sup $|x(n)|$ represents the maximum absolute value of the signal.

The kurtosis is a powerful tool which is independent of the operating conditions and has given accurate indications when used to diagnose the bearings. The KU is a normalized form of the fourth central moment, it is more sensitive to the peakedness of the signal than the other parameters, and is calculated as [43]:

$$\text{KU} = \frac{\frac{1}{N}\sum_{n=1}^{N}(x(n)-\bar{x})^4}{\left[\frac{1}{N}\sum_{n=1}^{N}(x(n)-\bar{x})^2\right]^2} \qquad \text{Eq. 23}$$

Another two indicators that are not widely used but they are more sensitive in certain conditions than the CF, are the Shape Factor (SF) and the Impulse Factor (IF). They are defined as [43]:

$$\text{SF} = \frac{RMS}{\frac{1}{N}\sum_{n=1}^{N}|x(n)|} \qquad \text{Eq. 24}$$

$$\text{IF} = \frac{Peak}{\frac{1}{N}\sum_{n=1}^{N}|x(n)|} \qquad \text{Eq. 25}$$

There are other two newly adopted parameters developed to diagnose the bearings health conditions as the other scalar indicators can only be used up to a certain deterioration stage and then their sensitivity decreases as the degradation increases. Those indicators are called TALAF and THIKAT, and they combine other common indicators [43]. These indicators are defined as:

$$\text{TALAF} = log\left[Kurtosis + \frac{RMS}{RMS_h}\right] \qquad \text{Eq. 26}$$

$$\text{THIKAT} = log\left[(Kurtosis)^{CF} + \left(\frac{RMS}{RMS_h}\right)^{Peak}\right] \qquad \text{Eq. 27}$$

where RMS_h is the RMS for the healthy case.

The performance of these new indicators has been investigated in detecting the gear tooth root cracks, and it was found that they are also sensitive to the crack level as shown in Figure 40. Therefore, they can be used effectively for the gear fault detection without limitation [44].

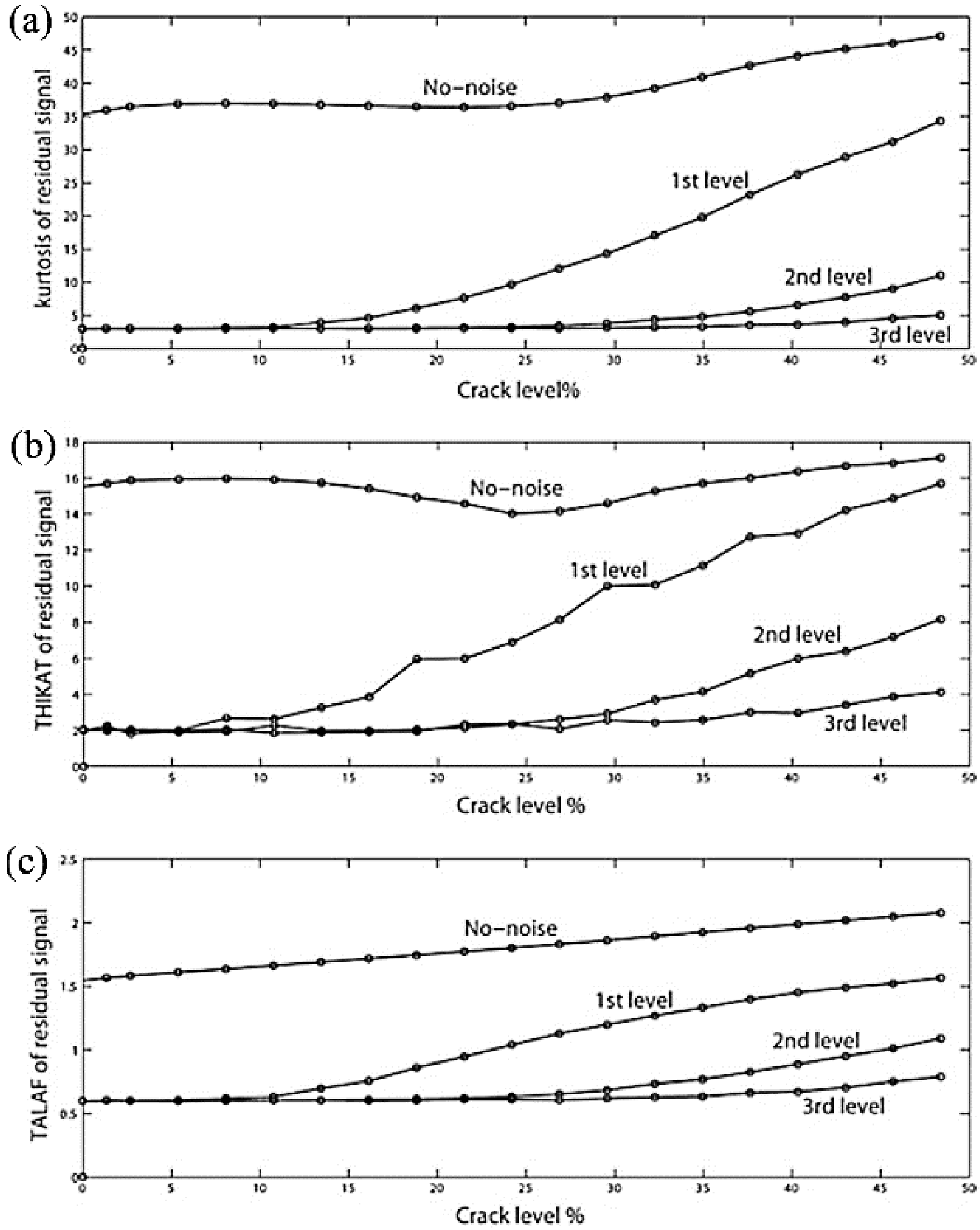

Figure 40: The performance of the fault detection indicators with the crack propagation [44]

In addition to using the original signal for analysis, the use of the residual signal is one of the main transmission diagnostic methods for determining the damage type and extent [45]. The original signal for healthy gears, which constitutes the gear meshing frequency and their shaft rotation frequency and their harmonics, dominate the meshing vibration spectrum [46]. However, when a tooth crack is present, a short duration impact will temporarily modify the vibration signal, and then the regular components of the signal become redundant for the purpose of fault detection. Thus, by removing the regular components from the signal, the fault features can be efficiently detected; the signal obtained after that is called the residual signal [47]. It is clear that the values of the statistical indicators, applied to the residual signals, increase significantly due to the presence of a tooth crack, see Figure 41.

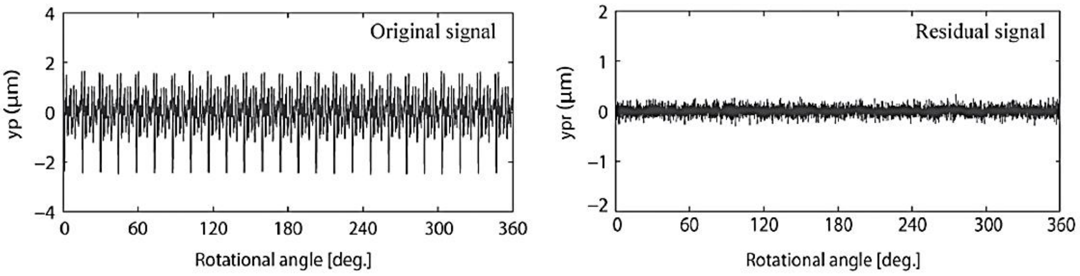

Crack depth=0.0 mm, CL=0.0%
RMS=7.181e-07, kurtosis=4.097

Crack depth=0.0 mm, CL=0.0%
RMS=0.841e-07, kurtosis=2.962

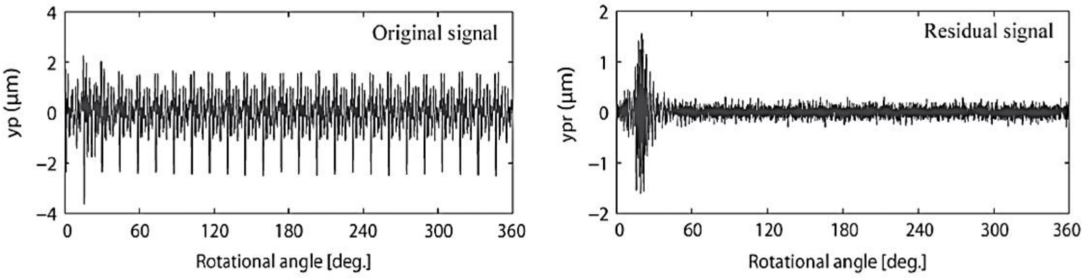

Crack depth=1.8 mm, CL=48.38%
RMS=7.239e-07, kurtosis=4.080

Crack depth=1.8 mm, CL=48.38%
RMS=1.804e-07, kurtosis=29.008

Figure 41: Original and residual signals for a healthy and faulty gear [30]

The statistical parameters are also used to identify how many DOF can be used to model the gear systems, which can give a higher sensitivity to detect the crack level accurately. Figure 42 indicates that a 6-DOF model has the highest significant sensitivity for the RMS and Kurtosis [41].

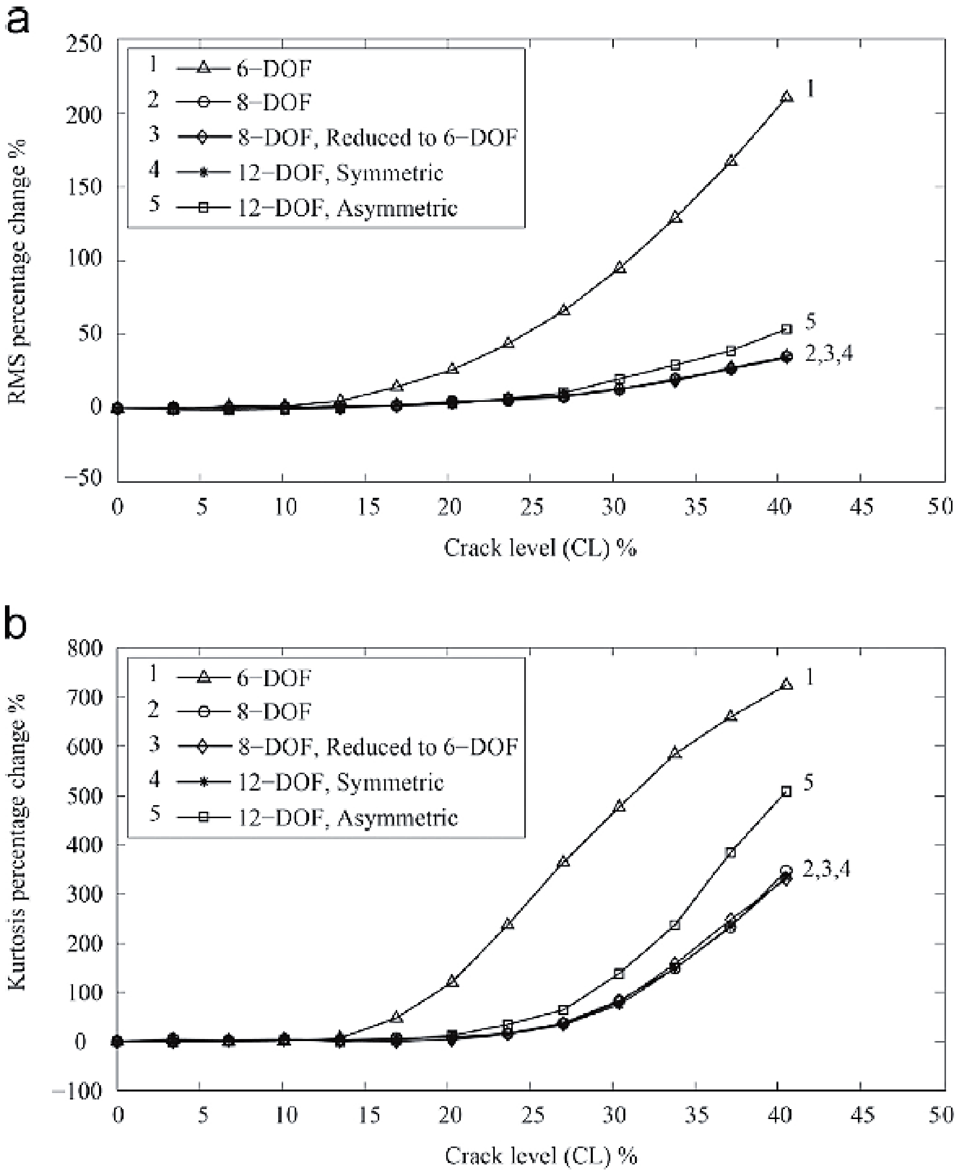

Figure 42: Performance of the statistical indicators applied to the residual signals: (a) RMS curves and (b) Kurtosis curves [41]

2.7.2 Frequency Domain Analysis

Another vibration analysis tool is the frequency domain analysis. It is a valuable tool for detecting faults in simple rotating machinery. This tool is used to break down complex signals into several frequencies to be analyzed easily, where the fault diagnosis can be simply made. The Fourier Transformation (FT) is the mathematical basis of the frequency analysis, where FT is expressed as [18]:

$$X(f) = \int_{-\infty}^{\infty} x(t)e^{-j2\pi ft}dt \qquad \text{Eq. 28}$$

where x(t) represents a continuous time domain signal, X(f) is the spectrum of x(t) and $j = \sqrt{-1}$. The FT can also isolate the influence of specific machine components to make the faults dominant. Examples of the Frequency domain analysis for cracks in gears are shown in Figure 43 and 44.

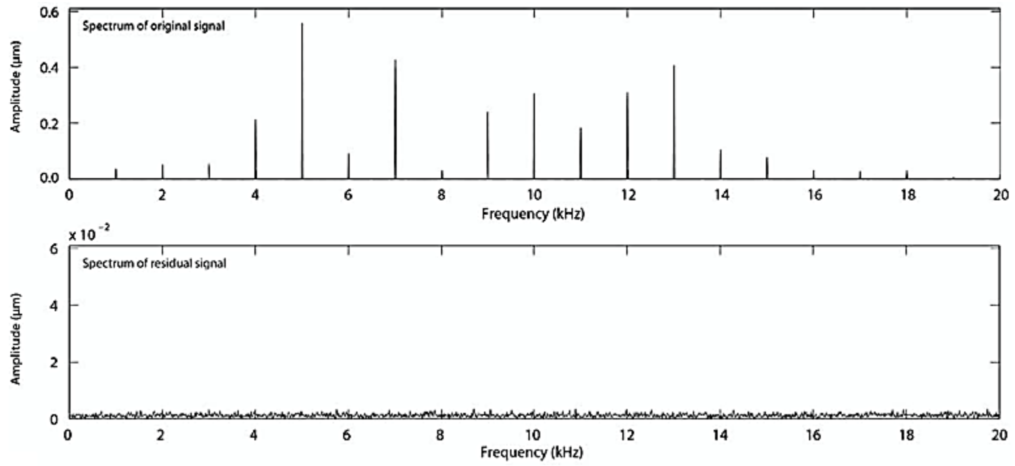

Figure 43: The spectra for a healthy gear for the original and residual signals [30]

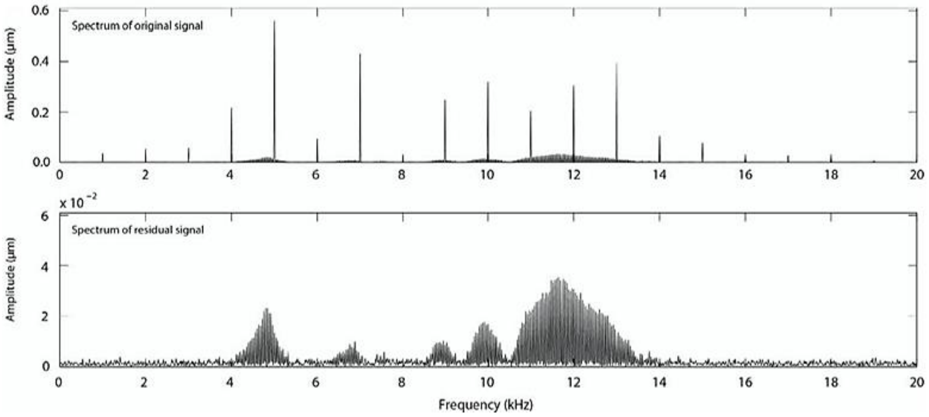

Figure 44: The spectra for a faulty gear for the original and residual signals [30]

2.8 Literature Survey Summary

In the light of the literature survey performed in this study, it can be observed that the investigation of gears dynamics in the presence of cracks attracted the interest of numerous researchers during the past ten years. To the best knowledge of the author, all the published work focused exclusively on the case of single cracks. Surprisingly, no previous work addressed the case of multiple simultaneous cracks, although it is very improbable that a single crack would reach 40% or more of the tooth width while being the only crack in the entire set of teeth.

Different approaches were used to analyze the vibration behavior of external spur gears as they are the most common gear type with simple geometrical properties. Numerical simulations are widely used as the experimental approach is costly, time-consuming, altered by many external factors, and difficult to be controlled. Numerical based models have the advantage that the approximation error is acceptable and that simulating various cases and operating conditions can be carried out in a short period. The numerical approach, for studying the effect of gear tooth cracks on the vibration signal, requires the consideration of a large number of parameters. For the sake of simplicity and efficiency, a one-stage gearbox will be studied as it is considered as the most basic form of meshing gears. The initial crack position starting at the top of the tooth root fillet will be investigated over the other possibilities, because it has the least adverse effect on the gear mesh stiffness, making it very hard to be correctly detected.

Among the different crack propagation paths reviewed, the scenario where the crack is extended through the entire tooth width with a uniform length distribution will be selected assuming that only a uniformly distributed load will be applied. Since the gear mesh stiffness is the main source of vibration, a finite element analysis will be performed to determine the stiffness variation with respect to the angular position. Such approach will be conducted for both healthy and faulty gears with different combinations of crack lengths. Moreover, this work will include the effect of the inter-tooth friction generated between the sliding surfaces of the gear teeth, with unequal load sharing which is more practical. From Sections 2.6 and 2.7.1, it was concluded that a 6 DOF model, that has 3 DOF (two translations and one rotation) for each gear, is the simplest model that can include the effect of friction and has the highest sensitivity to the statistical time domain parameters. Moreover, based on the surveys of vibration-based fault diagnostic techniques, it has been concluded that time domain analysis is simple, fast and inexpensive mean of fault detection and does not require sophisticated analysis instruments. Furthermore, the time domain analysis has the advantage that several statistical indicators can be used to indicate the gearbox health. A comparison between the sensitivity of those indicators will be clarified in this study. Also, the frequency domain analysis will be introduced to investigate its sensitivity to the existence of tooth cracks and compare it with the time domain analysis.

Chapter 3. THEORETICAL AND NUMERICAL DEVELOPMENTS

The theoretical and numerical developments are discussed in this chapter, starting from basic calculations to get the gears geometry, then generating the involute curve, after that identifying the contact region between the gears, then aligning the gears correctly and finally calculating the contact points during a gear period.

3.1 Gears Nomenclature

The basic terminology associated with gears and gearing systems is illustrated in Figure 45 and 46. These nomenclatures are defined in [6], along with the equations needed to calculate them. The gearset geometrical parameters are needed as they will be used in the gears modeling in SolidWorks that will pave the way for the Finite Element Analysis (FEA) that will be explained in a later chapter.

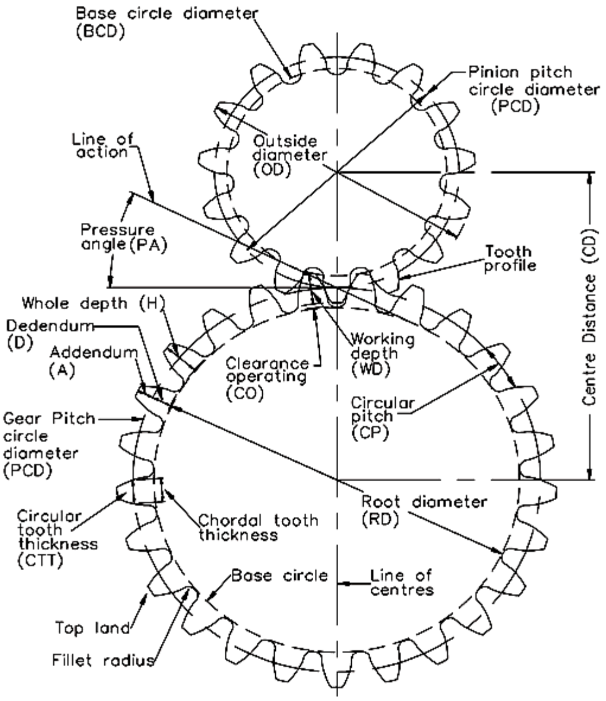

Figure 45: Gear Terminology [48]

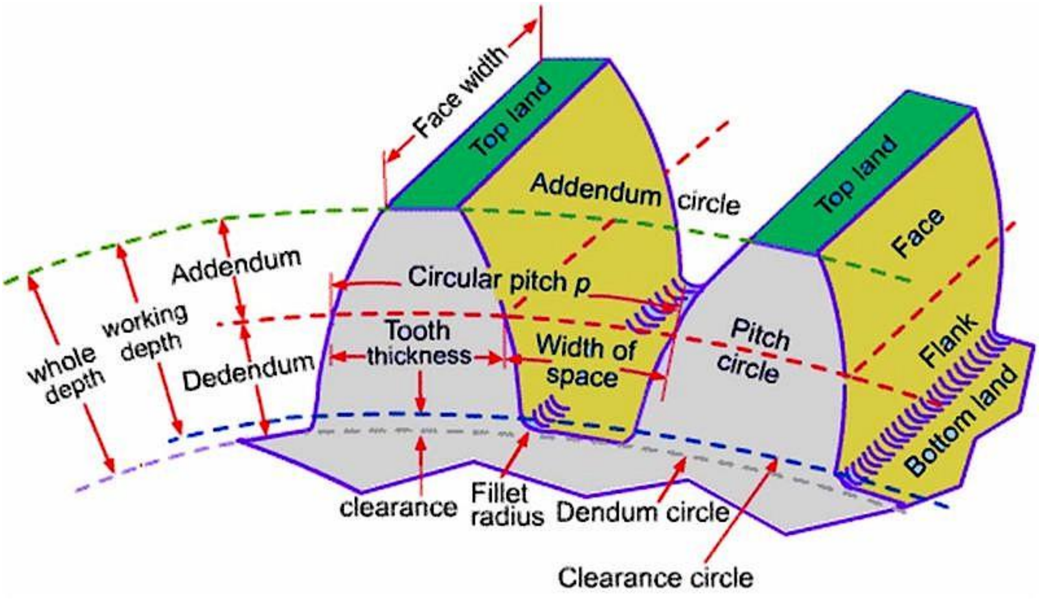

Figure 46: Gear tooth parameters [49]

3.2 Numerical Gearset Generation

The program developed using a MATLAB code was constructed using the defragmentation method, where different subprograms are developed to execute specific tasks. These subprograms are linked together to share certain variables and transfer data between each other effectively. Such strategy of programming avoids the congestion of tasks made by one single program file for which the troubleshooting of errors becomes tough.

3.2.1 Gearset Geometrical and Design Parameters Implementation

The first subprogram stores all the parameters that characterize the gearset. In addition, it does some basic calculations, such as the gear design parameters, the derived tooth constants for both the gear and the pinion, and other variable parameters. Thus, all the geometrical parameters of the gearset are obtained to be used later by other subprograms. The gear design parameters section contains all the design requirements, such as the number of pinion and gear teeth, the module, and pressure angle. In the derived constant tooth parameters section, all the constant parameters for both the pinion and the gear are included such as diametral pitch, the addendum and the dedendum, clearance, and whole depth. The last section contains the rest of the outputs, such as the outer diameter, the pitch diameter, the base diameter, the root diameter, and the circular tooth thickness.

3.2.2 Relations of the Involute Curve and Involute Angles Calculation

As shown in Figure 47, the involute curve is generated by point V of the straight line which rolls over the base circle clockwise. The lateral represents its respective side of the tooth. The equations of the involute curve can be derived from Figure 47, where Ra is the radius of the outer circle of gear, Rb is the base radius, β is the angle of rotation in rolling motion, and θ is the angle of the involute profile. Representation analysis to derive the involute curve is according to the following considerations.

The point F of the involute curve is determined by the vector equation:

$$\overrightarrow{\mathrm{FO}} = \overrightarrow{\mathrm{OP}} + \overrightarrow{\mathrm{PF}} \quad \text{Eq. 29}$$

As mentioned previously due to rolling without sliding, line $\overrightarrow{\mathrm{PF}}$ equals to arc $\widehat{\mathrm{V\,P}}$ so:

$$\overrightarrow{\mathrm{PF}} = \widehat{\mathrm{V\,P}} = \mathrm{Rb}.\beta \quad \text{Eq. 30}$$

As Ra and Rb are known from the gear properties, the value of γ can be evaluated by:

$$\mathrm{Ra} = \frac{\mathrm{Rb}}{\cos\gamma} = \mathrm{Rb}\sec\gamma \qquad \text{Eq. 31}$$

$$\overrightarrow{\mathrm{PF}} = \mathrm{Rb}\tan\gamma \qquad \text{Eq. 32}$$

$$\mathrm{Rb}.\beta = \mathrm{Rb}\tan\gamma \qquad \text{Eq. 33}$$

$$\beta = \tan\gamma \qquad \text{Eq. 34}$$

$$\theta = \beta - \gamma \qquad \text{Eq. 35}$$

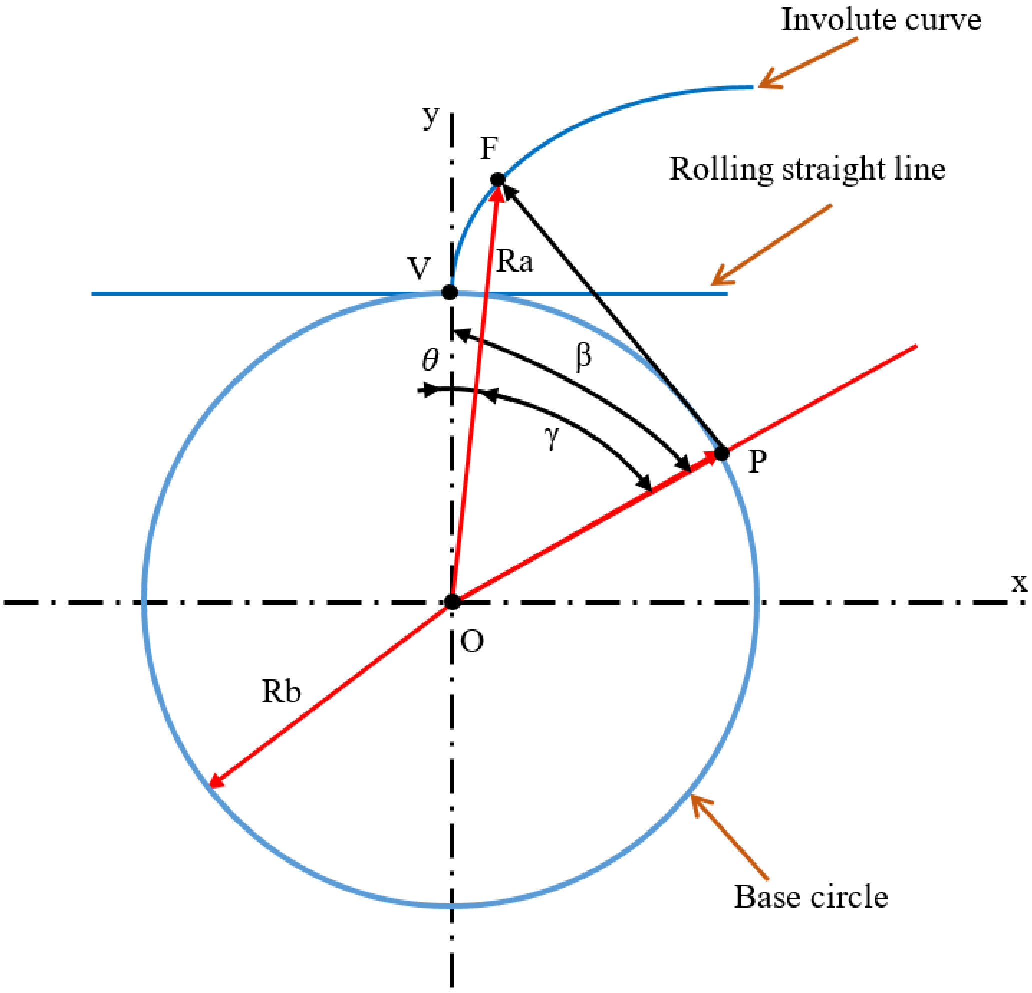

Figure 47: Involute curve geometrical relations

After getting all the critical parameters, the equations needed to generate the involute curve can be obtained. In polar coordinates (θ, r) the involute curve has the parametric equations:

$$\mathrm{r}(\gamma) = \frac{\mathrm{Rb}}{\cos\gamma} \qquad \text{Eq. 36}$$

$$\theta(\gamma) = \tan\gamma - \gamma \qquad \text{Eq. 37}$$

Also in the Cartesian coordinate, there are two equations which are a function of θ:

$$\mathrm{X}(\theta) = \mathrm{R}\sin\theta \qquad \text{Eq. 38}$$

$$\mathrm{Y}(\theta) = \mathrm{R}\cos\theta \qquad \text{Eq. 39}$$

The relationship between the polar coordinates, the angle and the radius, has to be identified first to draw the gears. Since the involute of a circle in Cartesian coordinates has the following parametric equation:

$$x = R_b[\cos(\beta) + \beta sin(\beta)] \qquad \text{Eq. 40}$$

$$y = R_b[\sin(\beta) - \beta cos(\beta)] \qquad \text{Eq. 41}$$

$$R^2 = x^2 + y^2 \qquad \text{Eq. 42}$$

Therefore,

$$R^2 = {R_b}^2[(\cos(\beta) + t\sin(\beta))^2 + (\sin(\beta) - \beta\cos(\beta))^2] \qquad \text{Eq. 43}$$

$$\frac{R^2}{{R_b}^2} = [\Big(\cos(\beta))^2 + 2\beta\sin(\beta)\cos(\beta) + \beta^2(\sin(\beta)\Big)^2 + (\sin(\beta))^2 - 2\beta\sin(\beta)\cos(\beta) + \beta^2\cos(\beta)^2] \qquad \text{Eq. 44}$$

$$\frac{R^2}{{R_b}^2} = \beta^2 + 1 \qquad \text{Eq. 45}$$

$$\beta^2 = \frac{R^2}{{R_b}^2} - 1 \qquad \text{Eq. 46}$$

$$\beta = \sqrt{\frac{R^2}{{R_b}^2} - 1} \qquad \text{Eq. 47}$$

where, β is the parametric involute angle in radians and R_b is the base radius.

Let,

$$R_b(\cos(\beta) + \beta \sin(\beta)) = R\ cos(\theta) \qquad \text{Eq. 48}$$

$$R_b(\sin(\beta) - \beta \cos(\beta)) = R\ sin(\theta) \qquad \text{Eq. 49}$$

where θ is the involute angle in degrees (starts at 0^o and increases in a counterclockwise direction) and R is the radius at which the involute curve intersects.

By dividing Eq. 41 by Eq. 40:

$$\tan(\theta) = \frac{\sin(\beta) - \beta\cos(\beta)}{\cos(\beta) + \beta\sin(\beta)} \qquad \text{Eq. 50}$$

Thus,

$$\theta = \tan^{-1}\left(\frac{\sin(\beta) - \beta\cos(\beta)}{\cos(\beta) + \beta\sin(\beta)}\right) \qquad \text{Eq. 51}$$

There are four stages for the tooth profile moving counterclockwise, the first one is the increasing involute curve, then the constant radius (outer radius) curve after that the decreasing involute and the last stage is the constant radius (base or root radius). To get the profile angles, which indicates the end of each stage, the angles at which the involute curve intersects with the pitch circle and outer circle should be calculated first.

So,

$$\theta_1 = \theta_{pitch} = \tan^{-1}\left(\frac{\sin\left(\sqrt{\frac{{R_p}^2}{{R_b}^2}-1}\right) - \sqrt{\frac{{R_p}^2}{{R_b}^2}-1}\ \mathrm{x}\cos\left(\sqrt{\frac{{R_p}^2}{{R_b}^2}-1}\right)}{\cos\left(\sqrt{\frac{{R_p}^2}{{R_b}^2}-1}\right) + \sqrt{\frac{{R_p}^2}{{R_b}^2}-1}\ \mathrm{x}\ \sin\left(\sqrt{\frac{{R_p}^2}{{R_b}^2}-1}\right)}\right) \qquad \text{Eq. 52}$$

$$\theta_2 = \theta_{outer} = \tan^{-1}\left(\frac{\sin\left(\sqrt{\frac{{R_{out}}^2}{{R_b}^2}-1}\right) - \sqrt{\frac{{R_{out}}^2}{{R_b}^2}-1}\ \mathrm{x}\cos\left(\sqrt{\frac{{R_{out}}^2}{{R_b}^2}-1}\right)}{\cos\left(\sqrt{\frac{{R_{out}}^2}{{R_b}^2}-1}\right) + \sqrt{\frac{{R_{out}}^2}{{R_b}^2}-1}\ \mathrm{x}\ \sin\left(\sqrt{\frac{{R_{out}}^2}{{R_b}^2}-1}\right)}\right) \qquad \text{Eq. 53}$$

where, θ_{pitch} is the pitch circle intersection tooth profile angle, θ_{outer} is the outer circle intersection tooth profile angle, R_p is the pitch radius and R_{out} is the outer radius.

Let,

$$\theta_0 = 0^o \qquad \text{Eq. 54}$$

Since,

$$\theta_6 = \frac{360^o}{Z} \qquad \text{Eq. 55}$$

$$\theta_4 - \theta_1 = \frac{360^o}{2\,Z} \qquad \text{Eq. 56}$$

Thus,

$$\theta_3 = (\theta_4 - \theta_1) - \big(2\ (\theta_2 - \theta_1)\big) + \theta_2 = \frac{360^o}{2\,Z} - \big(2\ (\theta_2 - \theta_1)\big) + \theta_2 \qquad \text{Eq. 57}$$

$$\theta_5 = \theta_3 + \theta_2 = \frac{360^o}{2\,Z} - \big(2\ (\theta_2 - \theta_1)\big) + (2\ \theta_2) \qquad \text{Eq. 58}$$

where, Z is the number of teeth and θ_2, θ_3, θ_5, and θ_6 , are the profile angles indicating the end of the four stages which are the increasing involute, the constant radius (outer radius), the decreasing involute, and the constant radius (root or base radius), respectively.

In the program developed, the second subprogram is responsible for calculating all the necessary angles of the tooth profile, as shown in Figure 48, which are the angle between the start of the involute profile and:

1) the intersection with the pitch circle
2) the intersection with the outer circle
3) the end of the constant radius (outer radius)
4) the other intersection with the pitch circle
5) the start of the constant radius (root or base radius)
6) the end of the constant radius (root or base radius)

This subprogram takes the geometrical properties from the previous subprogram as inputs and gives back the angles needed.

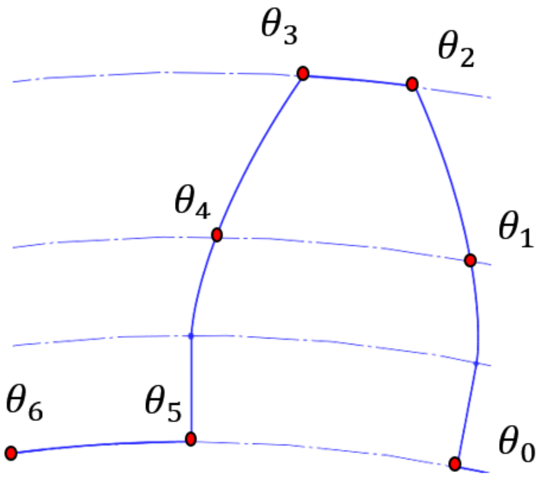

Figure 48: Tooth profile involute angles

3.2.3 Gear Profile Generation

For a certain module and pressure angle, the respective position of the base circle and the root circle will depend on the number of teeth. By equating the equation of the diameter of the base circle with that of the root circle, Eq. 59 can be obtained:

$$\text{The number of teeth} = \frac{2.5}{1 - \cos(\Phi)} \qquad \text{Eq. 59}$$

where, Φ is the pressure angle.

Thus the root circle is not always the smallest circle in the gear. For a pressure angle of 20o, the borderline case is “41 teeth”, where the root circle becomes greater than the base circle. Therefore, theoretically, the involute has already started before the dedendum or the root circle as shown in Figure 49. However, in actual practice, fillets with suitable radii are provided at the roots of the teeth to abolish the detrimental effects of stress concentration and notch effect, irrespective of whether the base circle or the root circle is the bigger of the two.

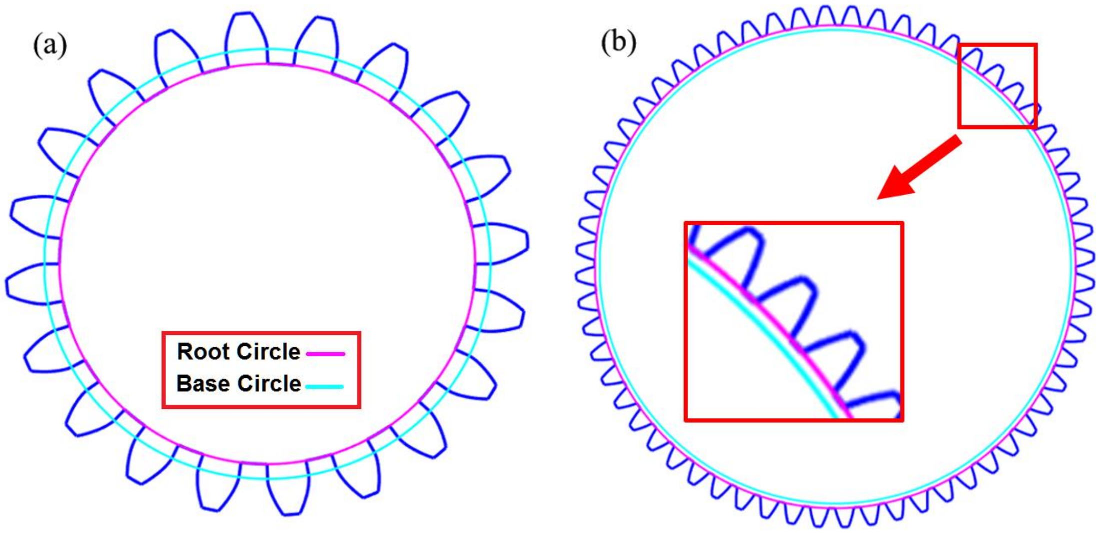

Figure 49: Schematic of spur gear tooth: (a) No. of teeth < 42, (b) No. of teeth > 42

The next subprogram is developed to get the involute tooth profile for the pinion. First, it takes the geometrical properties from the first subprogram. Then, the increasing involute part of the profile is plotted to a level exceeding the outer circle, see Figure 50, to ensure the existence of an intersecting point between both curves thus the exact and complete profile of the tooth can be plotted. After that the intersection point with the outer circle was identified, and the precise increasing involute was plotted, starting from the base circle and ends at the outer circle (Figure 51). After that, the complete pinion tooth is created according to the angles calculated previously. Then, the radius value of the space between the teeth is adjusted based on the number of teeth to be either the base or the root radius. Thus, a complete tooth with a tooth gap can be obtained.

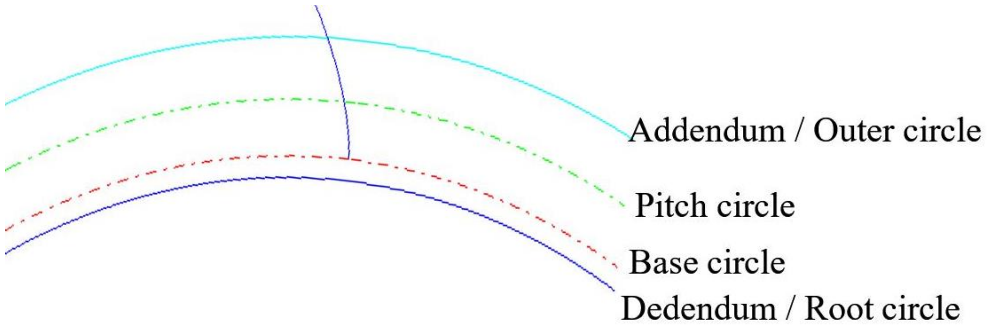

Figure 50: Involute curve exceeds the addendum circle

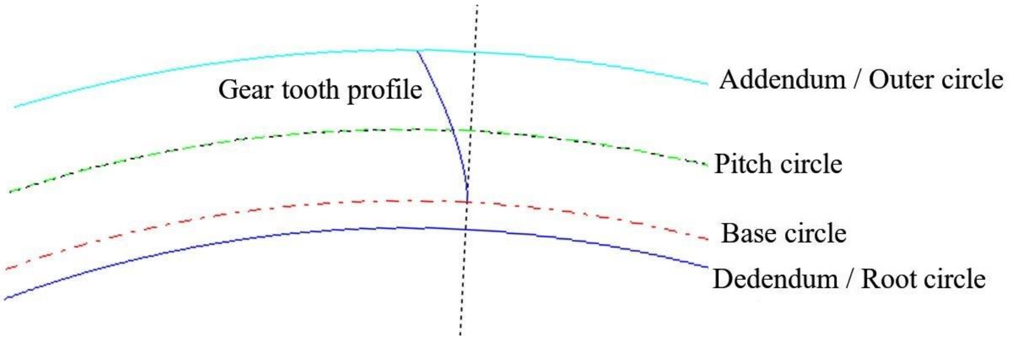

Figure 51: Correct shape of tooth profile

Finally, the tooth can be repeated around the pinion's center, according to its number of teeth. Thus the whole pinion can be plotted as shown in Figure 52. The same procedures were done for the gear as well (Figure 53).

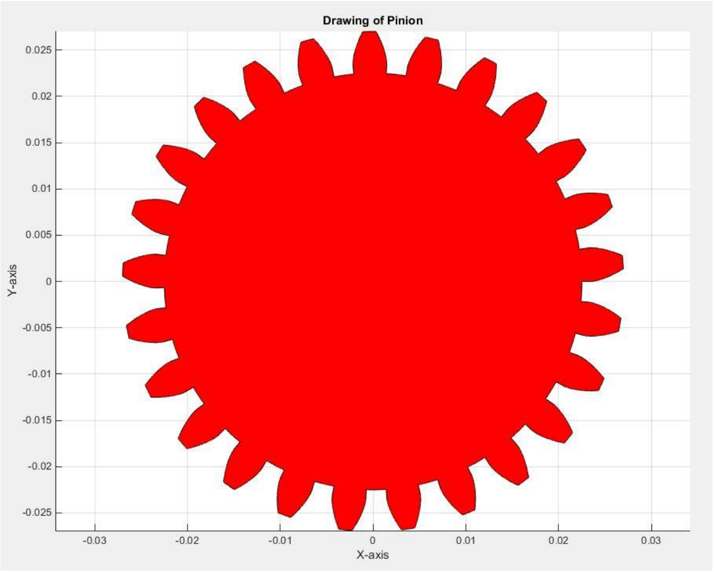

Figure 52: Generated Pinion profile

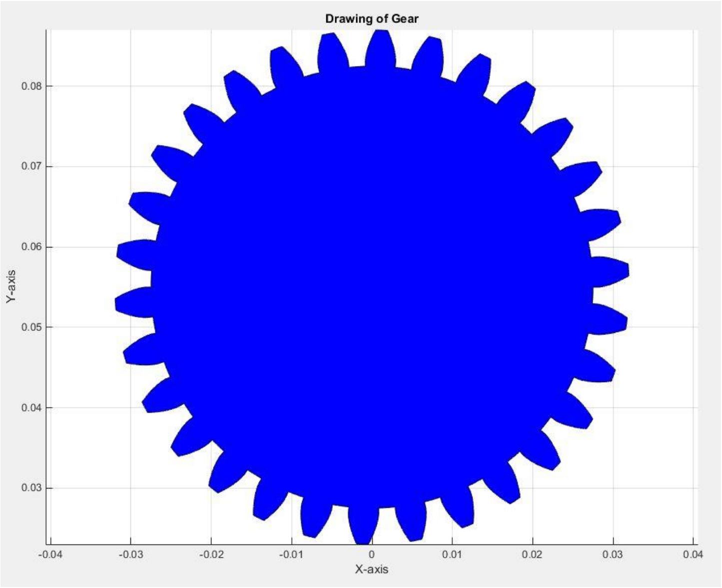

Figure 53: Generated Gear profile

3.3 Line of Action Equation Determination

The equation of the line of action can be obtained by getting two points on that line. Thus, for two gears in mesh, the line of action is tangent to both base circles of the gears. By supposing that Gear 1 is driving and rotating in a counterclockwise direction, while Gear 2 is driven. In Figure 54 the line intersects with Gear 1 and Gear 2 at *B1* (*XB1*, *YB1*) and *B2* (*XB2*, *YB2*), respectively. Thus, the coordinates of the two points B1 and B2 can be obtained as:

$$XB1 = \sin(\Phi) \cdot Rb1 \qquad \text{Eq. 60}$$

$$YB1 = \cos(\Phi) \cdot Rb1 \qquad \text{Eq. 61}$$

$$XB2 = -\sin(\Phi) \cdot Rb2 \qquad \text{Eq. 62}$$

$$YB2 = \text{Center distance} - [\cos(\Phi) \cdot Rb2] \qquad \text{Eq. 63}$$

where, Φ is the pressure angle, *Rb1* is the base radius of Gear 1, and *Rb2* is the base radius of Gear 2.

To get the slope of the line:

$$DeltaX = XB2 - XB1 \qquad \text{Eq. 64}$$

$$DeltaY = YB2 - YB1 \qquad \text{Eq. 65}$$

$$Slope = \frac{DeltaY}{DeltaX} = \frac{YB2 - YB1}{XB2 - XB1} \qquad \text{Eq. 66}$$

Since,

$$YB1 = [\, Slope \cdot XB1] + Y\text{-}intercept \qquad \text{Eq. 67}$$

$$Y\text{-}intercept = YB1 - [XB1 \cdot Slope] = YB1 - [XB1 \cdot \frac{YB2 - YB1}{XB2 - XB1}\,] \qquad \text{Eq. 68}$$

Since, the line of action equation is:

$$Y = Slope \cdot X + Y\text{-}intercept \qquad \text{Eq. 69}$$

Therefore, it can be written as:

$$Y = \frac{YB2 - YB1}{XB2 - XB1} \cdot X + [YB1 - (XB1 \cdot \frac{YB2 - YB1}{XB2 - XB1})] \qquad \text{Eq. 70}$$

These equations were programmed in MATLAB as getting the line of action equation is a crucial part in identifying the contact region and the path of contact as well.

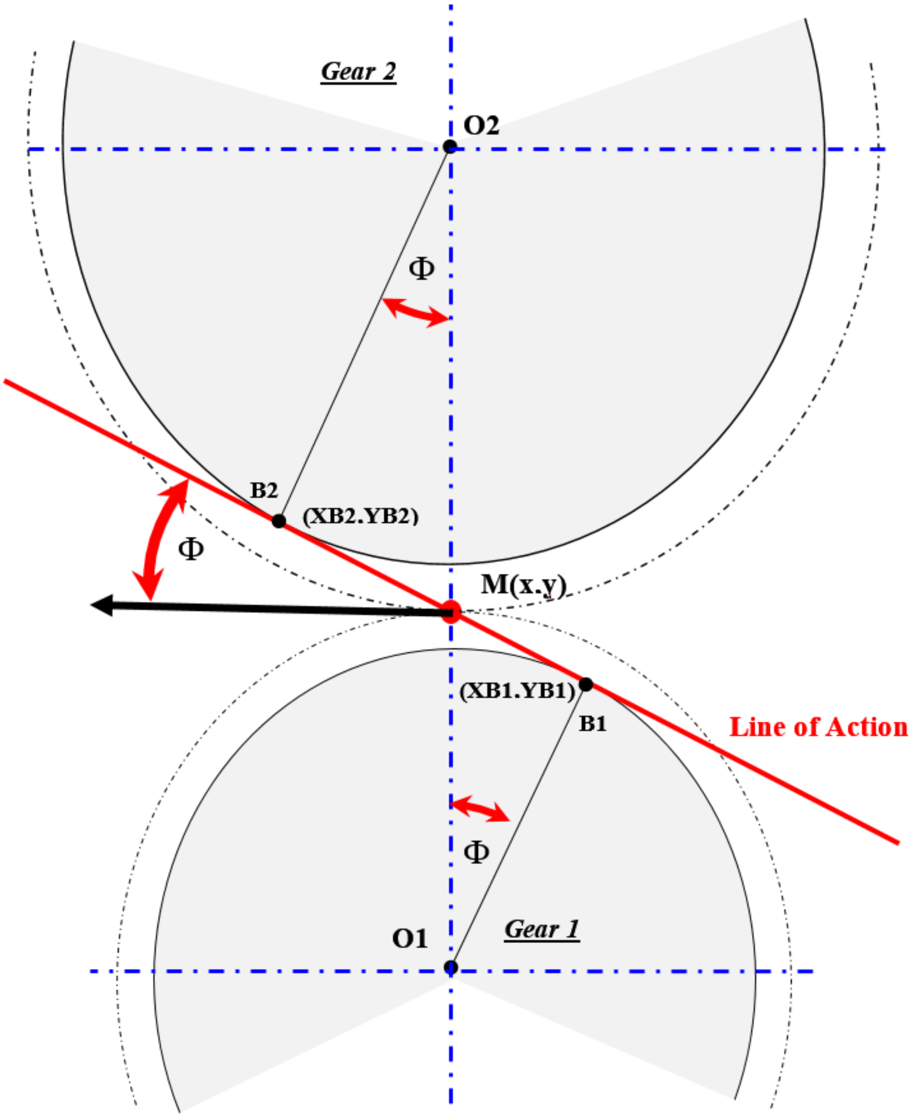

Figure 54: Line of action characteristics

3.4 Contact Region Identification

The line of action intersects with the outer circle of each gear at two points (four points of intersection in total). The angle between the two points that are nearer to the vertical axis is called the "Angle Limit", where one of the points will be the starting point of contact, and the other will be the ending point. This angle can be obtained by knowing the coordinates of the two points and the center point of each gear. In Figure 55 the angles ($\angle C1G1C2$) and ($\angle C1G2C2$) are the two "Angle Limit", and they can be obtained by the dot product between the two vectors G1C1 and G1C2 and the two vectors G2C1 and G2C2.

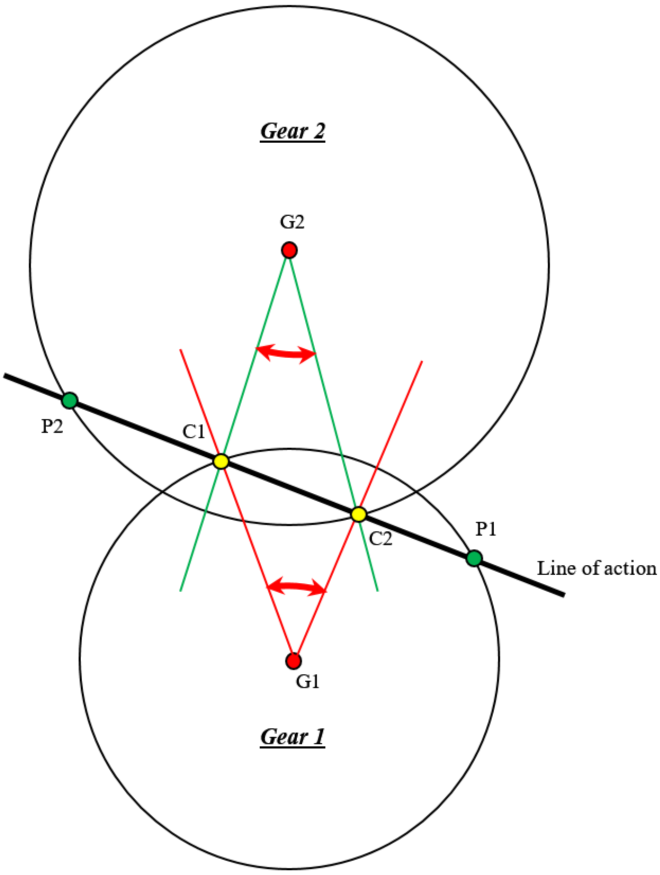

Figure 55: Line of action and the angle limits, including the path of contact

The distance along the line of action between these two points is called the path of contact, where the contact points between the gears move along this path (Figure 56).

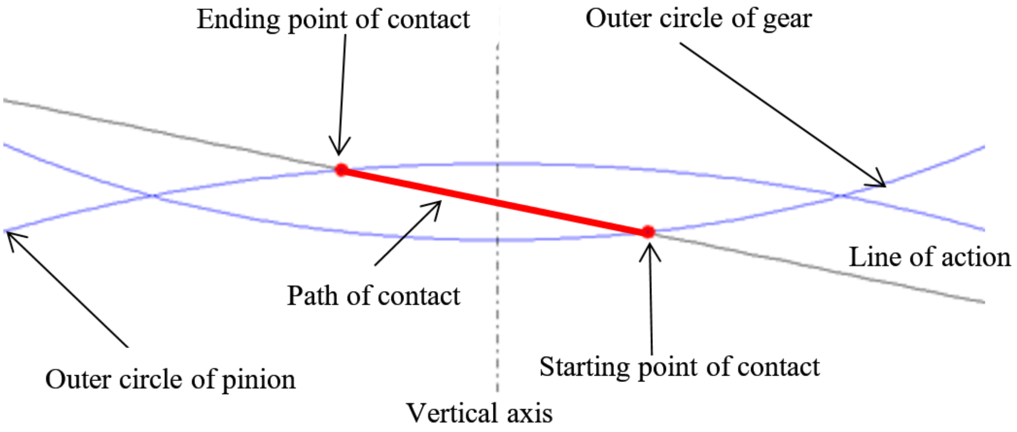

Figure 56: Location of the path of action

Another subprogram was developed to get the path of action and calculates the angle between the starting and ending point of contact. First, the line of action equation is obtained as explained in section 3.3. Then, to find the intersection point between the line of action and the outer circle, the difference between the y-coordinate of the outer circle and that of the line of action at different values of x-coordinate is calculated; where a sign change in the values indicates an intersection point. Using the pinion's outer circle gives two intersection points, and also the gear's outer circle gives two other intersection points. Thus, the four intersection points can be obtained and hence the path of contact and the Angle Limits can be found as shown in Figure 57.

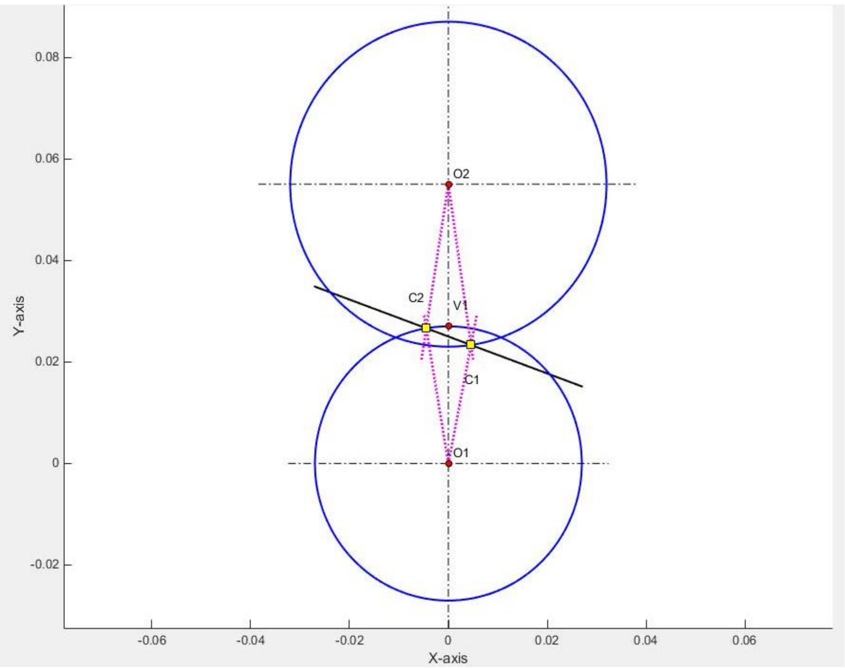

Figure 57: Angle limit plot for the Gearset

3.5 Gears Alignment

By plotting the two gears together, taking into account the center distance, it is clear that the teeth of the gears are overlapping each other, see Figure 58. The two gears must be aligned properly so that the teeth can engage correctly while rotation, where only the active flanks of the teeth of both gears are always touching. The rotation of the gears should start with an intersection at the pitch point to satisfy that condition, and consequently the overlap between the teeth can be avoided, that was done by:

1) Locating the angular position of the pinion at which an active flank in a tooth, within the contact region, is nearest to the pitch point (Figure 59).
2) Locating the angular position of the gear, at which an active flank in a tooth, within the contact region, is nearest to the pitch point.
3) Rotating each one of the gears by the angular value found previously.

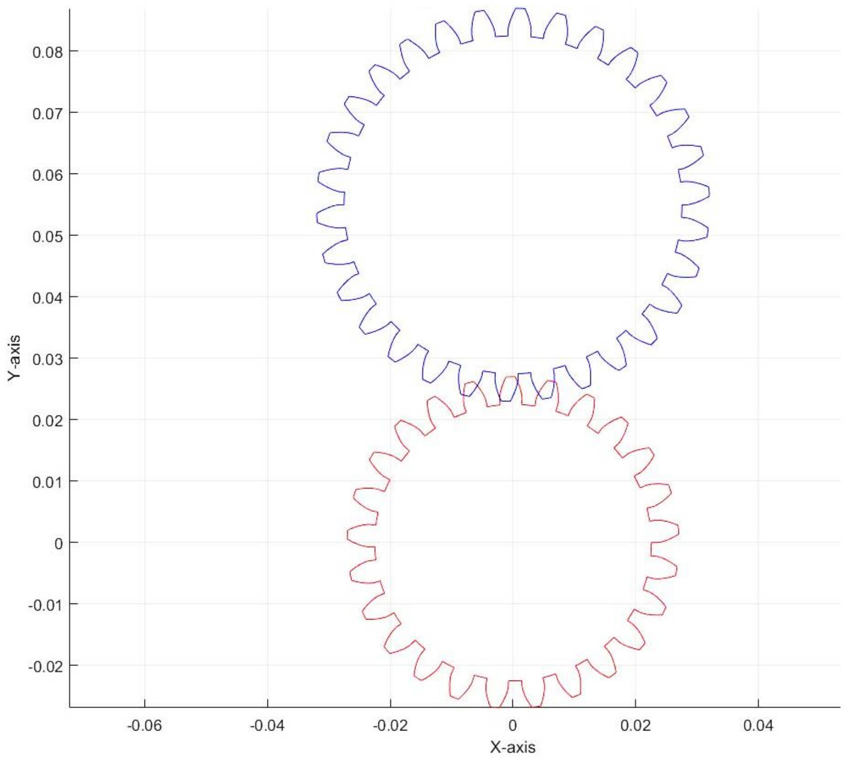

Figure 58: Gear and Pinion plot before alignment

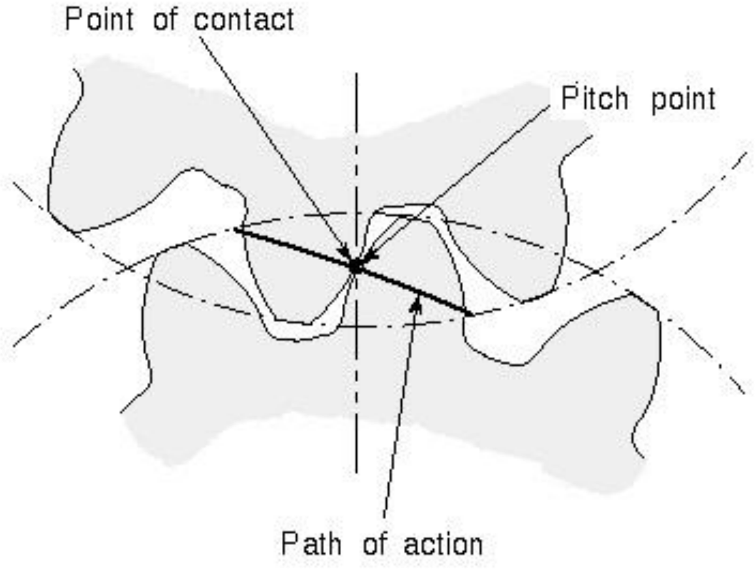

Figure 59: Point of contact along the path of action

After incorporating this in the program, the two gears became intersecting correctly at the pitch point located on the centerlines of the gears, as depicted in Figure 60.

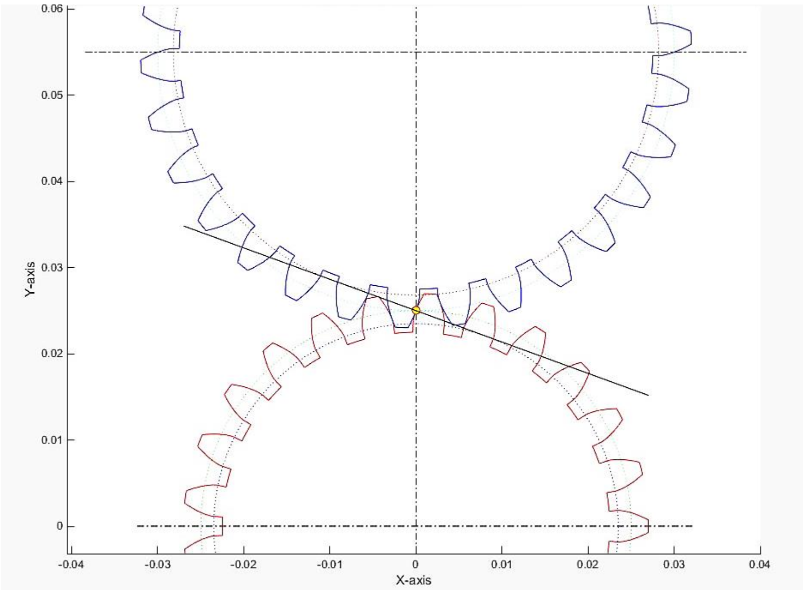

Figure 60: Gear and Pinion plot after alignment

3.6 The Contact Points Between Gears

Identifying the average contact ratio between the teeth is an essential step in any dynamic analysis or study. Knowing how many points are in contact and for how long the teeth are in contact, are critical information for determining the mesh stiffness, the friction, and the slipping velocity between teeth. The contact ratio between two meshing gears can be found using Eq. 71 [6]:

$$\text{Contact Ratio} = \frac{\sqrt{{R_{go}}^2 - {R_{gb}}^2} + \sqrt{{R_{po}}^2 - {R_{Pb}}^2} - \left([R_{gp} + R_{pp}]\ \sin\Phi\right)}{p\ \cos\Phi} \qquad \text{Eq. 71}$$

where,

R_{go} : Radius of Outside Diameter of the Gear

R_{gb} : Radius of Base Diameter of the Gear

R_{gp} : Radius of Pitch Diameter of the Gear

R_{po} : Radius of Outside Diameter of the Pinion

R_{pb} : Radius of Base Diameter of the Pinion

R_{pp} : Radius of Pitch Diameter of the Pinion

p : circular pitch

Φ : pressure angle

The contact ratio can also be found using a MATLAB code, where the main objective of this subprogram is to identify the location of the contact points and determine whether there are one or two contact points during the rotation of the gear. This can be achieved by (Figure 61):

1) Considering the pinion to be driving and the gear is driven.
2) The pinion is rotating in the counterclockwise direction.
3) In these conditions, the teeth will be active at their decreasing involute sides.
4) Whenever there is an intersection between a point on the active flank of the tooth and the line of action, this point is entitled to be a contact point.
5) If the point is located inside the angle limits of the meshing zone, this point is certainly a contact point between two teeth in mesh.

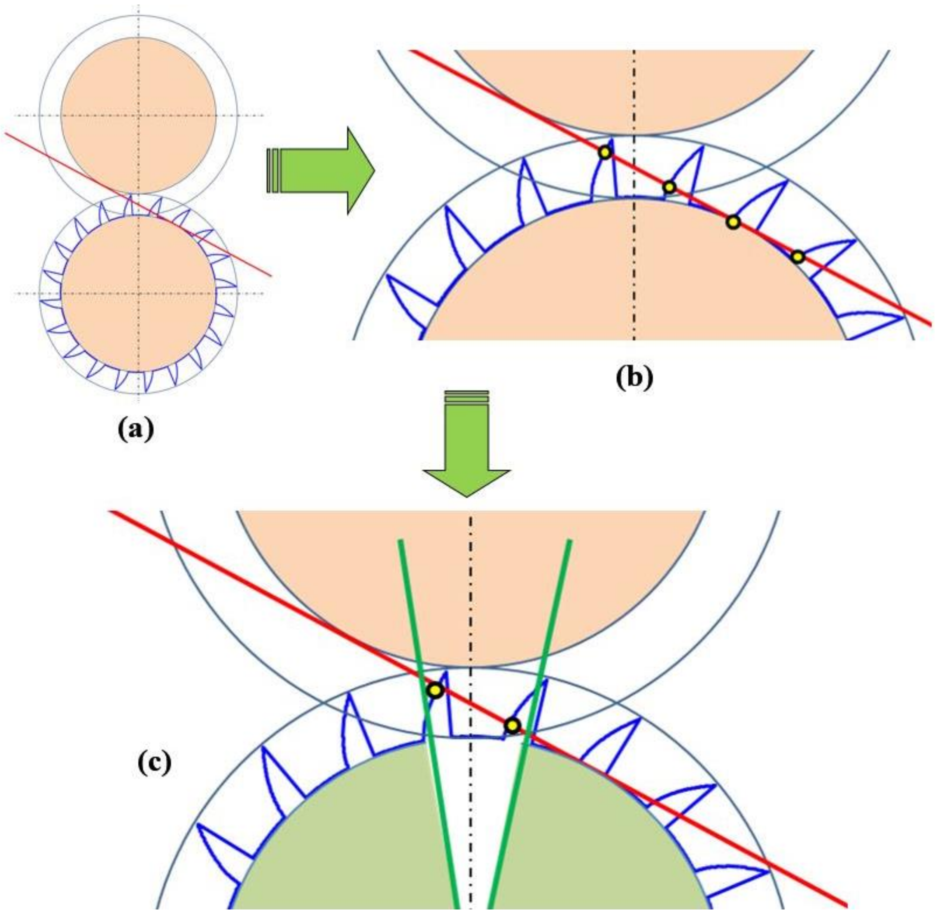

Figure 61: Contact Points Analysis: (a) Line of Action tangent to the base circles, (b) Locations entitled to be contact points, (c) Actual contact points

The subprogram has been used to identify the number of contact points, between the two gears, over one complete revolution (360 degrees). The flowchart of the code is shown in Figure 62. A typical graphical output of the subprogram is represented in Figure 63, where the contact points, the top points of the involute, and the bottom points of the teeth the line of action are highlighted in yellow, red, and green, respectively. During the rotation of both gears, the contact is taking place between two teeth at one single point or between four teeth at two different points. By plotting the number of contact points against the rotational angle, for a gearset with a module of 2 mm and 25 teeth in the pinion and 30 teeth in the gear with a pressure angle of 20^{o}, Figure 64 can be obtained. It is clear that during the rotation of the gear, there are two contact points most of the time. By taking the average value of the number of contact points along the 360^{o}, the contact ratio was found to be 1.63.

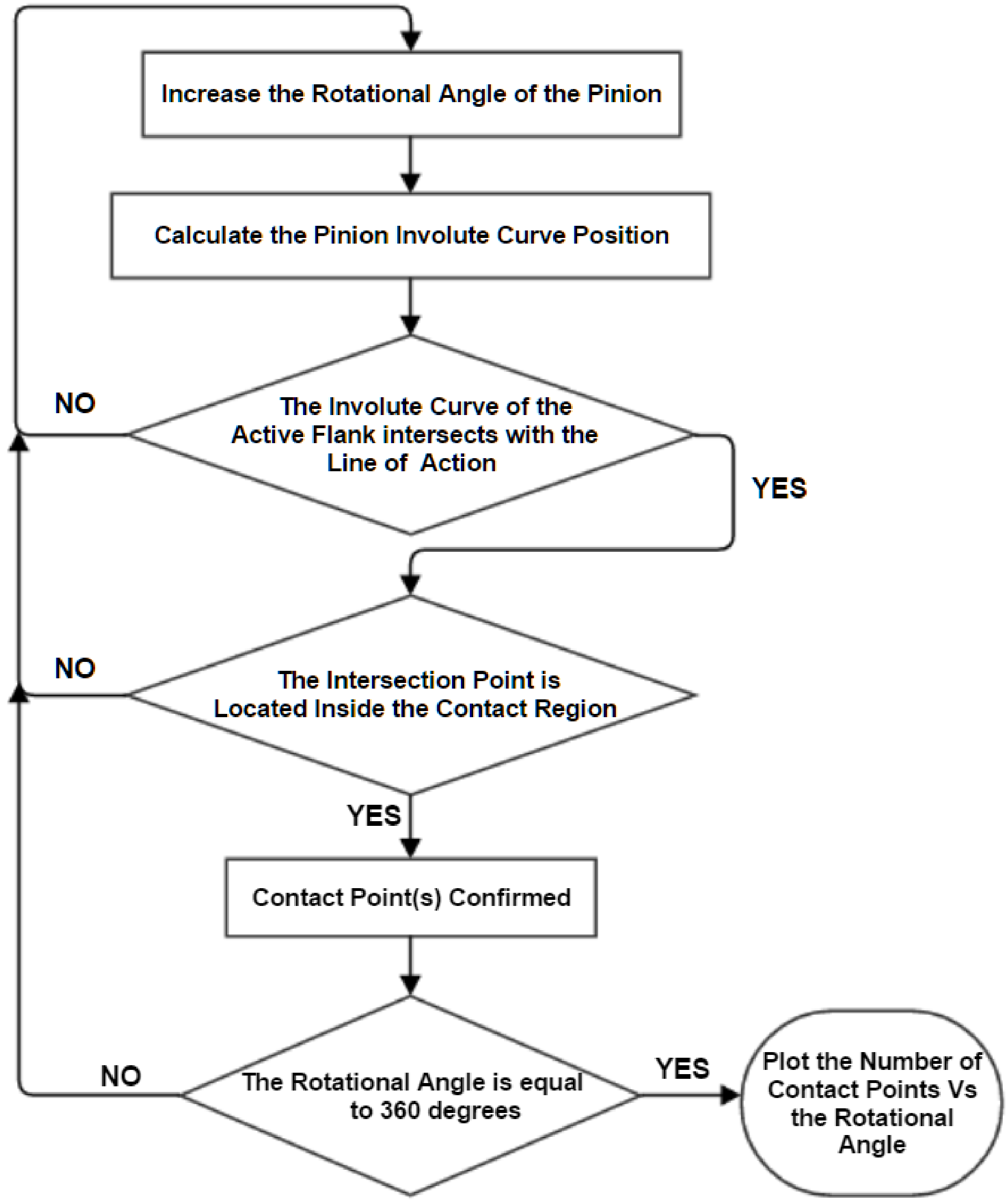

Figure 62: The flowchart for the contact analysis subprogram

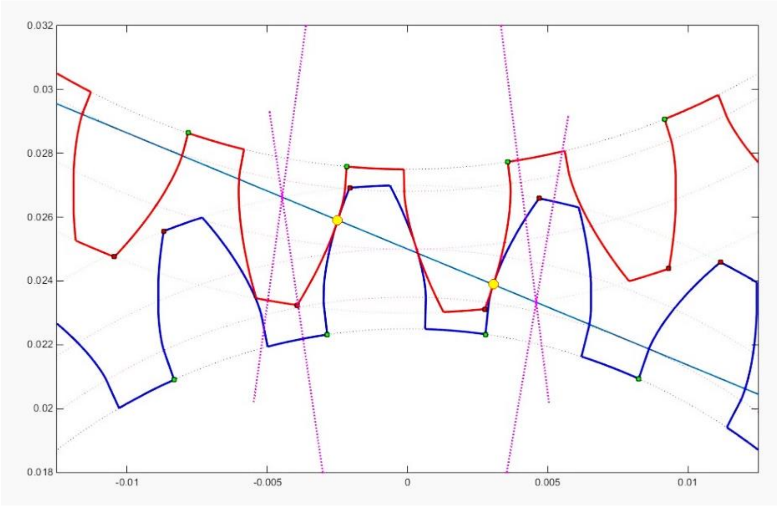

Figure 63: Contact points obtained from the developed program

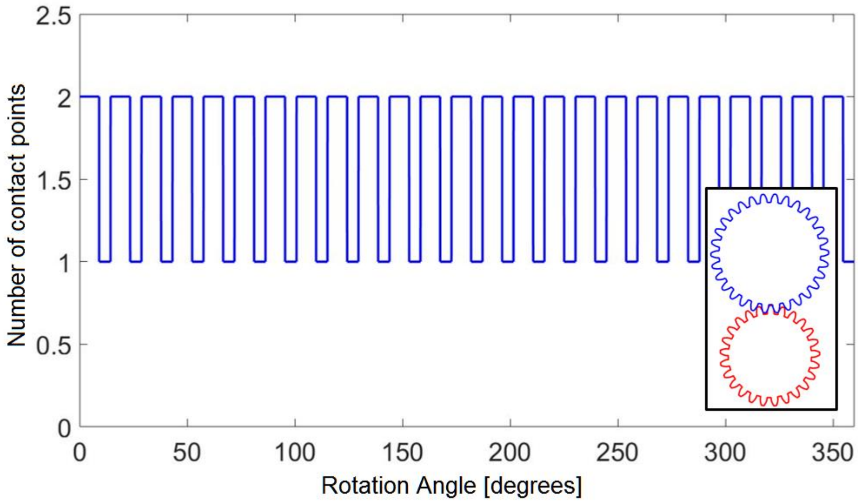

Figure 64: Contact points Vs Rotation angle for a pinion (Zp = 25) and a gear (Zg = 30)

Other numbers of teeth and gear ratios were simulated, with the same module and pressure angle, to see their effect on the contact ratio and also to validate the code used. Twenty-seven cases in total were simulated, and Figure 65 represents a sample case where contact ratio was found to be 1.7696, while by using the contact ratio equation it was equal to 1.77.

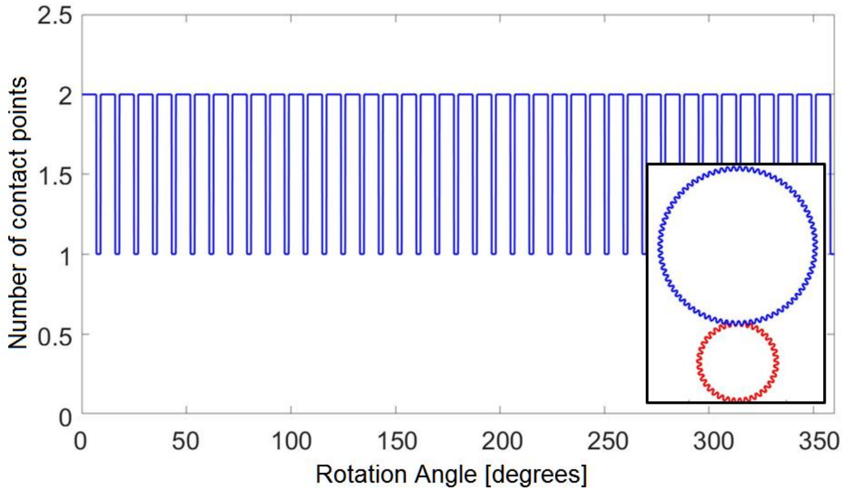

Figure 65: Contact points Vs Rotation angle for a pinion (Zp = 40) and a gear (Zg = 80)

By comparing the results obtained from Eq. 62 with those obtained from the MATLAB program, the results are almost identical as shown in Figure 66 with an error less than 0.2%, and that verifies the developed program. It can also be seen that the number of contact points and its periodicity depend strictly on the geometry of both mating gears.

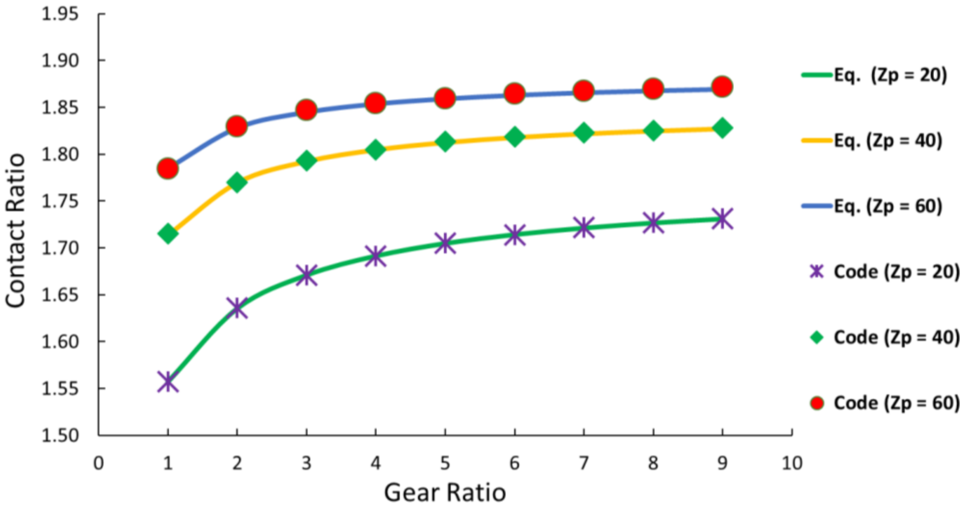

Figure 66: Contact ratio with respect to the Gear ratio

Another important parameter that will be used to calculate the time-varying mesh stiffness, which is obtained from the contact analysis, is the “Angle Ratio”. In Figure 67 suppose that:

1) θ_{1p} is the angle between the first contact point C_1 and the corresponding bottom point B_{1p} on the Pinion
2) θ_{1g} is the angle between the first contact point C_1 and the corresponding bottom point B_{1g} on the Gear
3) θ_{2p} is the angle between the second contact point C_2 and the corresponding bottom point B_{2p} on the Pinion
4) θ_{2g} is the angle between the second contact point C_2 and the corresponding bottom point B_{2g} on the Gear
5) C_s and C_e are the start and the end point of contact, respectively

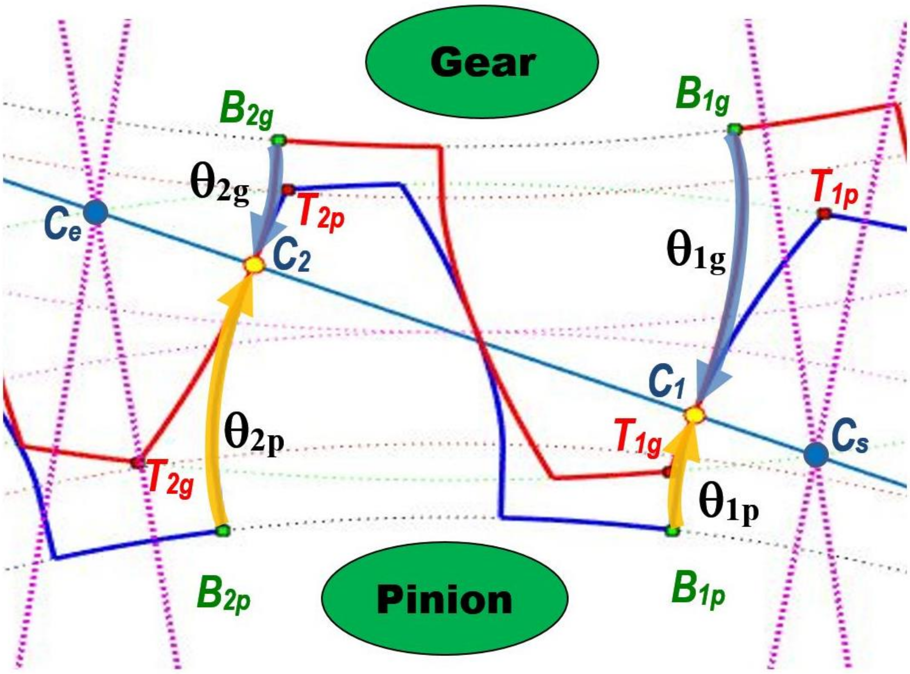

Figure 67: Contact Points and Angle Ratios

Thus, the following angle ratios can be defined from Figure 67:

$$AR_{1p} = \frac{Angle(B_{1p}, C_1)}{Angle(B_{1p}, T_{1p})} \quad \text{Eq. 72}$$

$$AR_{1g} = \frac{Angle(B_{1g}, C_1)}{Angle(B_{1g}, T_{1g})} \quad \text{Eq. 73}$$

$$AR_{2p} = \frac{Angle(B_{2p}, C_2)}{Angle(B_{2p}, T_{2p})} \quad \text{Eq. 74}$$

$$AR_{2g} = \frac{Angle(B_{2g}, C_2)}{Angle(B_{2g}, T_{2g})} \quad \text{Eq. 75}$$

By plotting the Angle Ratios, obtained from Eq. 72, 73, 74, and 75, against the rotation angle, Figure 68 and 69 can be obtained, where the variation for the Pinion's AR and the Gear's AR are opposite to each other, as when the ratio increases for the Pinion, it decreases for the Gear, and that was expected.

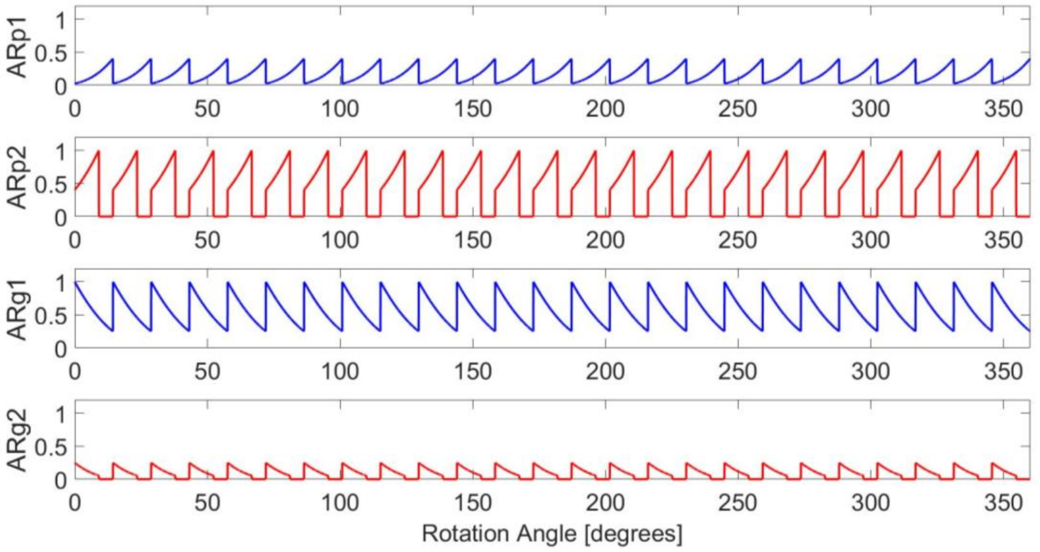

Figure 68: The four defined Angle ratios

The contact region is divided into two subregions for analysis, the first region (Region 1) starts from the contact location to the right of the pitch point during the double contact until the end of the single contact, while the second region (Region 2) starts from the contact on the left of the pitch during the double contact until the end of the double contact.

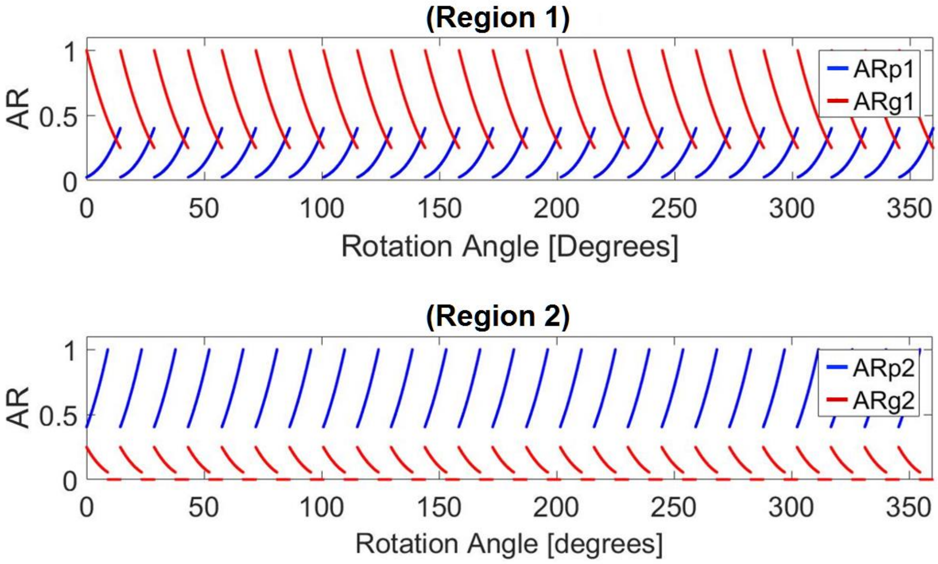

Figure 69: Angle ratios at the two contact subregions

3.7 Inter-Tooth Friction analysis

The gear meshing involves friction caused by the sliding mating teeth. The effect of friction was added, where another MATLAB subprogram was used to identify the pitch point, at which the friction becomes Zero. The friction coefficient was taken as 0.06 [32], which varies with respect to the rotational angle between -0.06 and 0.06 (Figure 70). The force ratio is an important factor in finding the friction force, as in the case of double teeth contact, the contact force is not distributed equally among the teeth, and that was found based on FEA [39]. As shown in Figure 71, the force ratio starts from 0.4 and increases till it reaches 0.6 linearly, after that a single teeth contact occurs, and the force ratio becomes unity.

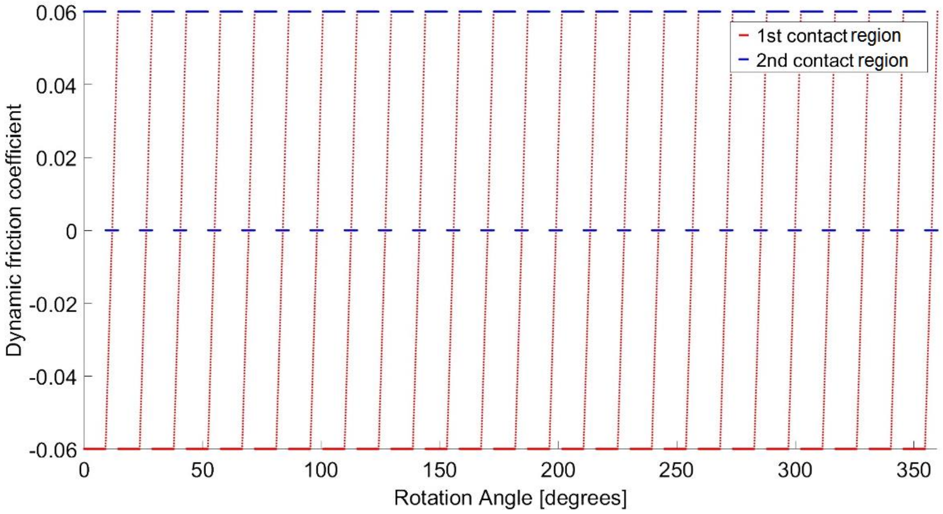

Figure 70: The dynamic friction coefficient with respect to the rotational angle

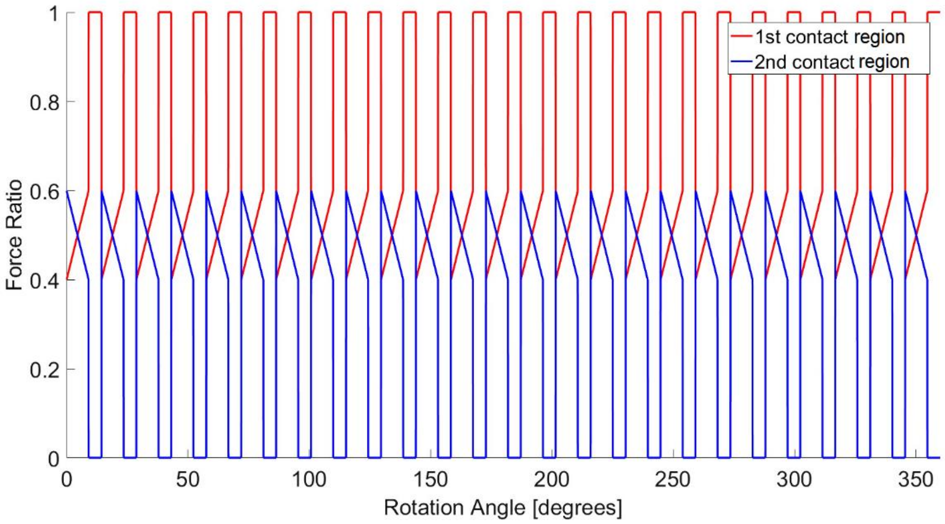

Figure 71: Force ratio at the 1st and 2nd contact subregions with respect to the rotational angle

In this study, the friction force is considered as an external force where all the dynamic effects of the normal force are excluded. The friction force can be obtained from Eq. 19, however, first the normal force has to be determined.

The transmitted force (F_T) due to the torque applied on the pinion (T_p) is given as:

$$F_T = \frac{T_p}{R_p} \qquad \text{Eq. 76}$$

where, R_P is the pitch radius of the pinion.

Therefore, the normal force (F_N) along the line of action will be constant and can be obtained as:

$$F_N = \frac{F_T}{cos(\Phi)} \qquad \text{Eq. 77}$$

where, Φ is the pressure angle.

However, the normal force is not shared equally between the teeth during the double contact (Figure 72), thus the friction force for the pinion can be calculated as:

$$F_f = \mu \cdot FR \cdot F_N \qquad \text{Eq. 78}$$

where, *FR* is the force ratio.

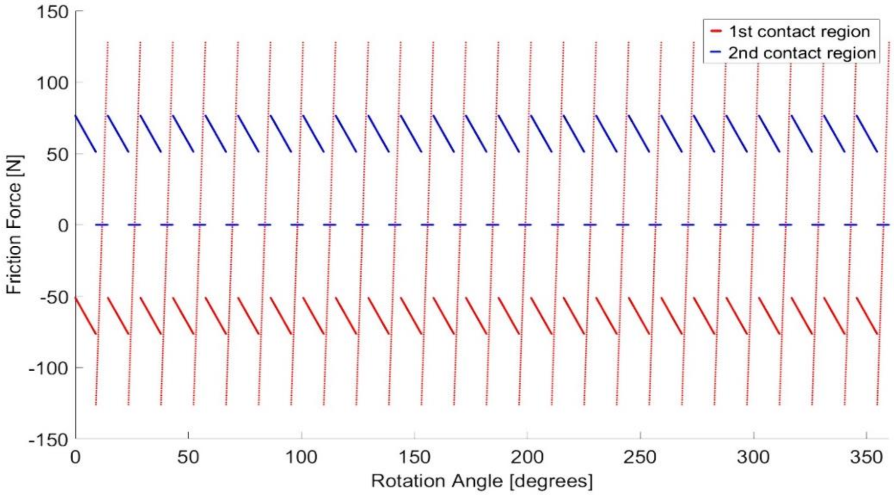

Figure 72: Friction force at the 1st and 2nd contact subregions with respect to the rotational angle

The friction force applied to the gear at the same contacting points will be the same magnitude as that of the pinion but in the opposite direction. The friction forces will also exert moments on the gears. These moments can be calculated by first identifying the moment arms, taking into consideration the contact geometry of the gear teeth (Figure 73). The Cartesian coordinates of the contact points G and H are already known from the contact analysis in addition to points O_1 and O_2, while both $\overline{O_1F}$ and $\overline{O_2I}$ can be calculated, thus, the frictional moment arms ($\overline{FG}$ and $\overline{FH}$ for the pinion, and $\overline{IH}$ and $\overline{IG}$ for the gear) can be identified.

First, the angles φ_1, φ_2, φ_3, and φ_4 are calculated using the dot product of two Euclidean vectors as shown in Eq. 79, 80, 81, and 82.

$$\varphi_1 = \frac{cos^{-1}\left(\overline{O_1G} \cdot \overline{O_1F}\right)}{\left\|\overline{O_1F}\right\|\left\|\overline{O_1G}\right\|} \qquad \text{Eq. 79}$$

$$\varphi_2 = \frac{\cos^{-1}\left(\overline{O_1H} \cdot \overline{O_1F}\right)}{\left\|\overline{O_1F}\right\|\left\|\overline{O_1H}\right\|} \qquad \text{Eq. 80}$$

$$\varphi_3 = \frac{\cos^{-1}\left(\overline{O_2H} \cdot \overline{O_2I}\right)}{\left\|\overline{O_2I}\right\|\left\|\overline{O_2H}\right\|} \qquad \text{Eq. 81}$$

$$\varphi_4 = \frac{\cos^{-1}\left(\overline{O_2G} \cdot \overline{O_2I}\right)}{\left\|\overline{O_2I}\right\|\left\|\overline{O_2G}\right\|} \qquad \text{Eq. 82}$$

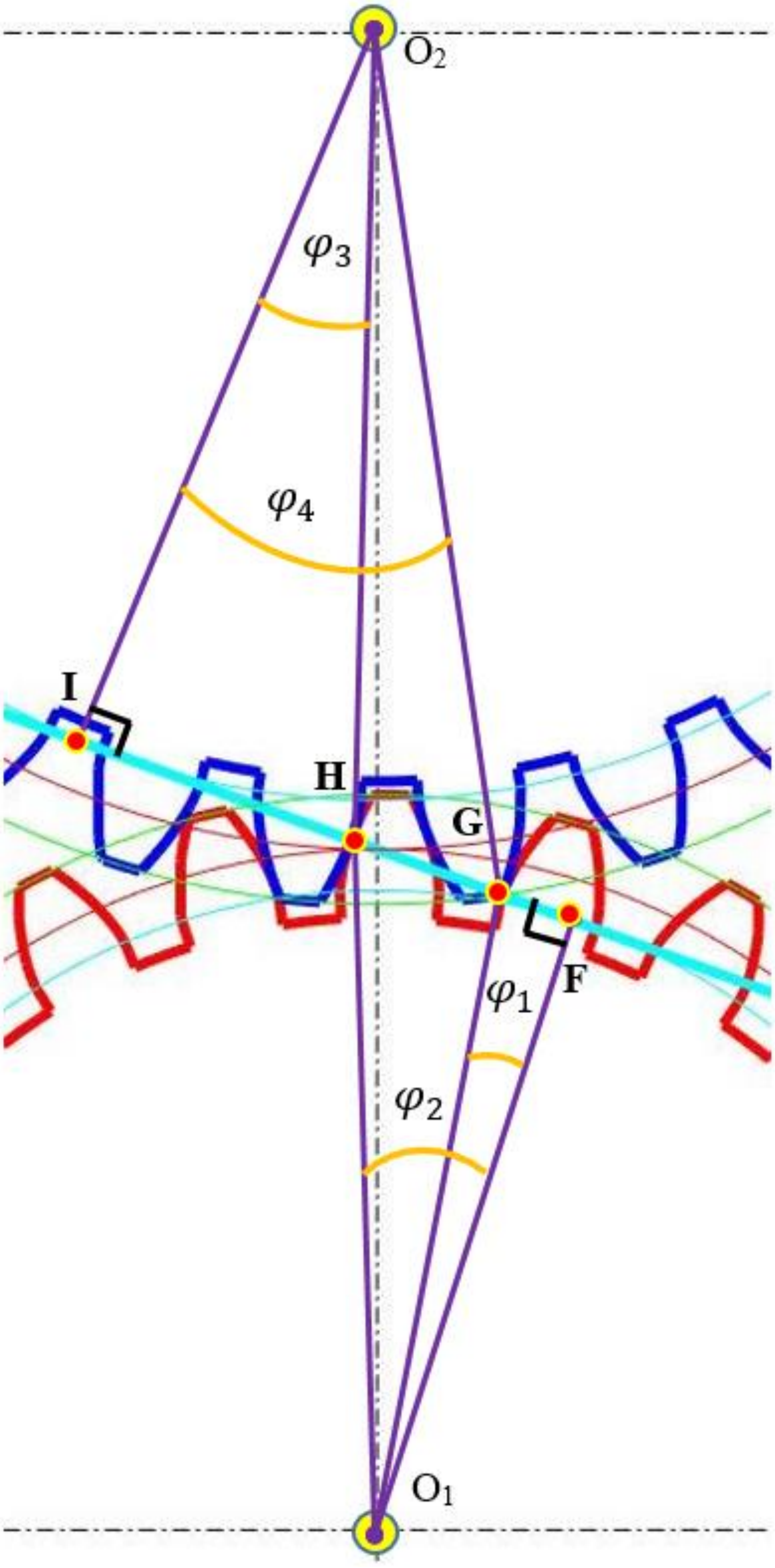

Figure 73: Contact geometry for frictional moment analysis

Thus, the frictional moment arms can be obtained as shown in Eq. 83, 84, 85, and 86.

$$\overline{FG} = \overline{O_1G} * \sin(\varphi_1) \tag{Eq. 83}$$

$$\overline{FH} = \overline{O_1H} * \sin(\varphi_2) \tag{Eq. 84}$$

$$\overline{IH} = \overline{O_2H} * \sin(\varphi_3) \tag{Eq. 85}$$

$$\overline{IG} = \overline{O_2G} * \sin(\varphi_4) \tag{Eq. 86}$$

Finally, the frictional moments are obtained by multiplying the friction force at the contact points with their respective arms. The values for the pinion and the gear are shown in Figure 74 and 75, respectively. The results of the friction forces and moments will be used in the dynamic model which will be deliberated in a later chapter.

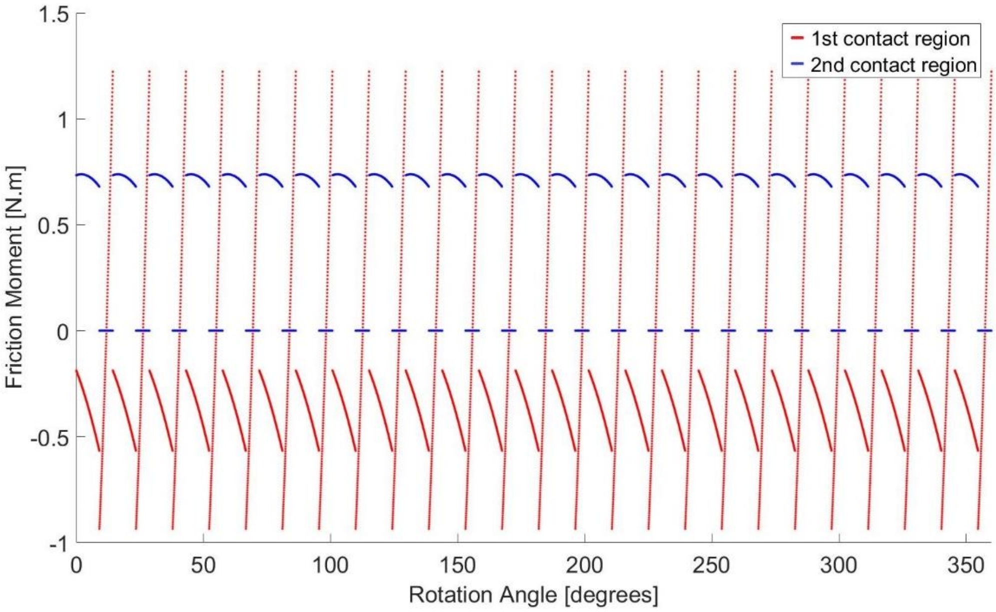

Figure 74: Friction moment for the pinion at the 1st and 2nd contact locations with respect to the rotational angle

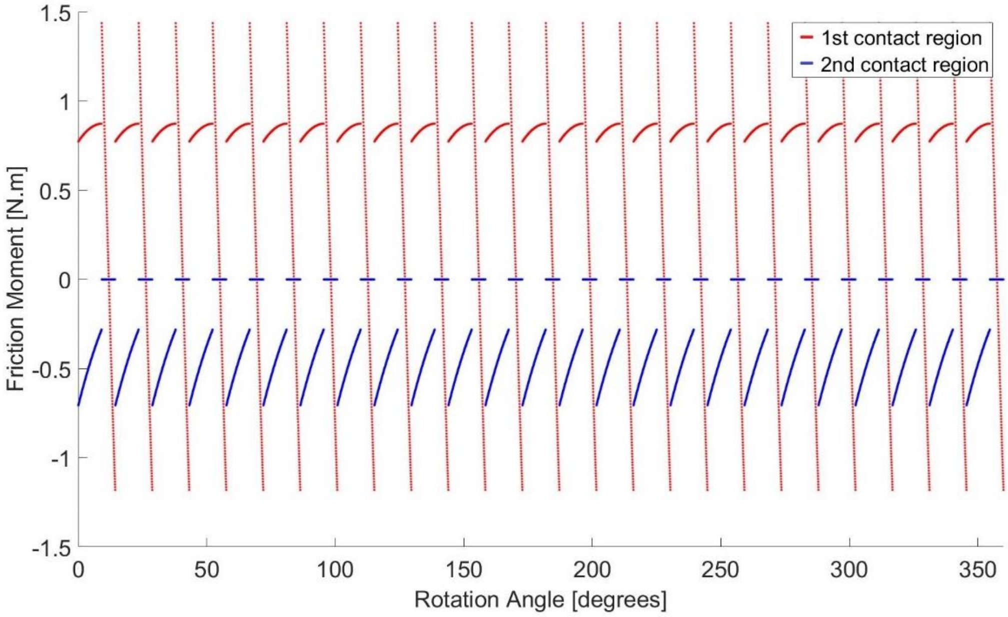

Figure 75: Friction moment for the gear at the 1st and 2nd contact locations with respect to the rotational angle

In this chapter, all the geometrical properties of the gearset were calculated. Also, the contact analysis was explained and the results were verified with the theoretical values. Finally, the inter-tooth friction was considered, and both the fiction force and moment for the sliding teeth were obtained.

Chapter 4. GEAR MESH STIFFNESS MODELING INCLUDING CRACKS

This chapter discusses the crack propagation scenario and the gear parameters considered in this study. Then it shows how the gear mesh stiffness is calculated using the FEM along with the MATLAB program developed. Finally, the results are compared with the previous studies in the literature to validate the results obtained.

4.1 Crack Modeling

In this study, cracks were only modeled for the pinion since it is more susceptible to tooth cracks than the gear when both are made of the same material. Assuming that the crack will propagate through the whole tooth width with a constant length and thickness, and a crack propagation angle of 20° as presented in [28, 30, 36]. Moreover, the crack starts at the top of the root fillet and changes its direction after reaching the center line of the tooth. Then, propagates towards the top of the root fillet on the other side, moving in straight lines [29], as shown in Figure 76. The parameters used in the gears modeling are given in Table 2.

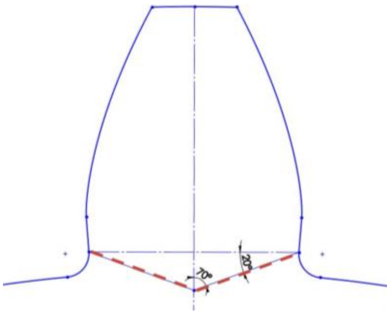

Figure 76: Crack propagation path

Table 2: Gear parameters used [28]

Parameter	**Pinion**	**Gear**
Number of teeth	25	30
Gear type	Standard involute (Full-Depth Teeth)	
Material	Steel	
Pressure angle (degree)	20	
Face width (mm)	20	
Module (mm)	2	
Elastic modulus (N/m^2)	2×10^{11}	
Poisson's ratio	0.3	
Contact ratio	1.63	
Crack propagation angle (degree)	20	
Fillet radius (mm)	0.4	
Backup ratio	3.3	
Crack thickness (mm)	0.01	
Crack width (mm)	20	
Total length of the crack path (mm)	3.8	

The backup ratio was taken as 3.3 to avoid the rim thickness effect on the tooth deflection, and root fillet curves are assumed to be circular. Supposing that CL is the length of the crack and PL is the total length of the crack path shown as a red dashed line in Figure 76. Thus the crack length percentage (CLP) can be obtained as:

$$\text{CLP} = \frac{CL}{PL} \times 100 \qquad \text{Eq. 87}$$

In this study, the CLP has been considered as varying from 0 to 45%, as then the tooth will suddenly break before the crack reaches 100% [29]. Different crack cases were considered, starting from 5% till 45% with an increment of 5%, a total of 9 cases.

Table 3 demonstrates a sample of the cases studied and their respected images, while the crack lengths with their respective percentages are shown in Table 4.

Table 3: Tooth root crack with different CLP

CLP (%)	Crack images	CLP (%)	Crack images
0	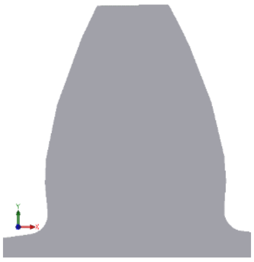	**10**	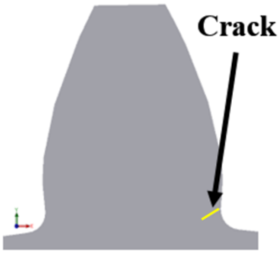
20	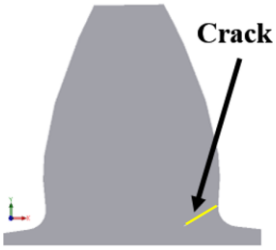	**40**	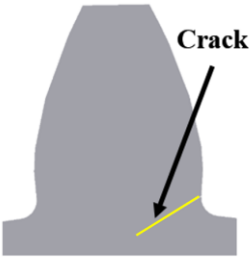

Table 4: Crack propagation data for the modeled cases

Case	Crack length (mm)	CLP (%)	Case	Crack length (mm)	CLP (%)
1	0.00	0	**7**	1.14	30
2	0.19	5	**8**	1.33	35
3	0.38	10	**9**	1.52	40
4	0.57	15	**10**	1.71	45
5	0.76	20			
6	0.95	25			

4.2 Gear Mesh Stiffness Calculation

In this study, a FEM is used to calculate the gear mesh stiffness. First, the pinion and the gear were modeled in 3D according to the data related to the geometry obtained from the MATLAB code. Then, a finite element simulation was done via SolidWorks software, where a “Static” study was performed considering the tooth as a non-uniform beam. Linear-elastic material properties were assumed as that is reasonable for metal gears. Figure 77 illustrates how the stiffness of a single tooth will be calculated, where a force is applied to one side of the tooth acting along the line of action, then from the simulation results, the deflections δ_x and δ_y can be used to get δ in the direction of the force [37].

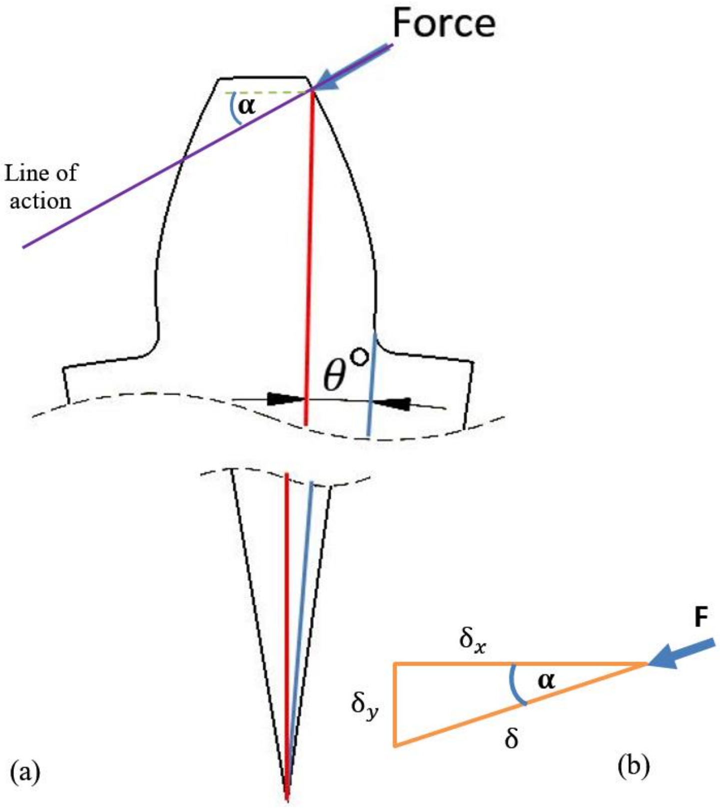

Figure 77: Transmitted Force: (a) normal to the tooth face and parallel to the line of action and (b) resolving the displacement components

As the stiffness varies with respect to the angle θ between the start of the involute curve and the location at which the force is applied on the tooth face, nine different positions, each at a time, were studied and the boundary conditions were inserted as shown in Figure 78.

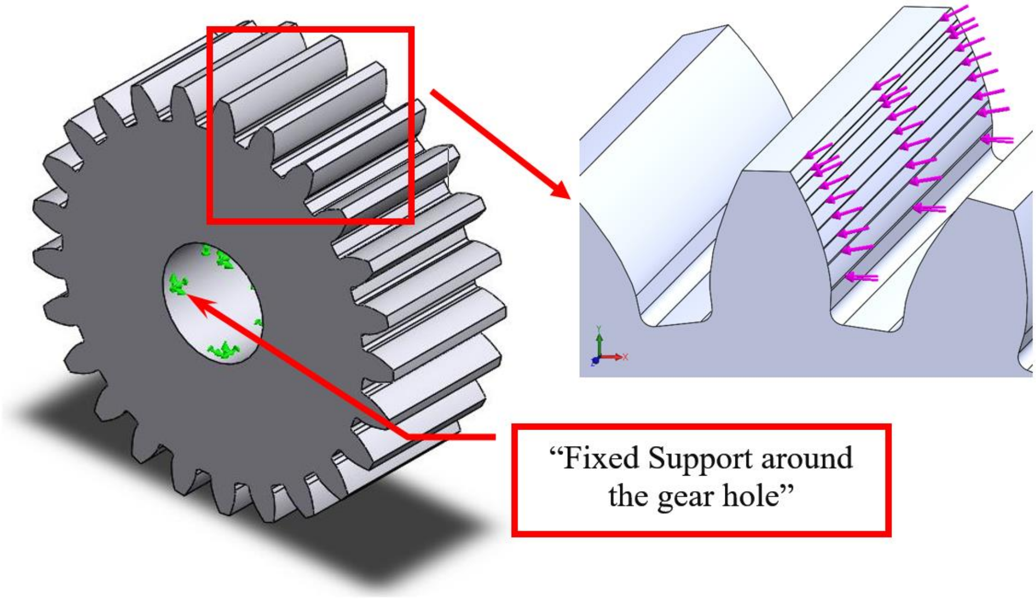

Figure 78: Different locations of the force and fixing the gear at the hole

In a finite element software, the Mesh feature can be used to control the analysis accuracy and the time of calculation through the meshing properties. The accuracy of the results increases as the number of elements increases. However, as the number of elements increases, the computational time increases. Since the crack area and the location at which the force is applied are tiny regions, the mesh density at these regions was increased using the “Mesh Control” feature in SolidWorks (Figure 79). A mesh convergence analysis was conducted decreasing the mesh element size until the difference in the deflection value in both the X and Y directions was almost 2%, the details of the final parameters used are shown in Table 5.

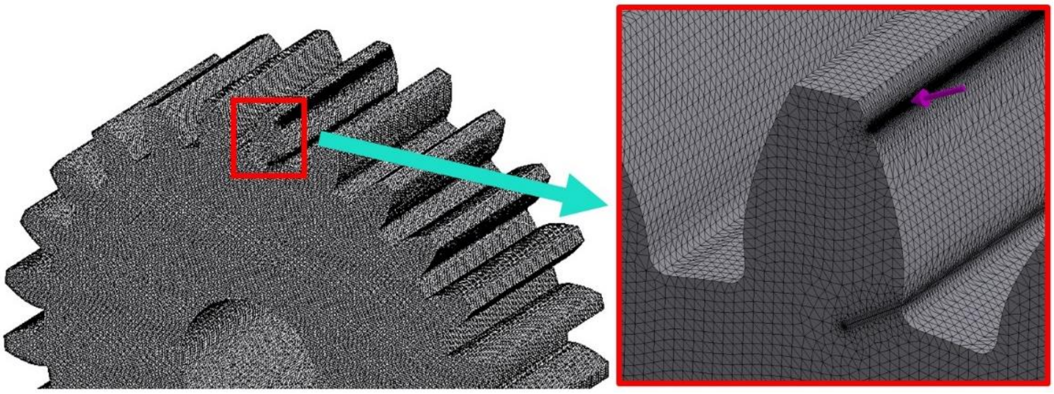

Figure 79: Meshing using the mesh control at the force applied area and the crack region

Table 5: Simulation details

Model type	Linear Elastic Isotropic
Element Type	Parabolic Tetrahedral
Integration points	4
Maximum Element Size	0.224 mm
Minimum Element size	0.003 mm
Total Nodes	19,971,575
Total Elements	14,403,857
% of elements with Aspect Ratio < 3	99.9

4.2.1 Finite Element Analysis Results

For each angular position, the force is applied, and the deflection is recorded. The individual stiffness value is simply equal to the force divided by the deflection, both taken in the same direction. It is considered that the material withstands the load applied and the yield stress is not reached for all the simulated cases, to prevent any plastic deformations. As illustrated in Figure 80, the high stresses are located at the bottom of the tooth, and at the contact surface.

Figure 80: High stresses located at load location, and the root of the tooth

As the force applied to the tooth surface is decomposed into two components, Fx and Fy, along X-axis and Y-axis, respectively, the tooth deflection is recorded in these two directions for each position. The total deflection along the force is calculated by:

$$\delta_i = \sqrt{X_i^2 + Y_i^2} \qquad \text{Eq. 88}$$

Thus, the tooth stiffness at each angular position can be obtained from Eq. 89:

$$K_i = \frac{F}{\delta_i} \qquad \text{Eq. 89}$$

For healthy and cracked pinion, the tooth stiffness is plotted against the angle of the force location (Figure 81), where both variables were transformed into dimensionless forms as:

- Stiffness Ratio (SR), $[K_{\mathrm{i}}/K_{\mathrm{max}}]$, where k_{i} is the stiffness at position *i* and k_{max} is the maximum stiffness at the start of the involute curve,
- Angle ratio (AR), $[\theta_i/\theta_{max}]$, where θ_i is the angle at position *i* and θ_{max} is the total angle of the tooth profile (end of the involute curve).

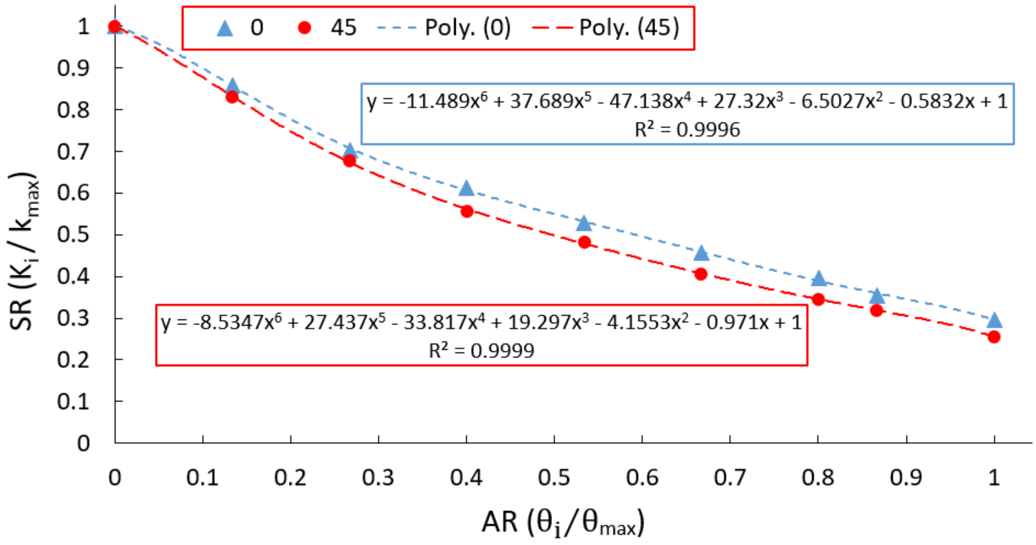

Figure 81: Stiffness ratio (SR) vs. angle ratio (AR) for 0 and 45 CLP for the pinion

It is clear that as the angle between the contact point and the bottom point, at the start of the involute curve, increases the stiffness decreases. That is because the perpendicular distance between the base of the tooth and the point at which the force is applied increases. The data points for each case were fitted using a six-degree polynomial curve that approximates the relation between the SR and the AR (Figure 81). The maximum stiffness at the start of the involute curve for different CLP are shown in Figure 82, where the maximum stiffness decreases as the CLP increases. Furthermore, only the polynomial curve for a healthy gear was obtained as it was stated earlier that cracks on the gear will not be studied.

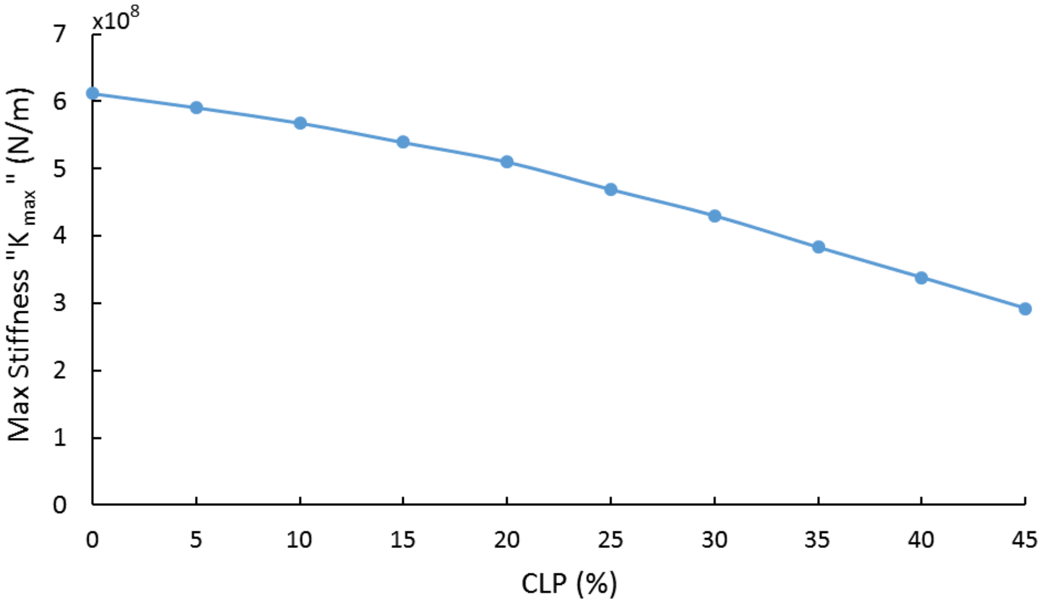

Figure 82: Max stiffness of the pinion for different CLP

4.2.2 Equivalent Stiffness for Single and Double Contacts

The polynomial equations obtained were inserted into the MATLAB code so that the stiffness at each contact point can be calculated, during the meshing between two mating gears, the contact could be single (between two teeth) or double (between four teeth). In the case of single contact, the equivalent stiffness can be calculated as shown in Figure 83, while in the case of the double contact, the equivalent stiffness is given by (Figure 84). In both cases, the influence of the Hertzian contact stiffness is added as discussed in section 2.4.1.

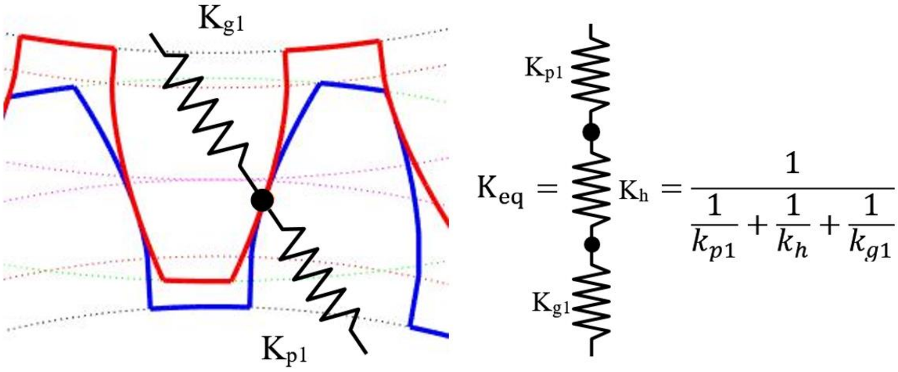

Figure 83: Single contact as two springs connected in series

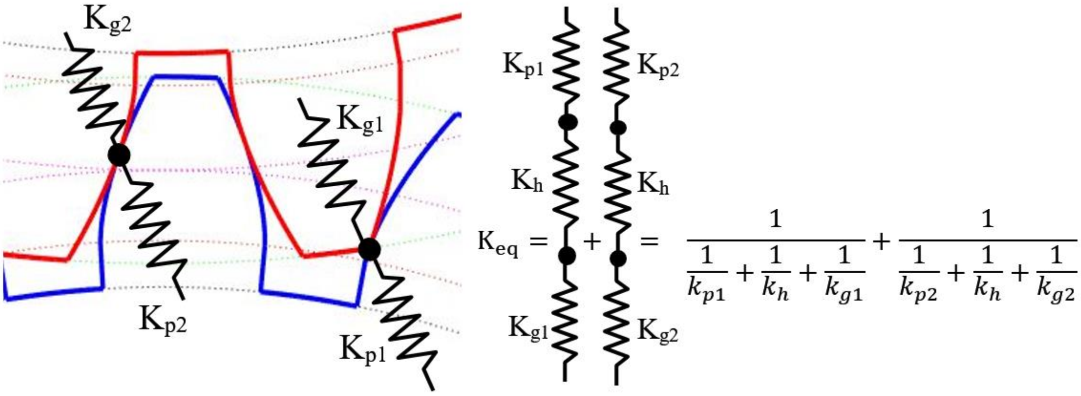

Figure 84: Double contact as two parallel sets of springs connected in series

The individual stiffness for a healthy pinion and gear were plotted against the rotation angle as shown in Figure 85, while the stiffness for the first and the second contact location are presented in Figure 86, and the overall equivalent gear mesh stiffness can be seen in Figure 87.

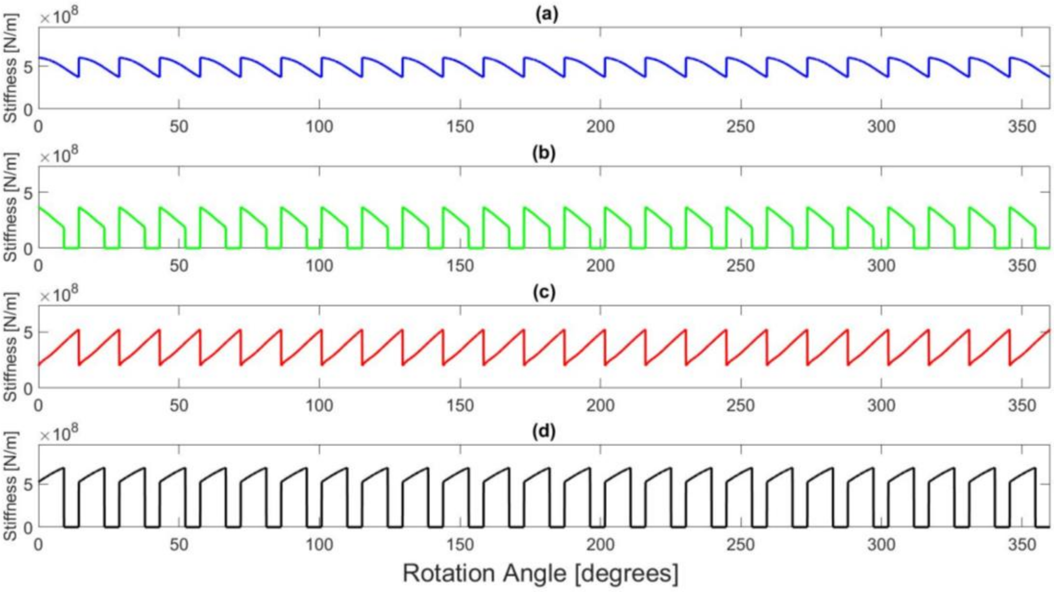

Figure 85: Individual stiffness: (a) at the 1st contact location of the pinion; (b) at the 2nd contact location of the pinion; (c) at the 1st contact location of the gear; (d) at the 2nd contact location of the gear

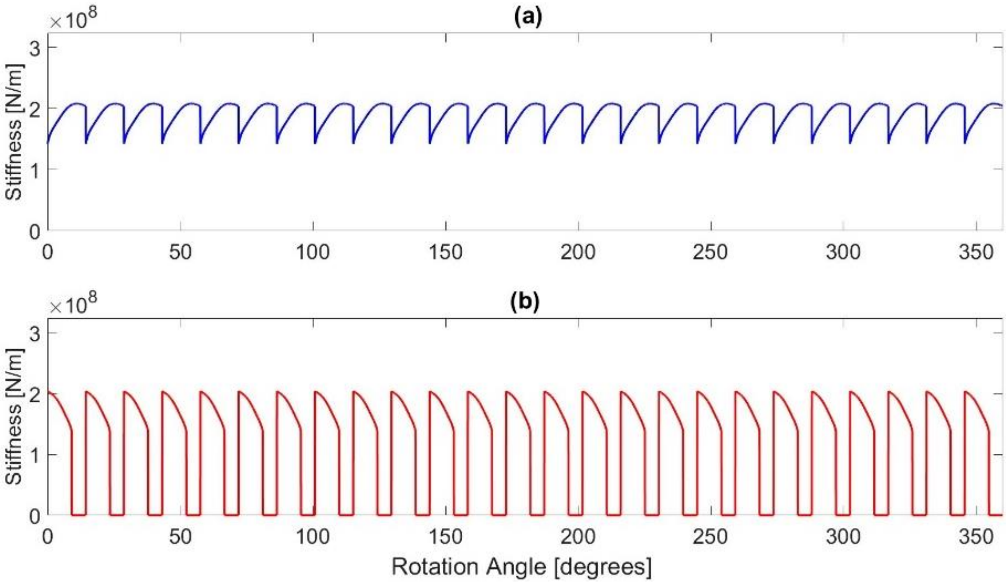

Figure 86: Single tooth mesh stiffness: (a) at the 1st contact location; (b) at the 2nd contact location

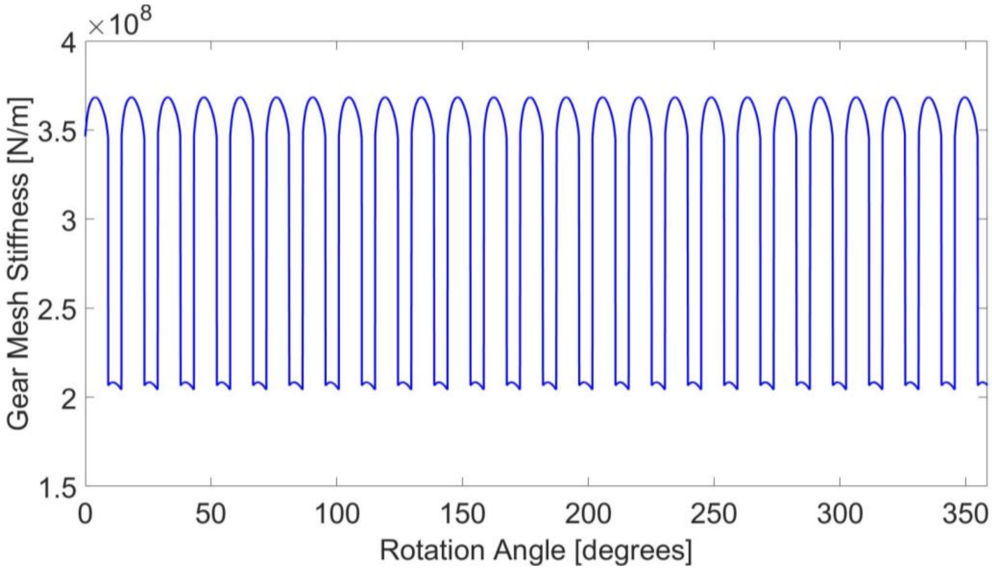

Figure 87: Gear mesh stiffness for a healthy pinion

The stiffness of a healthy and that of a cracked pinion with a crack length of 0.66 mm equivalent to 17.37% (Crack No.2), were compared with those obtained from [30] to verify the results achieved from the code developed, see Figure 88.

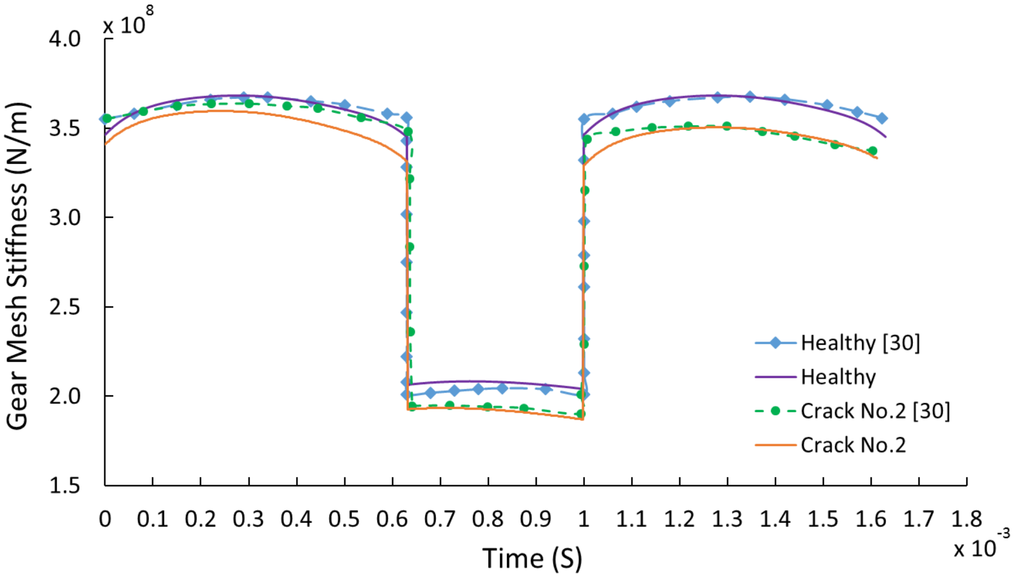

Figure 88: Comparison of the mesh stiffness for a healthy and a cracked pinion with [30]

The comparison shows that there is a good agreement between the results obtained and other published work, and that verifies the approach and the code developed. As a sample of the results obtained, Figure 89 and 90 show other CLPs, where it is clear that as the CLP increases the gear mesh stiffness decreases.

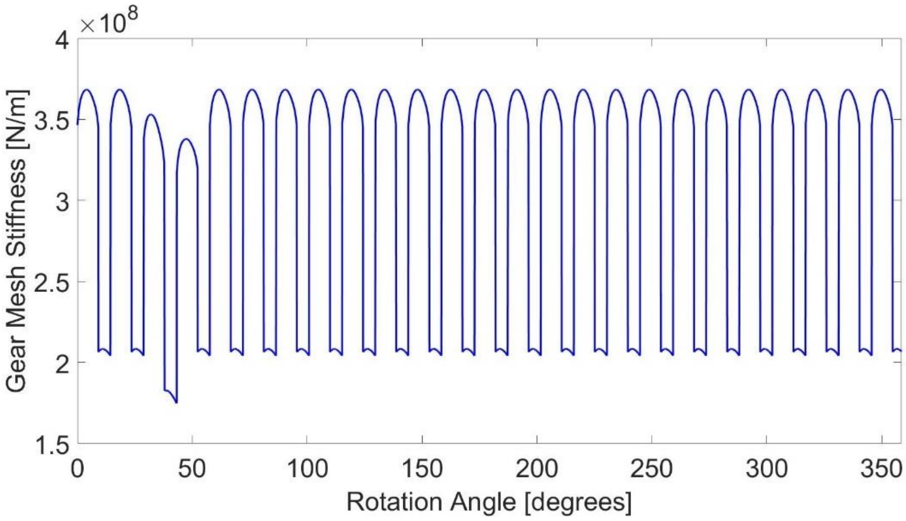

Figure 89: Gear mesh stiffness for a faulty pinion with 25% CLP

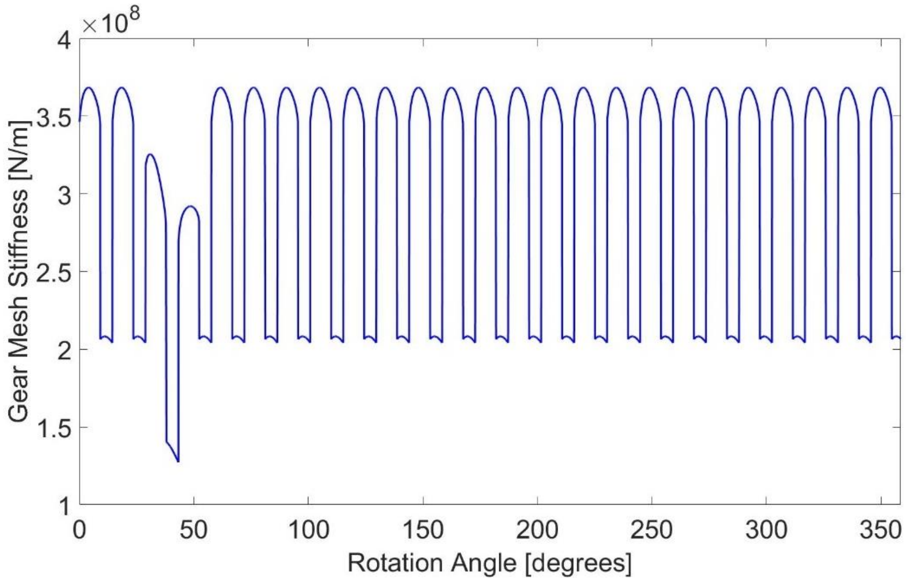

Figure 90: Gear mesh stiffness for a faulty pinion with 45% CLP

4.3 Proposed Multiple Cracks Scenarios

In a practical case, it is very improbable that a single crack would reach 40% or more of the tooth width while being the only crack in the entire set of teeth. Usually, when a crack infects one tooth, other cracks are expected to take place on the other teeth. These cracks can appear randomly on other teeth, allowing for the possibility of having consecutive and nonconsecutive cracks, as shown in Figure 91.

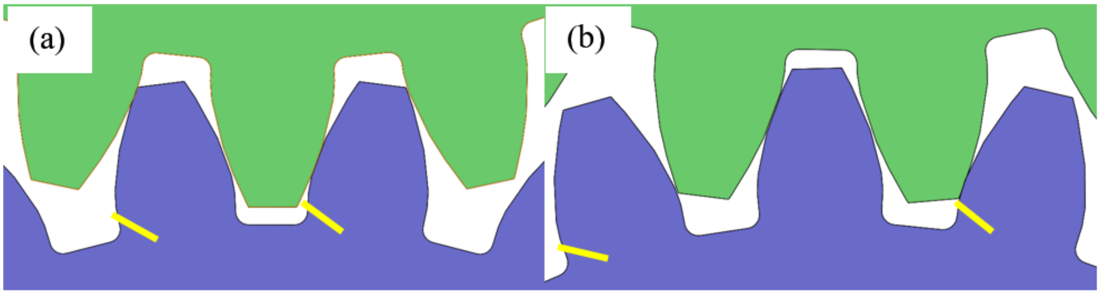

Figure 91: (a) Consecutive cracks; (b) Nonconsecutive cracks

Different multiple simultaneous cracks scenarios can be investigated, out of which the following four scenarios were considered:

1) First scenario: multiple simultaneous cracks with the same length (CLP of 30%) at nonconsecutive teeth (Figure 92).
2) Second scenario: multiple simultaneous cracks with the same length (CLP of 30%) at consecutive teeth (Figure 93).
3) Third scenario: multiple simultaneous cracks with different lengths at nonconsecutive teeth (Figure 94).
4) Fourth scenario: multiple simultaneous cracks with different lengths at consecutive teeth (Figure 95).

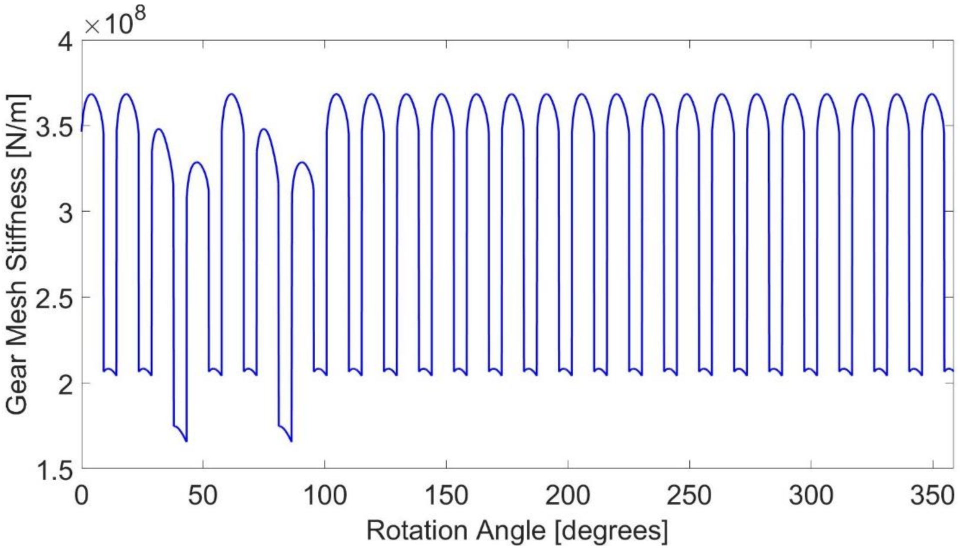

Figure 92: The gear mesh stiffness for the 1st scenario (Two nonconsecutive cracked teeth with 30% CLP)

When cracks appear on consecutive teeth, the gear mesh stiffness for the single contact case is the same as that for the nonconsecutive cracks. However, for the double contact case, the gear mesh stiffness decreases even further (Figure 93).

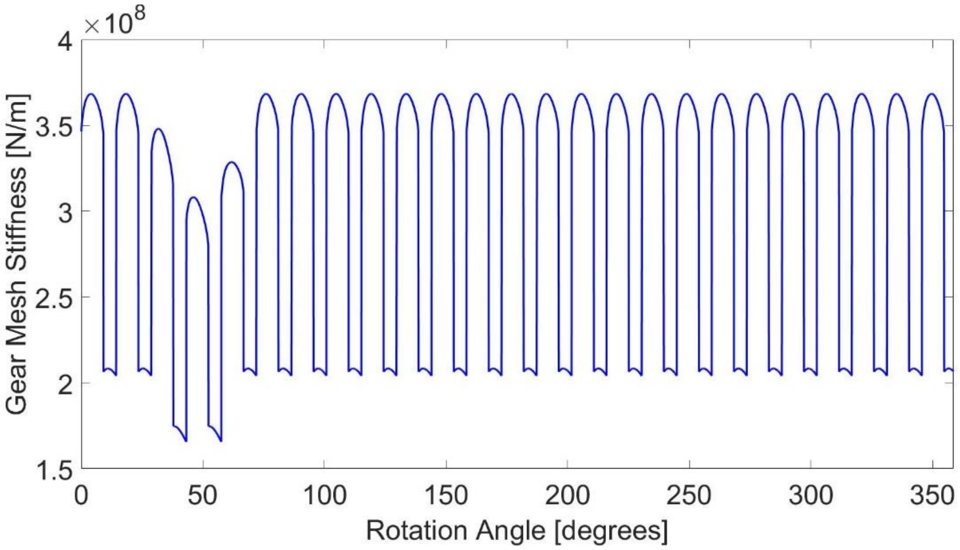

Figure 93: The gear mesh stiffness for the 2nd scenario (Two consecutive cracked teeth with 30% CLP)

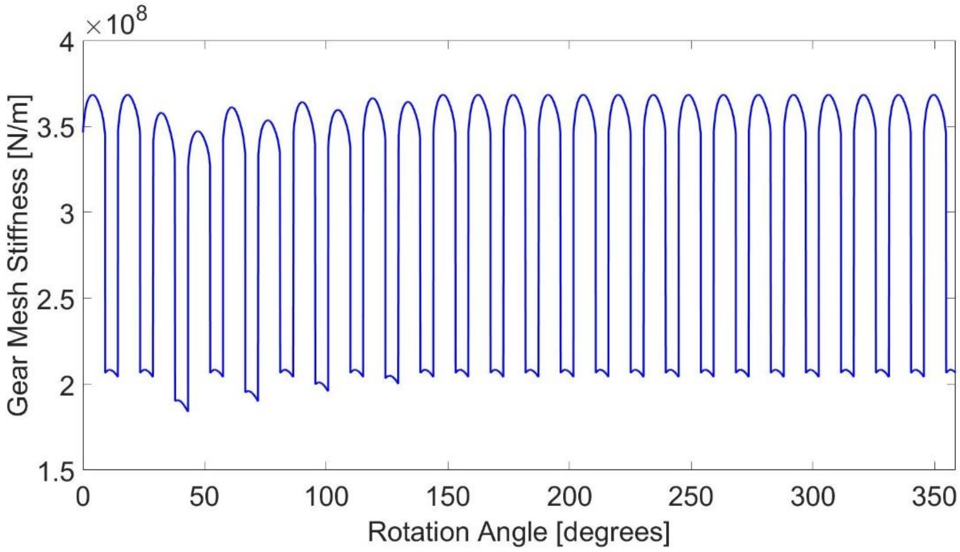

Figure 94: The gear mesh stiffness for the 3rd scenario (Four nonconsecutive cracked teeth with CLP of 20%, 15%, 10%, and 5%, respectively)

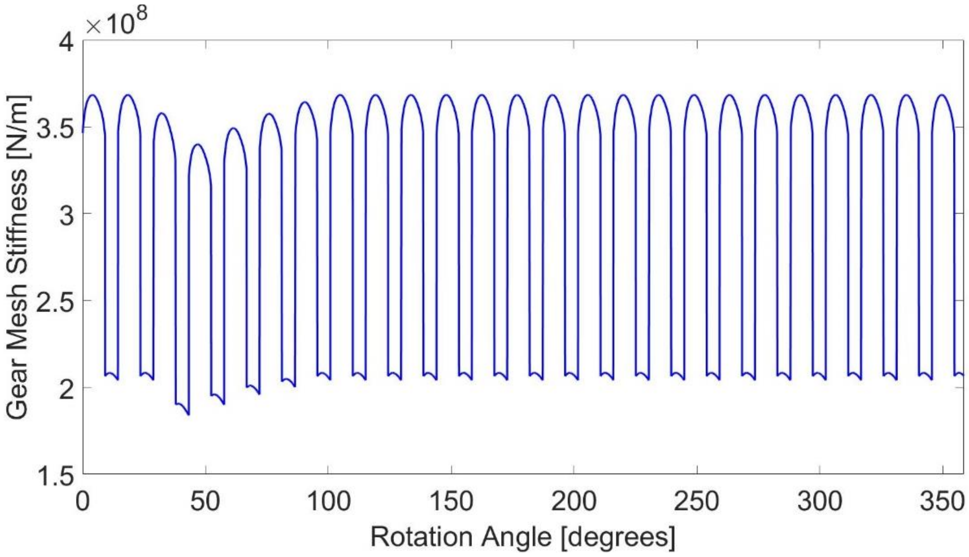

Figure 95: The gear mesh stiffness for the 4th scenario (Four consecutive cracked teeth with CLP of 20%, 15%, 10%, and 5%, respectively)

It is obvious that the mesh stiffness for the fourth scenario (Figure 95) is lower than that of the third scenario (Figure 94).

Chapter 5. DYNAMIC SIMULATION OF SYSTEM RESPONSE OF GEARBOX

In this chapter, a one-stage six DOF gear dynamic model considering the time-varying mesh stiffness, and the lateral and torsional vibrations will be simulated to study the dynamic response of the system.

5.1 Gearbox Dynamic Modeling

A six DOF model was considered in this work as it is more sensitive to teeth cracks than an eight or a twelve DOF model [41] and it was adopted in [32,30]. The coordinate system is chosen in this model such that one of the axes, the y-axis, is parallel to the line of action, whereas the x-axis is in the direction of the off-line-of-action (OLOA), see Figure 96. The parameters used in the dynamic model are adopted from [32] and are detailed in Table 6. The gears are supported elastically in both directions by springs (KB_{x1}, KB_{x2}, KB_{y1}, KB_{y2}) and dampers (CB_{x1}, CB_{x2}, CB_{y1}, CB_{y2}). These elements represent the flexibility introduced by the shafts and the bearings supporting the gears. The radial stiffness and damping of the bearings are considered to be the same both horizontally and vertically. The gearbox casing is supposed to be perfectly rigid. The equations of motion for the system in the ‘x’ direction are:

$$m_1\ddot{x}_1 = F_1 - KB_{x1}x_1 - CB_{x1}\dot{x}_1 \qquad \text{Eq. 90}$$

$$m_2\ddot{x}_2 = F_2 - KB_{x2}x_2 - CB_{x2}\dot{x}_2 \qquad \text{Eq. 91}$$

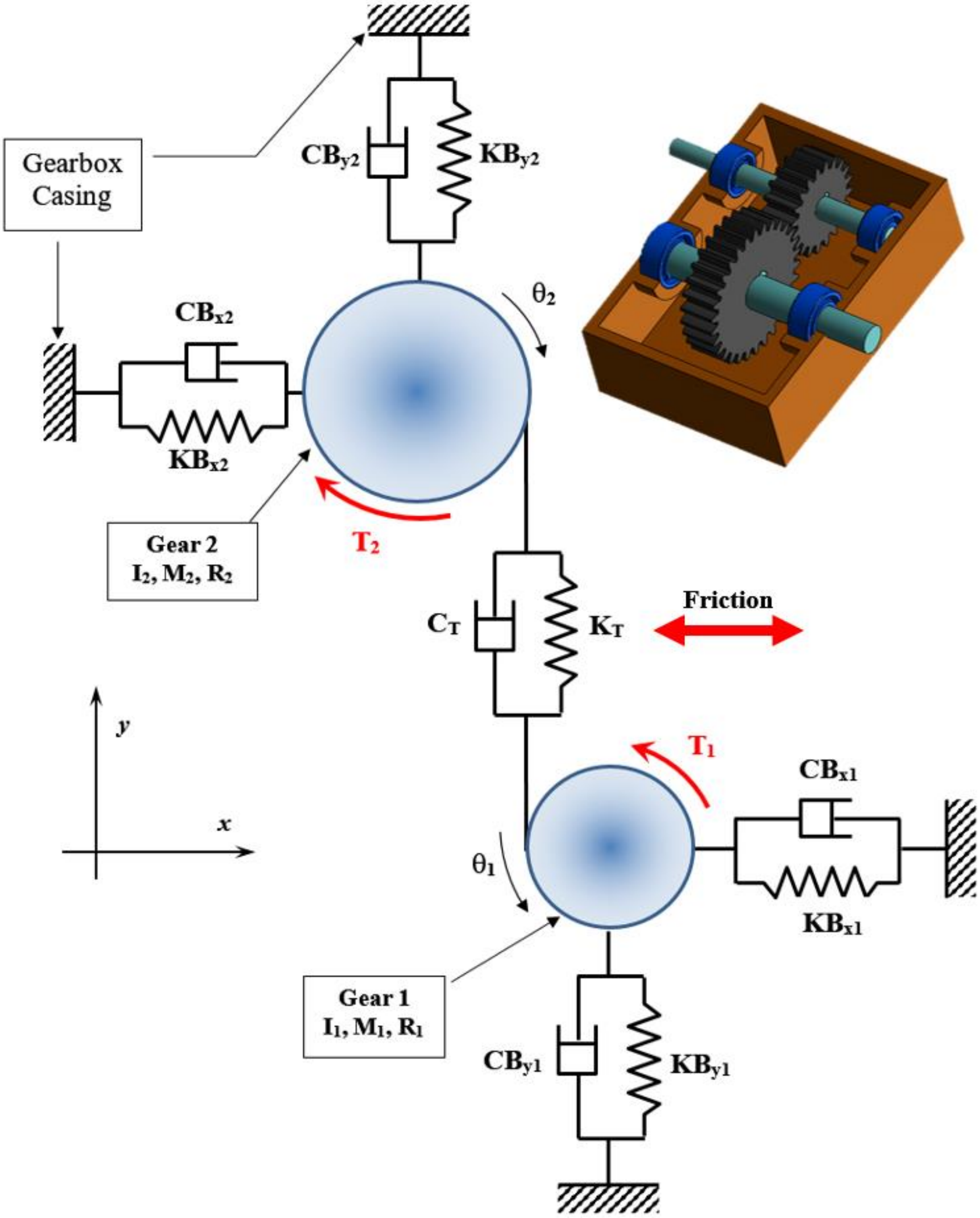

Figure 96: One-stage six DOF gearbox dynamic model

The equations of motion in the ‘y’ direction are as follows:

$$\begin{aligned} m_1\ddot{y}_1 \;=\; & -KB_{y1}y_1 - CB_{y1}\dot{y}_1 \\ & + K_T(R_{b1}\theta_1 - R_{b2}\theta_2 - y_1 + y_2) \\ & + C_T\left(R_{b1}\dot{\theta}_1 - R_{b2}\dot{\theta}_2 - \dot{y}_1 + \dot{y}_2\right) \end{aligned} \qquad \text{Eq. 92}$$

$$
\begin{aligned}
m_2\ddot{y}_2 \; = \; & -KB_{y2}y_2 - \; CB_{y2}\dot{y}_2 \\
& + K_T(R_{b1}\theta_1 - \; R_{b2}\theta_2 - \; y_1 + \; y_2) \\
& + C_T\big(R_{b1}\dot{\theta}_1 - \; R_{b2}\dot{\theta}_2 - \; \dot{y}_1 + \; \dot{y}_2\big)
\end{aligned} \qquad \text{Eq. 93}
$$

Table 6: Parameters of the gear system used in the dynamic model [32]

Parameter	**Pinion**	**Gear**
Base radius of the pinion and gear (mm)	23.49	28.20
Mass of the pinion and gear (kg)	0.3083	0.4439
Mass moment of inertia of pinion and gear (kg·m^2)	9.633×10^{-5}	1.998×10^{-4}
Applied torque (N·m)	50	60
Input shaft frequency (Hz)	40	
Mesh frequency (Hz)	1000	
Coefficient of friction	0.06	
Radial stiffness of the bearings (N/m)	6.56×10^8	
Damping coefficient of the bearings (N·s/m)	1.8×10^3	
Total damping between meshing teeth (N·s/m)	67	

For the rotary motions of the pinion and the gear, the motion equations in the ‘θ’ direction are:

$$
I_1\ddot{\theta}_1 \; = M_1 + \; T_1 - \; R_{b1}\begin{bmatrix} K_T(R_{b1}\theta_1 - \; R_{b2}\theta_2 - \; y_1 + \; y_2) \\ + \; C_T\big(R_{b1}\dot{\theta}_1 - \; R_{b2}\dot{\theta}_2 - \; \dot{y}_1 + \; \dot{y}_2\big) \end{bmatrix} \qquad \text{Eq. 94}
$$

$$
I_2\ddot{\theta}_2 \; = M_2 - \; T_2 + \; R_{b2}\begin{bmatrix} K_T(R_{b1}\theta_1 - \; R_{b2}\theta_2 - \; y_1 + \; y_2) \\ + \; C_T\big(R_{b1}\dot{\theta}_1 - \; R_{b2}\dot{\theta}_2 - \; \dot{y}_1 + \; \dot{y}_2\big) \end{bmatrix} \qquad \text{Eq. 95}
$$

where,

m_1	Mass of the pinion
m_2	Mass of the gear
I_1	Mass moment of inertia of the pinion

I_2	Mass moment of inertia of the gear
R_{b1}	Base circle radius of the pinion
R_{b2}	Base circle radius of the gear
KB_{x1}	Horizontal radial stiffness of the input bearing
KB_{x2}	Horizontal radial stiffness of the output bearing
KB_{y1}	Vertical radial stiffness of the input bearing
KB_{y2}	Vertical radial stiffness of the output bearing
CB_{x1}	Horizontal radial viscous damping coefficient of the input bearing
CB_{x2}	Horizontal radial viscous damping coefficient of the output bearing
CB_{y1}	Vertical radial viscous damping coefficient of the input bearing
CB_{y2}	Vertical radial viscous damping coefficient of the output bearing
F_1	Friction force applied on the pinion
F_2	Friction force applied on the gear
M_1	Friction moment applied on the pinion
M_2	Friction moment applied on the gear
T_1	Input motor torque
T_2	Output torque from load
K_T	Teeth mesh stiffness
C_T	Teeth mesh damping coefficient
X_1	Linear displacement of the pinion in the x direction
Y_1	Linear displacement of the pinion in the y direction
X_2	Linear displacement of the gear in the x direction
Y_2	Linear displacement of the gear in the y direction
θ_1	Angular displacement of the pinion
θ_2	Angular displacement of the gear

Symbols with one or two dots above them (e.g. $\dot{x}$ and $\ddot{x}$) represent velocities and accelerations, respectively.

5.2 Numerical Solution for the Vibration Response

The numerical solution of the set of equations of motion is achieved by a MATLAB code constantly interacting with the blocks-based environment "Simulink". The main idea of the solving technique is to isolate the term of higher derivative (acceleration) in the differential equation and to integrate it two times. When the loop is closed, the model will converge to the exact solution after several steps of numerical calculations. Considering that the equation of motion of the system is in the form:

$$M\ddot{x} + C\dot{x} + Kx = f(t) \qquad \text{Eq. 96}$$

Also, Eq. 96, can be transformed into the following form:

$$\ddot{x} = \frac{1}{M}\left[-C\dot{x} - Kx + f(t)\right] \qquad \text{Eq. 97}$$

Then, Eq. 97 could be programmed by using the block diagram method, as follows:

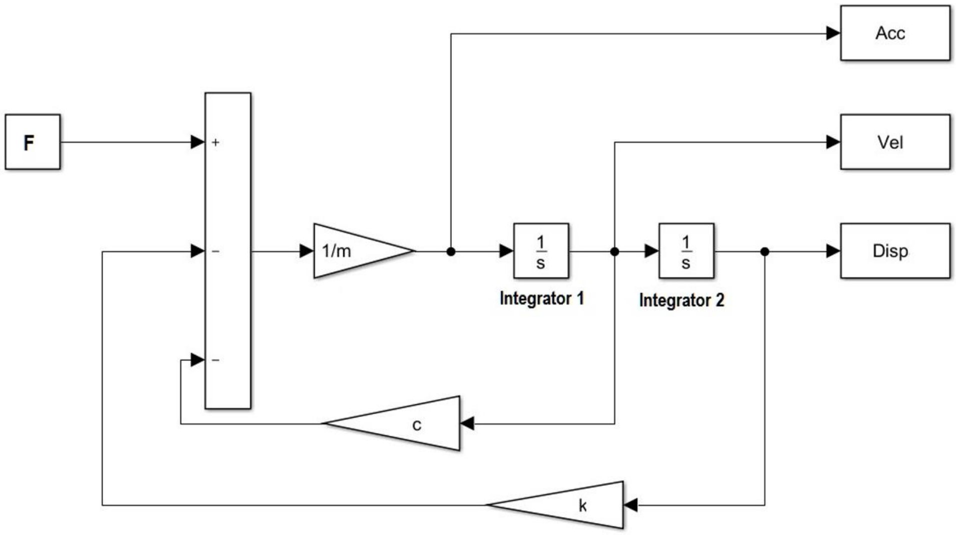

Figure 97: Block diagram in Simulink for Eq. 90

The particularity of this method is that it allows reaching a solution even if the system is non-linear. For our case, the dynamic analysis of the gearbox, with two external spur gears meshing together, is achieved by two sub-programs:

- The block-diagram has been programmed inside the first subprogram (Simulink environment)
- The command of the block-diagram and the definition of all parameters and variables are done inside the second subprogram written using a MATLAB code.

Chapter 6. VIBRATION RESPONSE IN TIME AND FREQUENCY DOMAINS

In this chapter, different statistical techniques were applied to both the time and the frequency domains, to permit the early detection of faults and to prevent any sudden teeth breakage. Also, the sensitivity of the statistical parameters to the faults growth, extracted from both time and frequency domain are investigated.

6.1 Time-domain Indices

The numerical solution of Eq. 97 was achieved by using the ODE4 function in Simulink, at first the ODE45 function, which is based on the 4th – 5th Runge-Kutta method with a variable time step [50], was used similar to [30] and it did not fail. However, to get the same signal length, a fixed time step was needed and thus the fourth-order Runge-Kutta formula (ODE4) was selected. A normally distributed noise was added with a Signal-to-noise ratio value of 20 dB to include the measurement noise influence [30]. In this study, two simulated revolutions for the pinion were considered, where the first revolution including the transient response, was excluded. The sampling frequency of 400 kHz was used to prevent aliasing and since the simulated revolutions have a total of 20,000 samples (10,000 samples/revolution) and the revolution takes 0.025 seconds. The y-displacement of the pinion was analyzed and samples of the time waveform signals for a healthy case is shown in Figure 98. Also, the same for faulty cases with 25% and 45% CLP are shown in Figure 100 and 102 respectively. The residual signal was obtained by subtracting the time-domain healthy signal from the faulty gear signal to ensure that the remaining signal is only related to the fault as shown in Figure 99, 101, and 103, respectively. Furthermore, the time-domain statistical parameters discussed in section 2.7.1 were calculated for both the original and the residual signals. A noticeable relationship between the crack length and the parameters values is clearly observed.

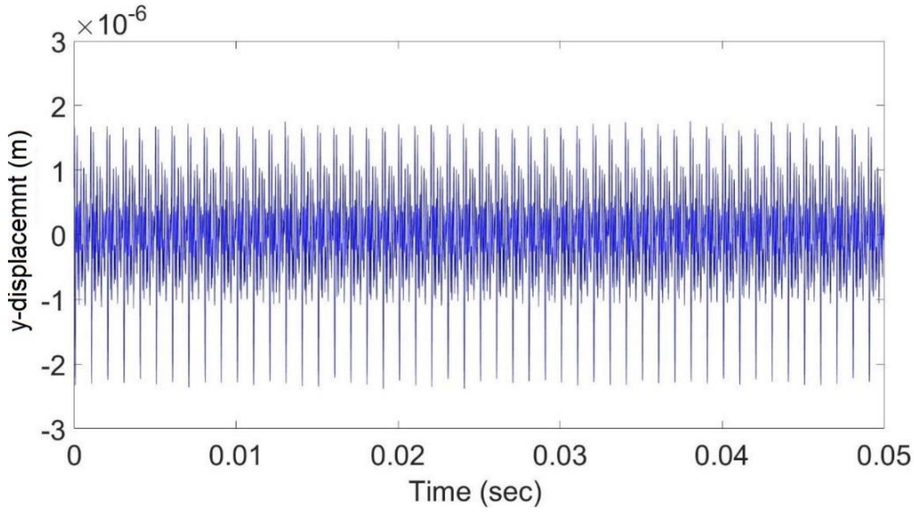

RMS = 6.68E-07, Peak = 1.73E-06, KU = 4.07, CF = 2.59,
SF = 1.32, IF = 3.42, Talaf = 1.62, Thikat = 3.67

Figure 98: Original signal of a healthy pinion; CLP = 0%

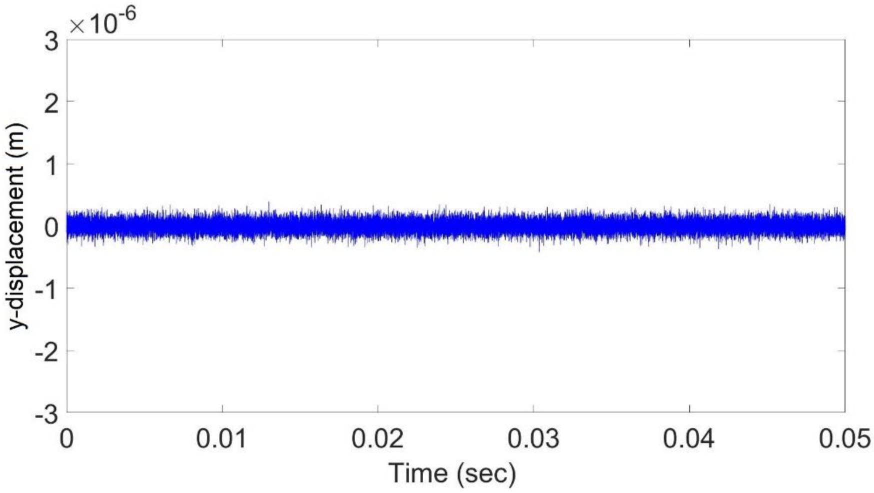

RMS = 9.26E-08, Peak = 3.63E-07, KU = 2.98, CF = 3.92
SF = 1.25, IF = 4.92, Talaf = 1.38, Thikat = 4.3

Figure 99: Residual signal of a healthy pinion; CLP = 0%

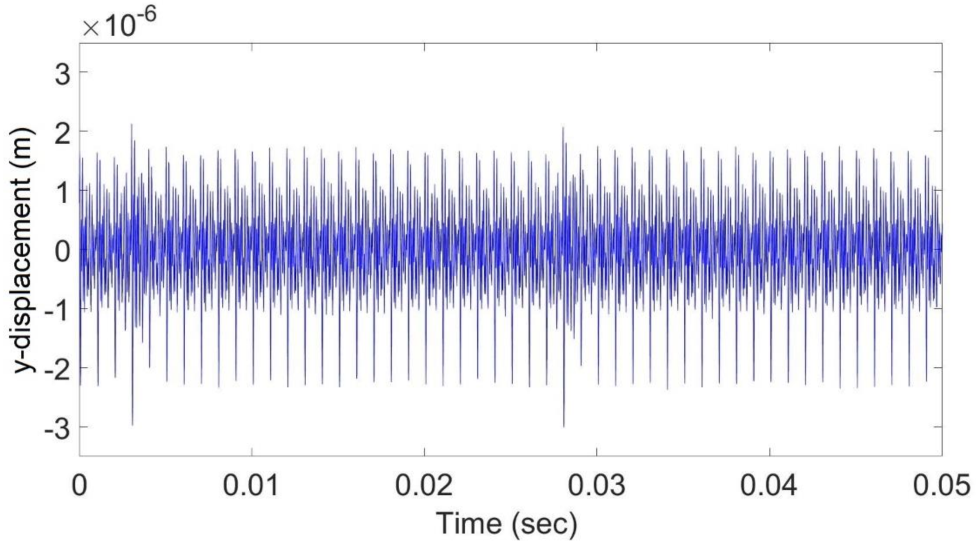

RMS = 6.78E-07, Peak = 2.13E-06, KU = 4.07, CF = 3.14
SF = 1.32, IF = 4.13, Talaf = 1.63, Thikat = 4.42

Figure 100: Original signal of a faulty pinion; CLP = 25%

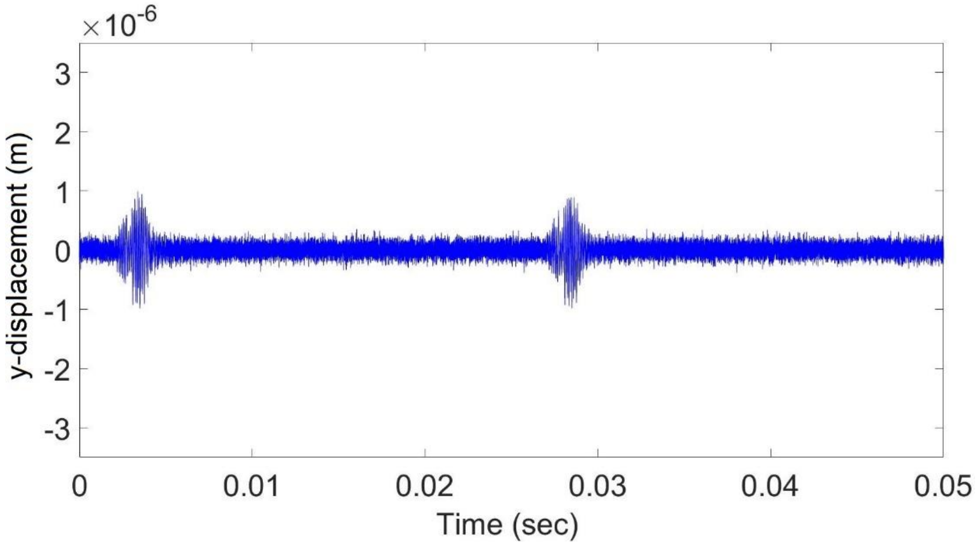

RMS = 1.36E-07, Peak = 9.90E-07, KU = 10.59, CF = 7.25
SF = 1.46, IF = 10.62, Talaf = 2.49, Thikat = 17.11

Figure 101: Residual signal of a faulty pinion; CLP = 25%

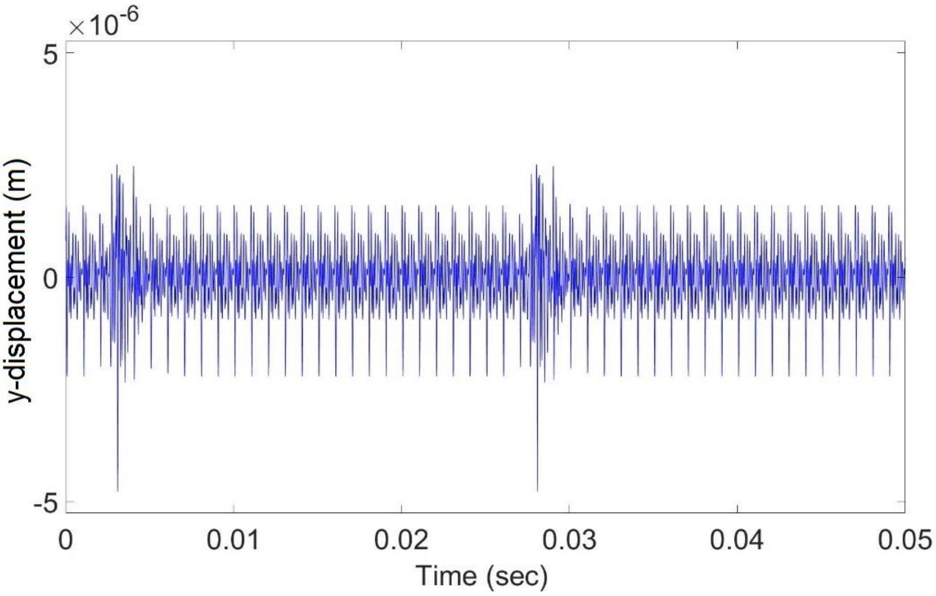

RMS = 7.21E-07, Peak = 2.57E-06, KU = 5.34, CF = 3.56
SF = 1.34, IF = 4.78, Talaf = 1.86, Thikat = 5.97

Figure 102: Original signal of a faulty pinion; CLP = 45%

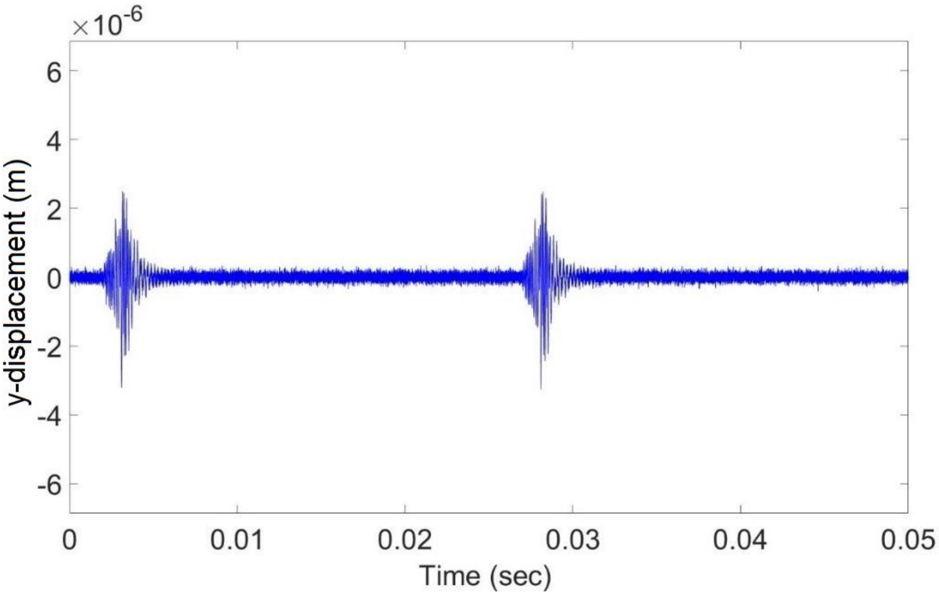

RMS = 2.82E-07, Peak = 2.49E-06, KU = 34.14, CF = 8.85
SF = 2.14, IF = 18.93, Talaf = 3.62, Thikat = 31.24

Figure 103: Residual signal of a faulty pinion; CLP = 45%

For the complete topography of the effect of the crack length on the time domain indicators applied to the original signal, the indicators' percentage change was plotted against the CLP, see Figure 104. The indicators' values for a healthy gear were considered as a reference to be used for calculating the indicators' percentage change. Initially, when the crack size is small, the resulting small shocks increase the value of the peak amplitude of the signal, as well as the value of the parameters Thikat, IF, and CF. However, they have a minor influence on the RMS, kurtosis, SF, and Talaf values. As the size of the crack increases, an increase in the levels of the indicators can be observed. The peak amplitude, Thikat, IF, and CF appear to be more sensitive than the other parameters, whereas the SF appears to be the least sensitive indicator.

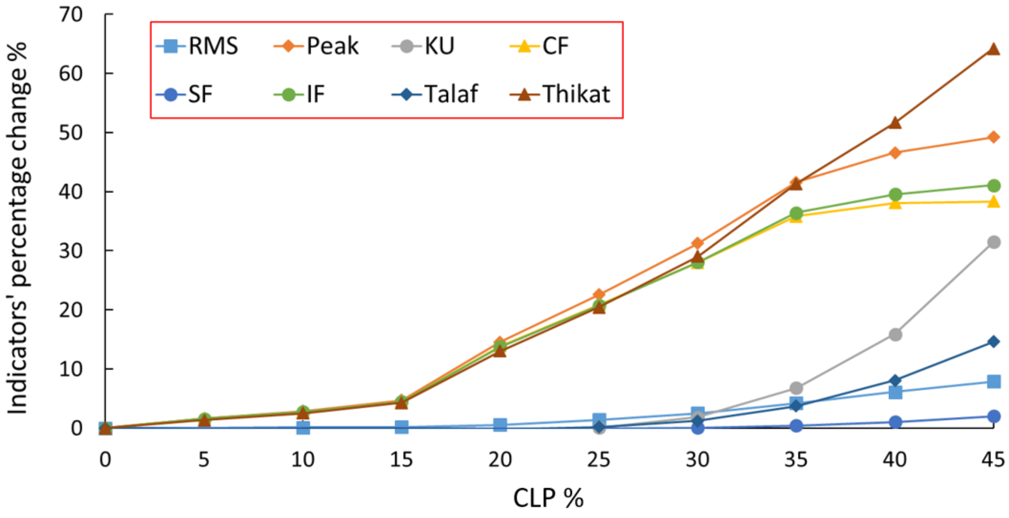

Figure 104: Performance of different time-domain indicators applied to the original signal

Since the values of most of the indicators, applied on the original signal, did not increase significantly as the CLP is increased, the indicators were applied on the residual signal. As expected, the sensitivity of the parameters to the crack length became more pronounced. The percentage change, taking the healthy case indicators values as a reference, was calculated and plotted against the CLP as it can be seen in Figure 105. It is apparent that the values of all the statistical parameters increase as the CLP increases but with different rates. For small values of cracks, the parameter Thikat has the highest sensitivity. However, when the crack exceeds 25%, Kurtosis showed a better sensitivity than the other parameters in issue.

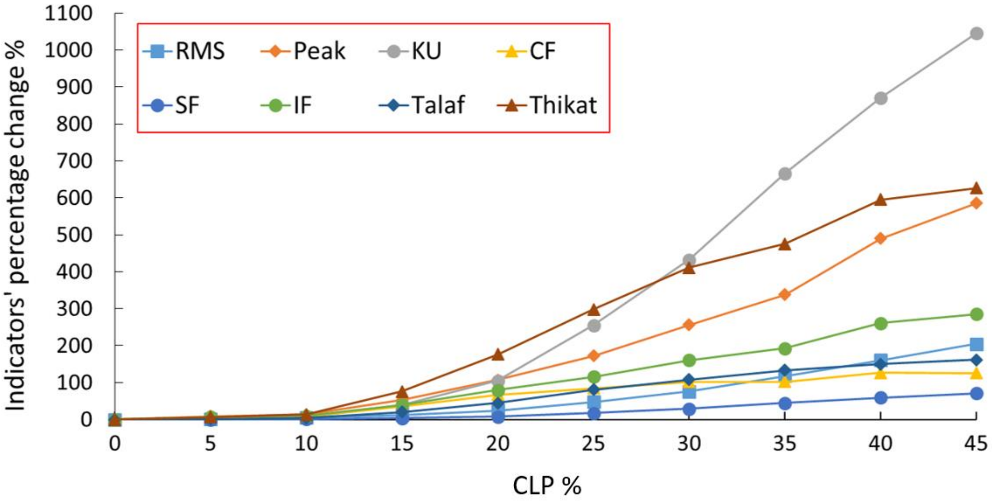

Figure 105: Performance of different time-domain indicators applied on the residual signal

These results were compared with another published work. However, the crack levels given in [37] are calculated as the crack length divided by the tooth thickness while the crack levels provided in this study are computed as the crack length divided by the entire crack path (3.8 mm). Thus, the crack levels were adjusted to be based on the total crack length. The indicators values were normalized to the healthy signal, and then the Kurtosis and crest factor values (applied on the residual signal) obtained by the code developed were compared with those presented in [37]. Figure 106 and 107 indicate that the data points values and the trend of the curves obtained are very close to those published ones.

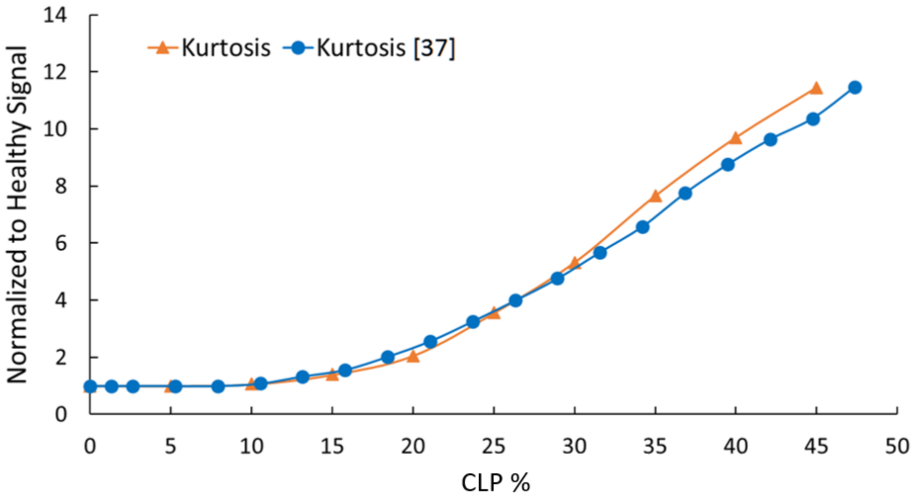

Figure 106: Comparison between the Kurtosis values normalized to the healthy value applied on the residual signal

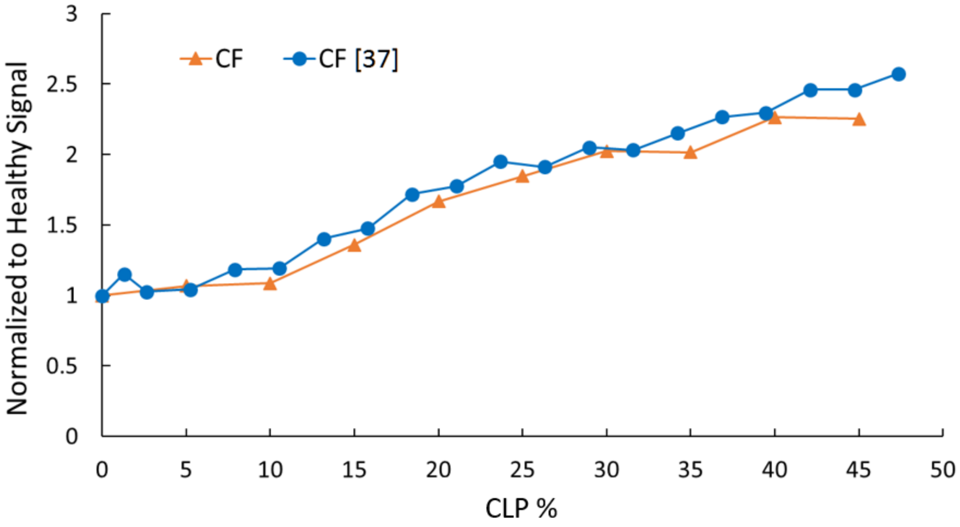

Figure 107: Comparison between the Crest Factor values normalized to the healthy value applied on the residual signal

The vibration response of the different crack scenarios proposed in Section 4.3 was obtained, and the sensitivity of the aforementioned parameters was investigated. For the first scenario, a sample of the residual waveform for two nonconsecutive cracked teeth is shown in Figure 108.

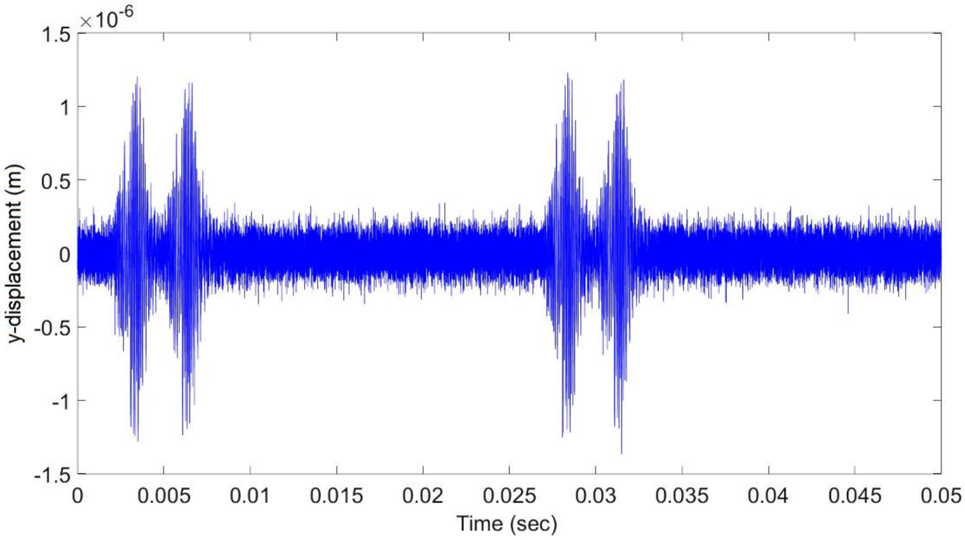

Figure 108: Residual signal obtained for the 1st scenario (Two nonconsecutive cracked teeth with 30% CLP)

Different nonconsecutive cases were considered, where the number of cracked teeth was increased from one to seven. For this scenario, the percentage change of the indicators against the number of cracks is portrayed in Figure 109. It can be seen that contrary to the previous case (single crack), the parameters are not responding in the same way as in this case (multiple cracks). At first, the values of all the parameters, as previously stated, increase due to the presence of one crack. However, as the number of cracks increases, the values of most of the parameters decrease. The values of the CF and IF will even decrease to values less than that of a healthy signal. For the SF, the values increased at the beginning, then started decreasing after two cracks. On the other hand, the value of the RMS increases significantly with the number of cracks, making it the most sensitive parameter for this scenario. The peak value remains almost constant after the first crack since the same CLP was used for all the cracks.

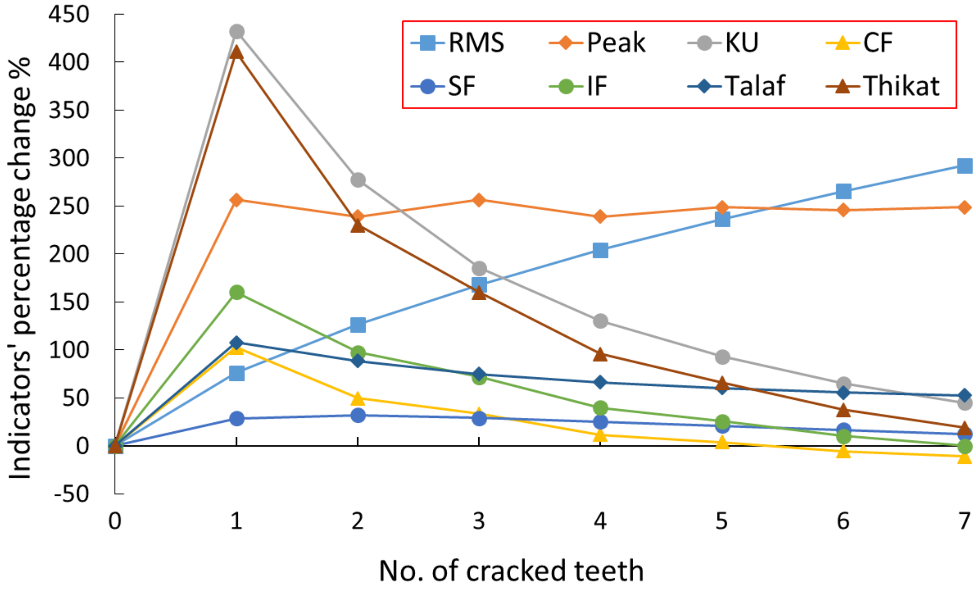

Figure 109: Performance of different time-domain indicators applied to the residual signal for the 1st scenario of multiple cracks

In the second scenario, the number of cracked teeth has been increased to seven consecutive cracks, and the values of the statistical parameters were recorded and plotted in Figure 110. All the curves gave the same trends as those of the first scenario, but the decrease in the values was with a slower rate. Moreover, the peak amplitude value became constant after three simultaneous cracks as when two cracks appear in consecutive teeth; the vibration response gives higher amplitudes (Figure 111) due to the dramatic decrease in the gear mesh stiffness.

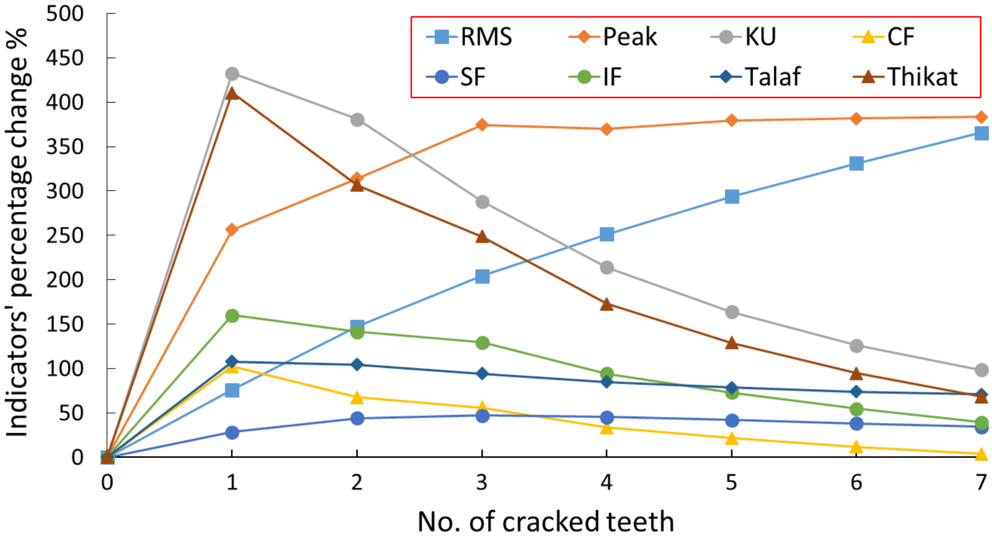

Figure 110: Performance of different time-domain indicators applied to the residual signal for the 2nd scenario of multiple cracks

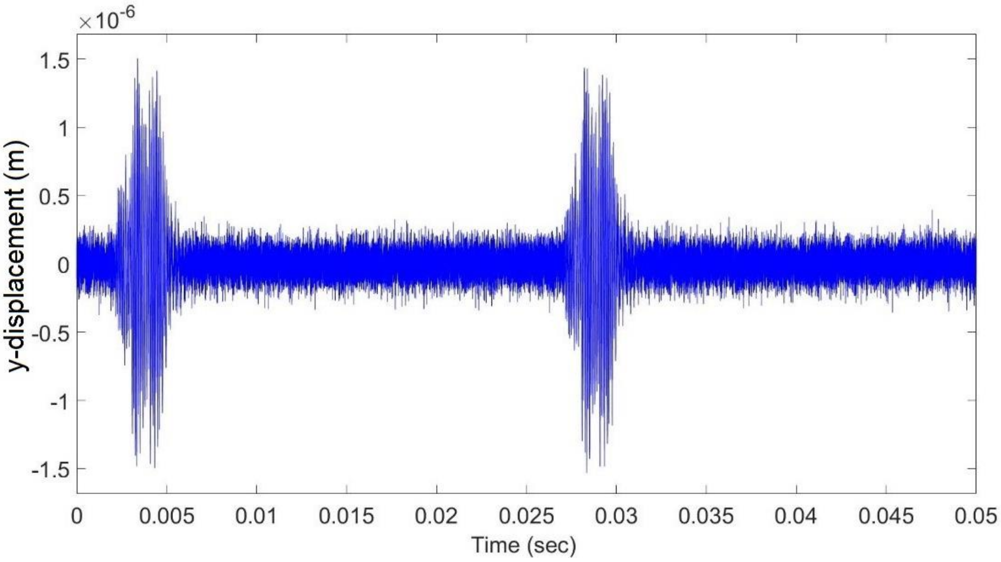

Figure 111: Residual signal obtained for the 2nd scenario (Two consecutive cracked teeth with 30% CLP)

For the third and fourth scenarios, different combinations of crack locations and lengths were considered. From one case to another, the number and the severity of the cracks were increased, where Case 0 is for a healthy pinion. Table 7 and 8 summarize the details of the simulated cases, where the only difference is the cracks being consecutive or nonconsecutive. The vibration response of the residual signal for Case 7 for both the third and fourth scenarios are shown in Figure 112 and 113, respectively.

Table 7: Cases for the third scenario with different crack locations and lengths

Case No.	**CLP at the Pinion Tooth Number (%)**									
	#1	**#3**	**#5**	**#7**	**#9**	**#11**	**#13**	**#15**	**#17**	**#19**
1	3%									
2	6%	3%								
3	9%	6%	3%							
4	12%	9%	6%	3%						
5	15%	12%	9%	6%	3%					
6	18%	15%	12%	9%	6%	3%				
7	21%	18%	15%	12%	9%	6%	3%			
8	24%	21%	18%	15%	12%	9%	6%	3%		
9	27%	24%	21%	18%	15%	12%	9%	6%	3%	
10	30%	27%	24%	21%	18%	15%	12%	9%	6%	3%

Table 8: Cases for the fourth scenario with different crack locations and lengths

Case No.	CLP at the Pinion Tooth Number (%)									
	#1	**#2**	**#3**	**#4**	**#5**	**#6**	**#7**	**#8**	**#9**	**#10**
1	3%									
2	6%	3%								
3	9%	6%	3%							
4	12%	9%	6%	3%						
5	15%	12%	9%	6%	3%					
6	18%	15%	12%	9%	6%	3%				
7	21%	18%	15%	12%	9%	6%	3%			
8	24%	21%	18%	15%	12%	9%	6%	3%		
9	27%	24%	21%	18%	15%	12%	9%	6%	3%	
10	30%	27%	24%	21%	18%	15%	12%	9%	6%	3%

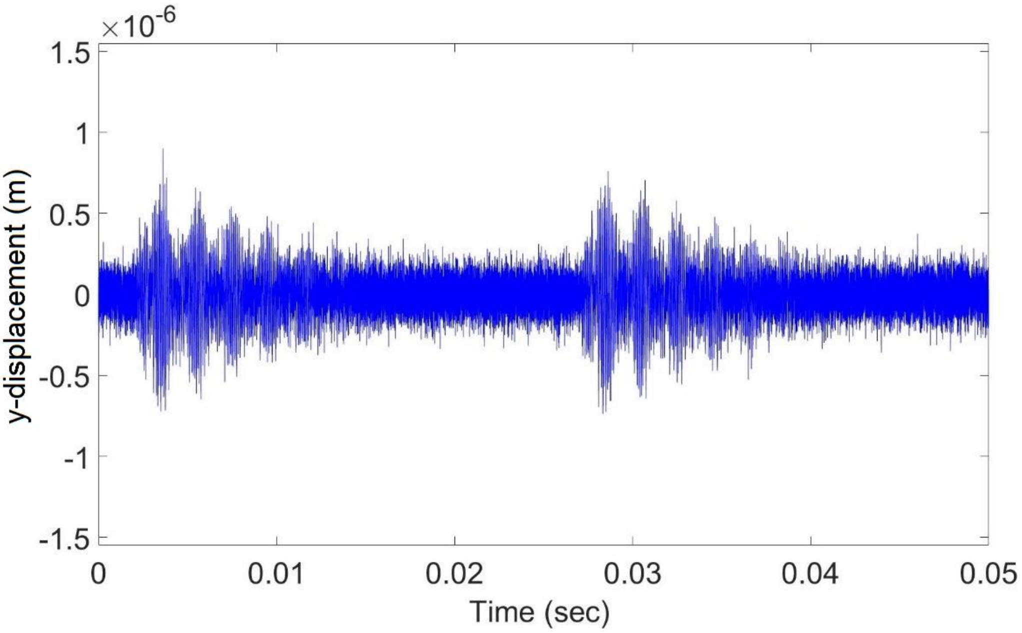

Figure 112: Residual signal obtained for the 3rd scenario (Case 7 nonconsecutive cracked teeth)

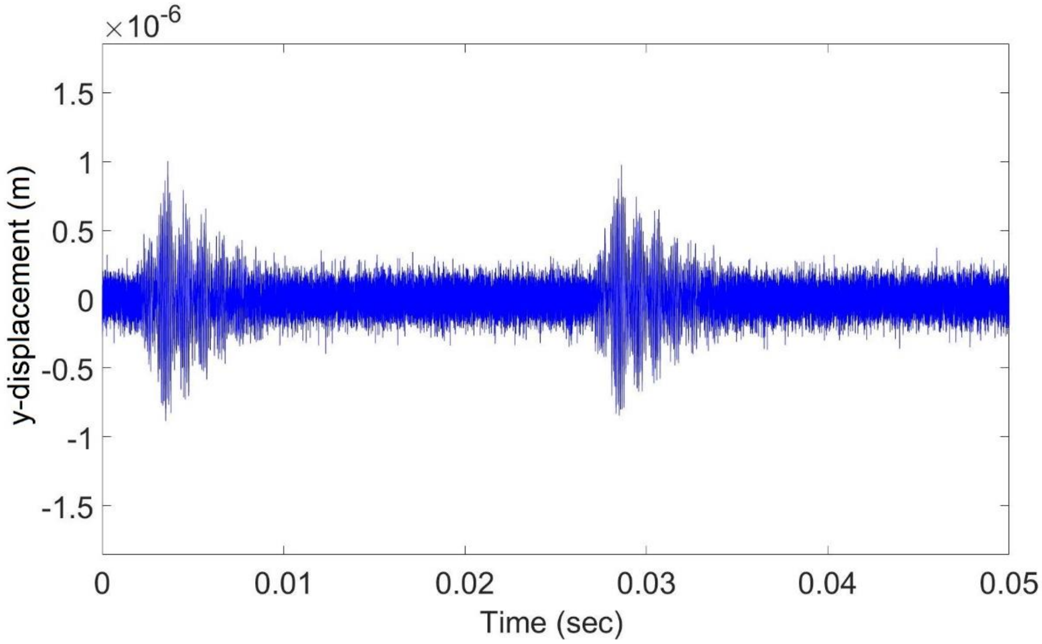

Figure 113: Residual signal obtained for the 4th scenario (Case 7 consecutive cracked teeth)

Looking at the percentage change of the statistical indicators, shown in Figure 114, for the third scenario, it is clear that the peak and Thikat have the highest sensitivity. However, after Case 8, the value of Thikat starts decreasing. Both the CF and the IF are to some extent sensitive, but their values decrease after Case 7. Also, a noticeable increase in the Talaf and RMS values after Case 5, where the RMS increases with a higher rate. The kurtosis appears to be more sensitive than the RMS but till Case 8. The SF is the least sensitive parameter to this scenario.

Figure 115 illustrates the performance of the indicator for the fourth scenario; almost the same trends are obtained. The main difference is that for the parameters Thikat, CF, and IF, their values starts decreasing earlier. In general, the sensitivity of all the parameters for this scenario is higher than the previous one. The kurtosis appears to start decreasing after Case 9, which implies that it would start decreasing as well after a few more cracks in the case of the third scenario. The SF is the least sensitive indicator and cannot be used to detect gear tooth cracks.

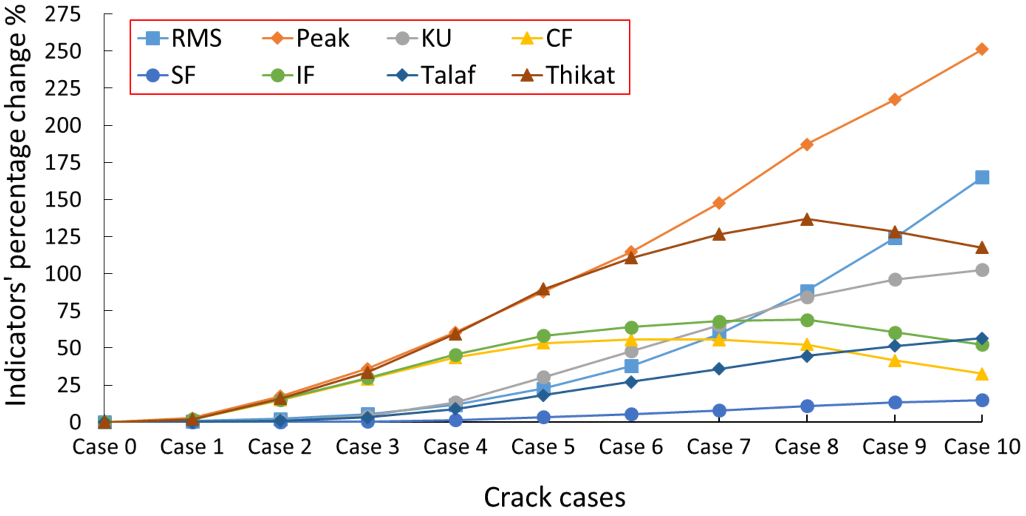

Figure 114: Performance of different time-domain indicators applied to the residual signal for the 3rd scenario of multiple cracks

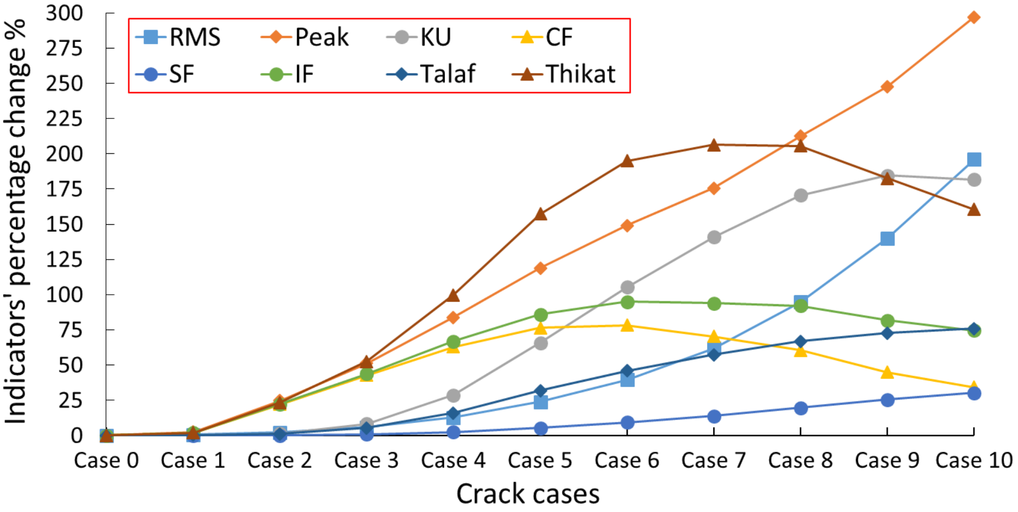

Figure 115: Performance of different time-domain indicators applied to the residual signal for the 4th scenario of multiple cracks

6.2 Frequency Domain Indices

The frequency domain analysis is known to have the potential in detecting faults in gears [29,30,52]. Other studies have found that the peak spectral amplitude is more sensitive to gear tooth cracks than the time-domain indicators [18,31].

When the gears are healthy, the sidebands generated are approximately constant in the frequency spectrum. However, similar to the time domain signal, the signal spectrum amplitude increases as the severity of the faults increases, and the number and amplitude of the sidebands increases as well [52]. Thus, the spectra of all the simulated signals and residual signals were created using two simulated revolutions for the pinion, shown previously in section 6.1.

The spectrum of the healthy case for the original and residual signals are illustrated in Figure 116 and 117, respectively, where they are in good agreement with those presented in [30]. In addition, the gear mesh frequency at 1 kHz and its multiples can be seen in Figure 116. The spectra of the original signals for a faulty tooth with 25% and 45% CLPs are shown in Figure 118 and 120, respectively, while the residual signals are shown in Figure 119 and 121, respectively.

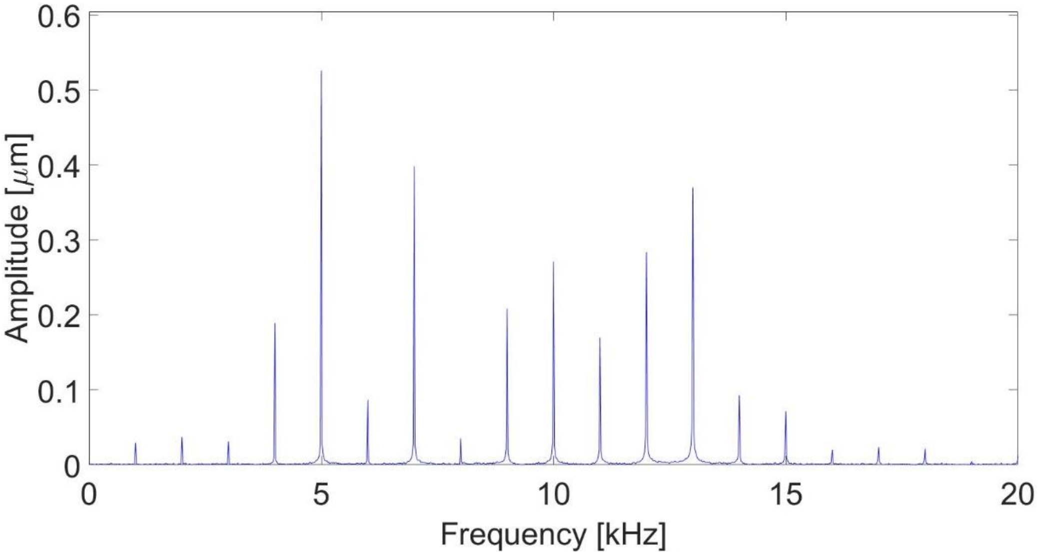

Figure 116: Spectrum of the original signal of a healthy gear

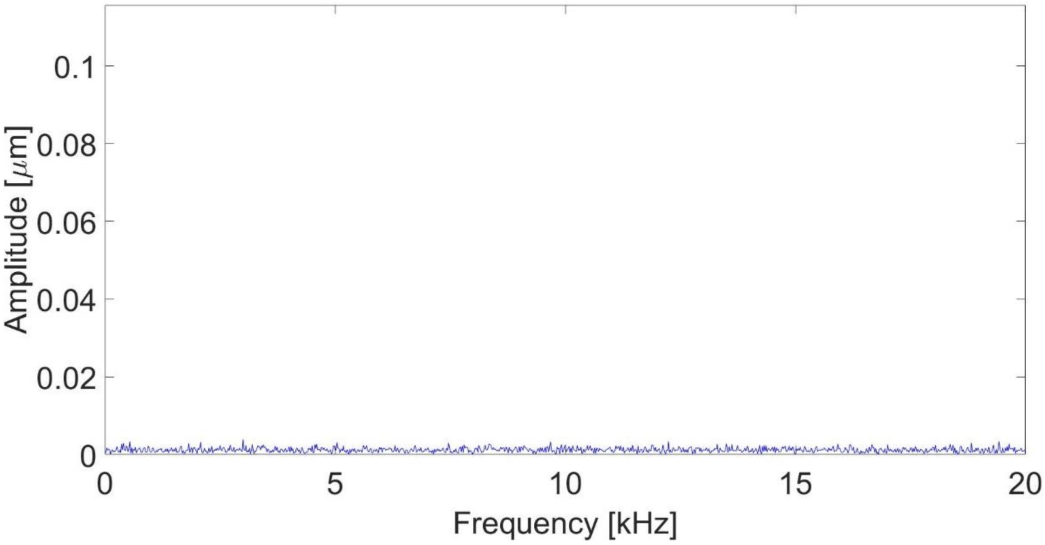

Figure 117: Spectrum of the residual signal of a healthy gear

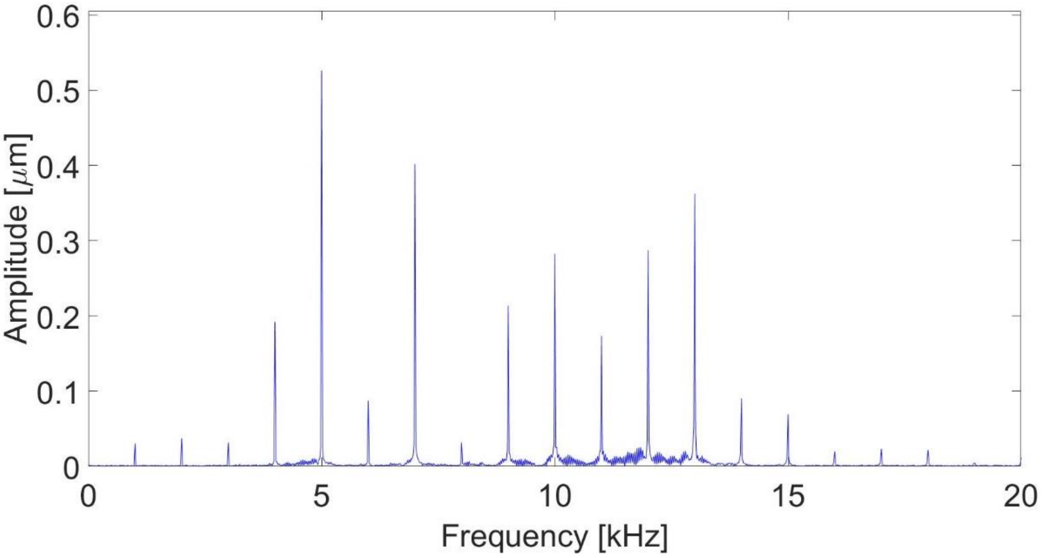

Figure 118: Spectrum of the original signal of a faulty gear (CLP = 25%)

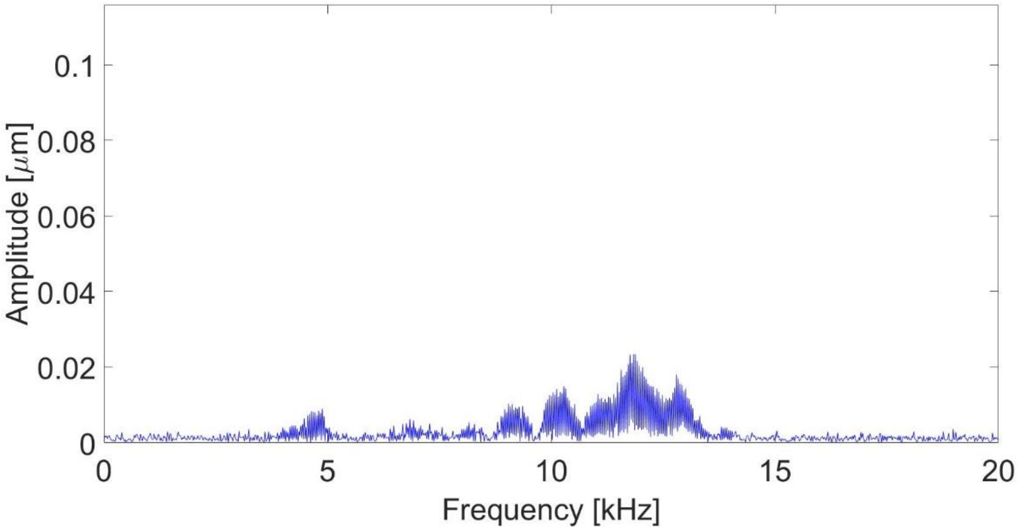

Figure 119: Spectrum of the residual signal of a faulty gear (CLP = 25%)

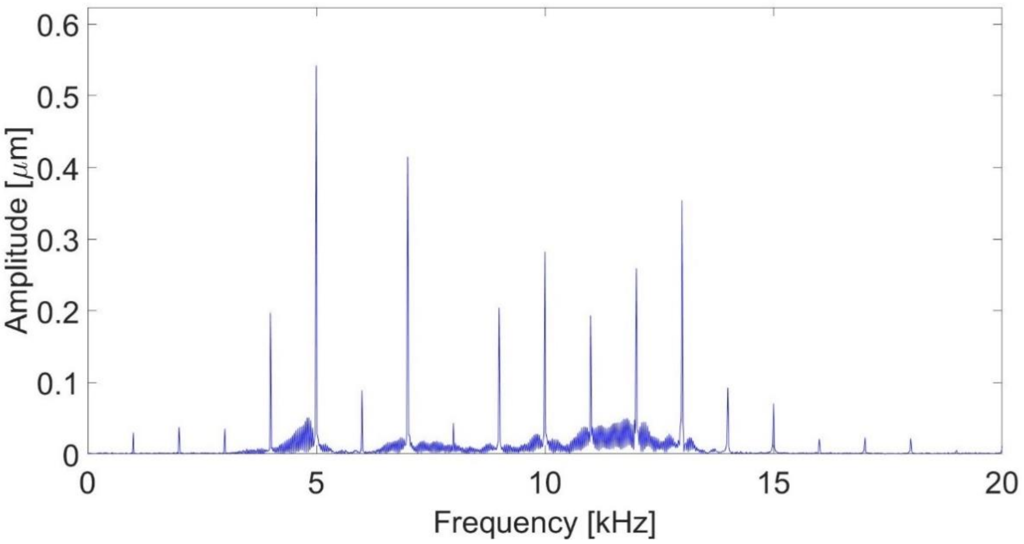

Figure 120: Spectrum of the original signal of a faulty gear (CLP = 45%)

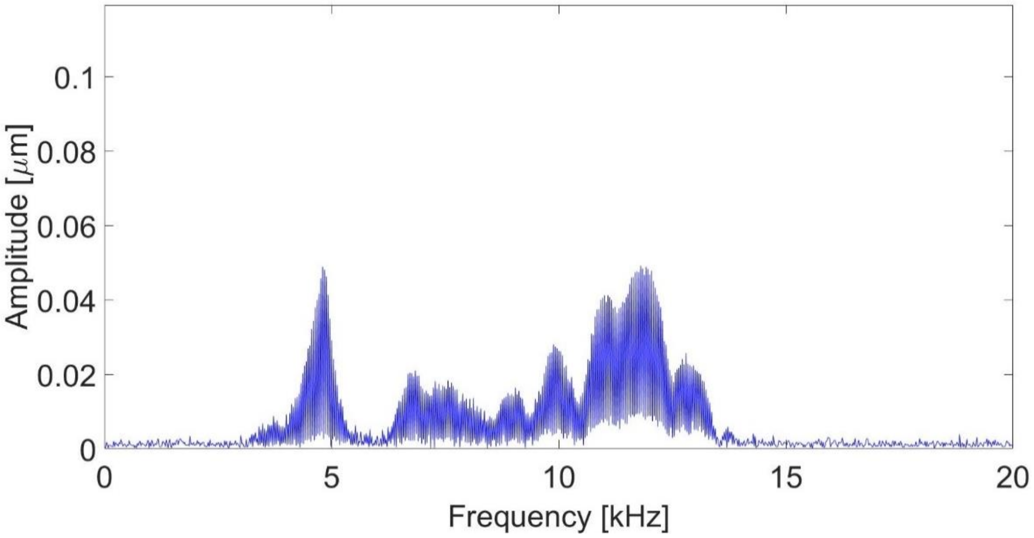

Figure 121: Spectrum of the residual signal of a faulty gear (CLP = 45%)

Since the crack was introduced in the pinion only, multiples of the rotational speed of the pinion are expected to be present in the faulty spectrum. Thus, by zooming to Figure 121, multiple integers of the pinion rotational speed (40 Hz) can be seen in Figure 122.

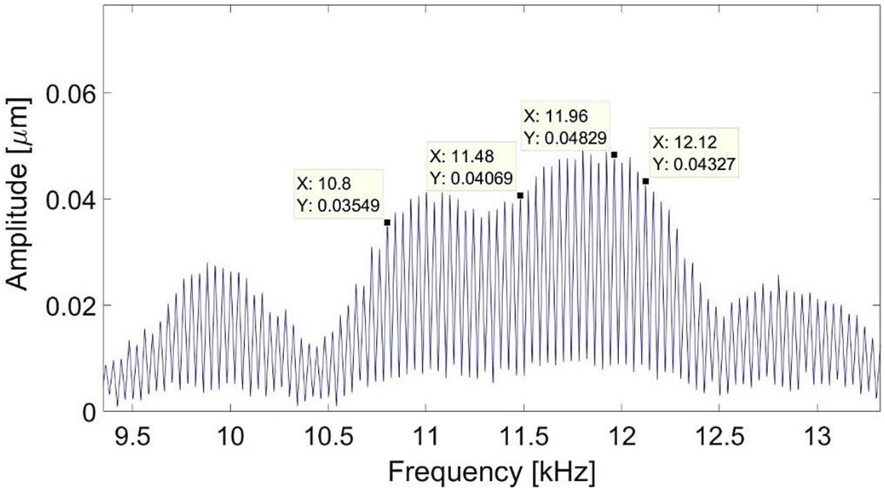

Figure 122: Zoomed area of Figure 121 showing the multiple integers of the pinion rotational speed (40 Hz)

To verify the frequency domain analysis results, the percentage change in the maximum peak of the residual signals spectra amplitude for different CLP, obtained from the code developed, was compared with that presented in [30] and it was found to be in good agreement, see Figure 123.

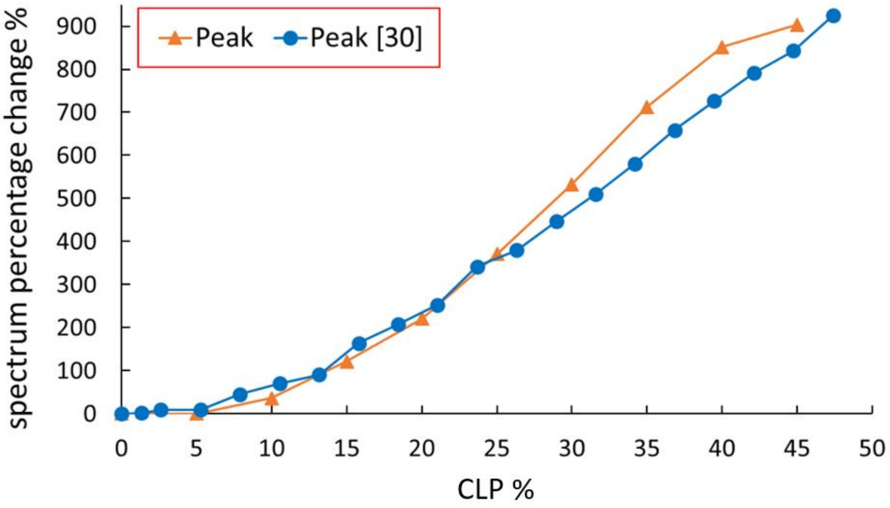

Figure 123: Comparison between the peak of the spectra of the residual signal with respect to the CLP

For the proposed multiple crack scenarios, in the spectra of the residual signal of the first scenario (Figure 124), the peaks are sharper than those of the second scenario (Figure 125) and with more sidebands. Figure 126 shows that, as the number of cracks increases, the peak amplitude of the spectra of the residual signal for both scenarios increases linearly, where the rate of the second scenario is higher as expected.

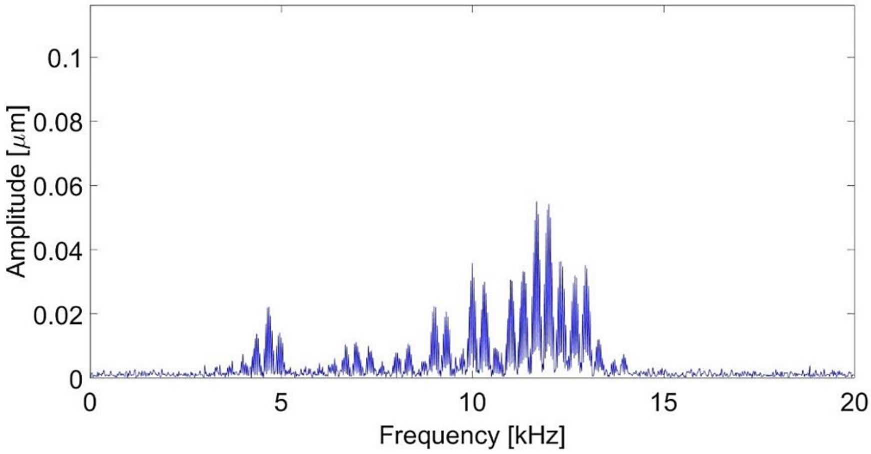

Figure 124: Spectrum of the residual signal obtained for the 1st scenario (Two nonconsecutive cracked teeth with 30% CLP)

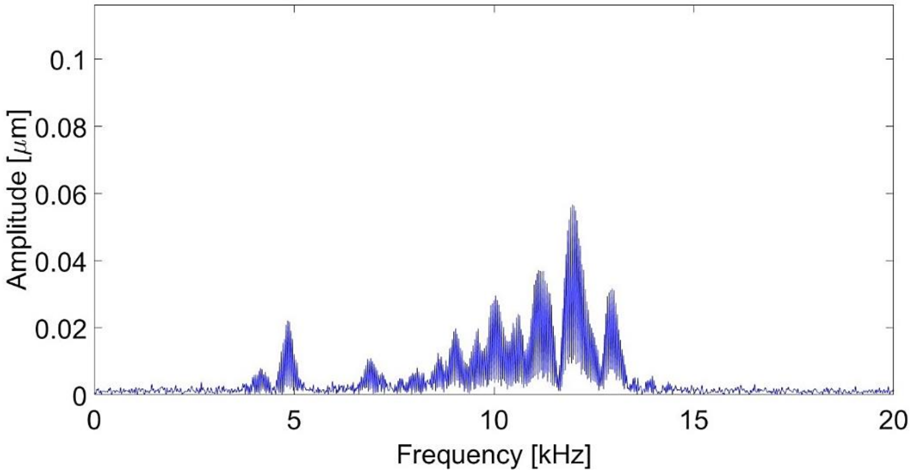

Figure 125: Spectrum of the residual signal obtained for the 2nd scenario (Two consecutive cracked teeth with 30% CLP)

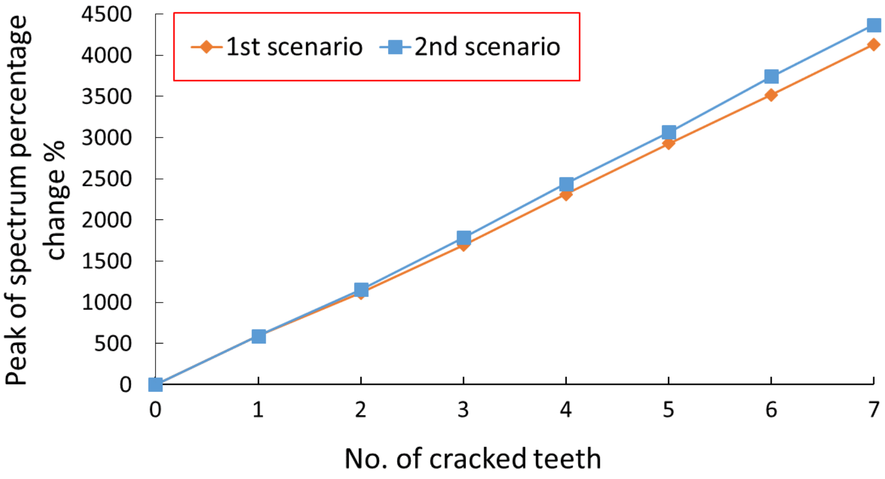

Figure 126: Percentage change in the peak of the residual signal spectrum for the 1st and 2nd scenarios

It was also observed that the number of peaks in the residual spectrum of the second scenario, between 4 kHz and 5 kHz, represents the number of consecutive cracks in the pinion. Figure 125 showed two peaks for two consecutive cracks, while as illustrated in Figure 127, seven peaks were obtained in the case of seven consecutive cracks. For other numbers of cracks, see Appendix.

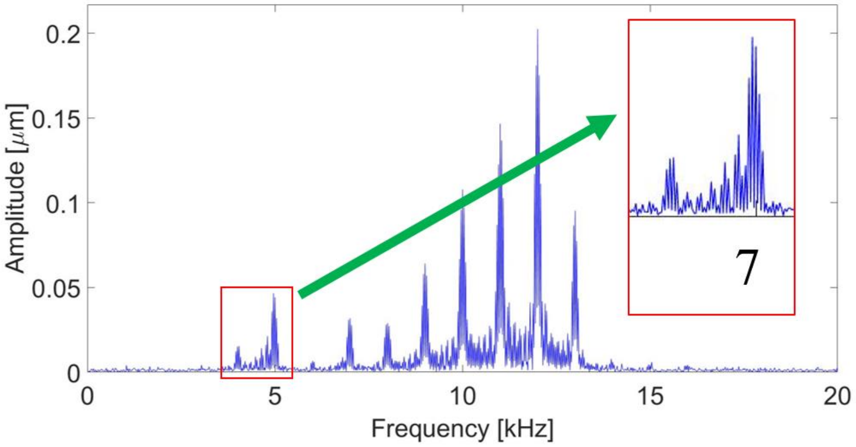

Figure 127: Spectrum of the residual signal obtained for the 2nd scenario (Seven consecutive cracked teeth with 30% CLP)

Both the number of peaks and their amplitudes for the spectra of the residual signal of the third scenario (Figure 128) are higher than that of the fourth scenario (Figure 129). As the number of cracks and their severity increases, the percentage change of the peak of the spectra increases with a third degree polynomial trend, see Figure 130.

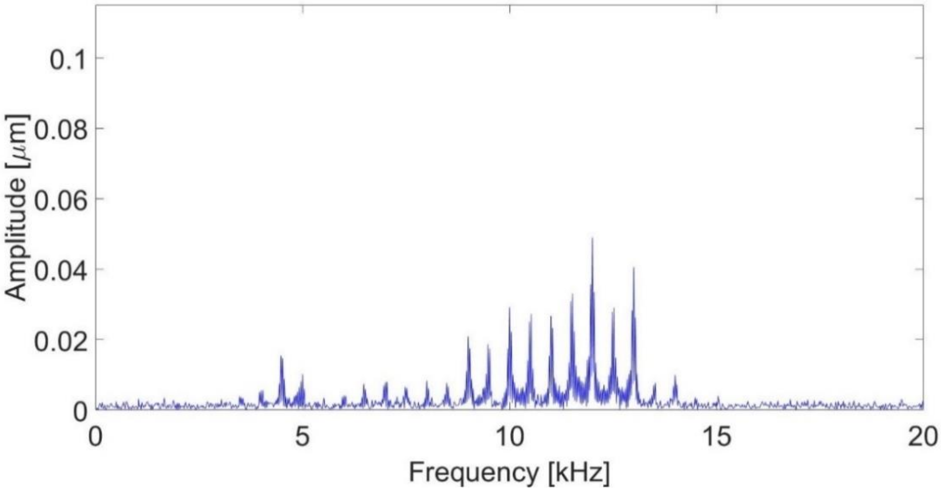

Figure 128: Spectrum of the residual signal obtained for the 3rd scenario (Case 7 nonconsecutive cracked teeth)

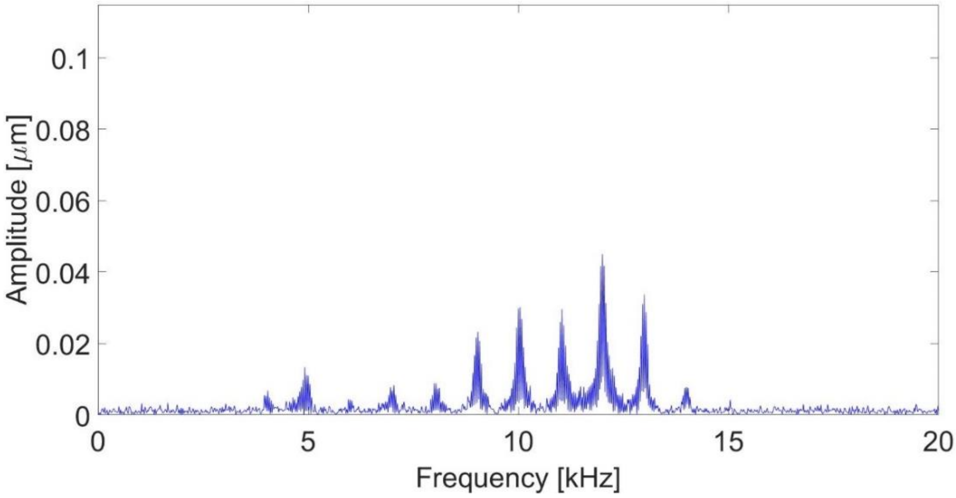

Figure 129: Spectrum of the residual signal obtained for the 4th scenario (Case 7 consecutive cracked teeth)

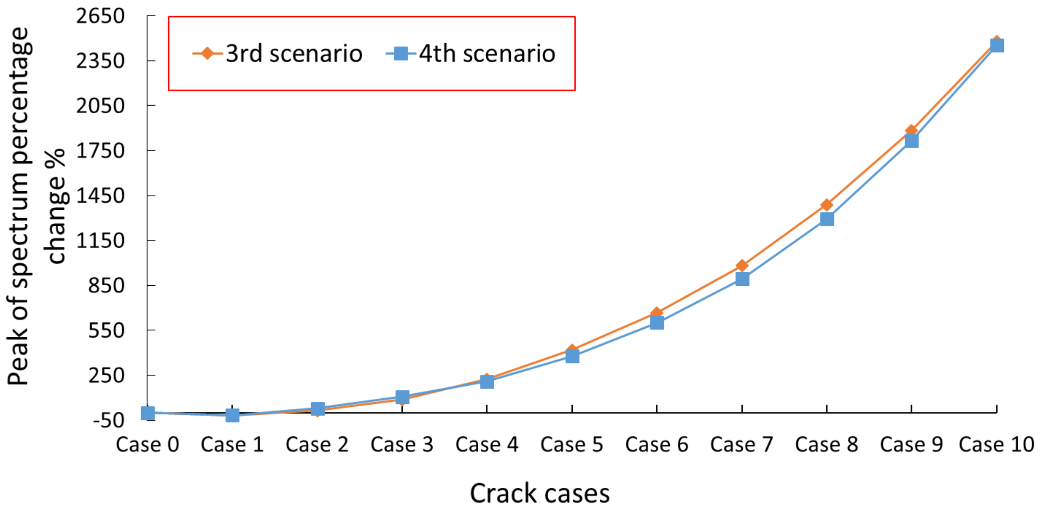

Figure 130: Percentage change in the peak of the residual signal spectrum for the 3rd and 4th scenarios

It can be concluded from this chapter that the spectral amplitude is more sensitive than all the studied time domain statistical parameters. In addition, it can be seen from the spectra of the proposed scenarios that more peaks are obtained when the cracked teeth are nonconsecutive than the case of consecutive cracks.

Chapter 7. CONCLUSIONS AND FUTURE WORK

7.1 Conclusions

In this study, a numerical model was developed and tuned to analyze the dynamic behavior of a one-stage gearbox with external spur gears having an involute tooth profile. A set of MATLAB codes were utilized to generate the gears teeth profile, perform the contact analysis, and evaluate the contact ratio. The variable gear mesh stiffness with respect to the angular position was obtained using a FEM, with SolidWorks. The total mesh stiffness was then utilized in a simplified six degrees of freedom nonlinear lumped parameter model to simulate the vibration response of the gears. First, various time-domain statistical parameters were extracted from the original and the residual vibration signals, where the gear was kept healthy, and that a single crack was supposed to appear on the pinion. The results of this model were verified at three stages. First, the contact ratios obtained from the contact analysis were compared with the theoretical values and almost exact numbers were achieved. Then, the gear mesh stiffness of both, a healthy and cracked pinion, were compared with those presented in other research articles and the results were found in good agreement. In the third stage, the values of the statistical indicators applied on both the time and frequency domains at different crack level percentages were verified with a published work.

For a more realistic investigation, multiple simultaneous cracks were introduced to the pinion. Four different multiple crack scenarios were considered in this study. The first scenario simulates the effect of the number of multiple cracks, a total of seven cracks, with the same CLP located in nonconsecutive teeth. The second scenario is similar to the first scenario, but it considers the possibility of having consecutive cracks. On the other hand, both the third and fourth scenarios study the effect of the number of cracks with different severity, but the fourth scenario simulates consecutive cracks. The gear mesh stiffness of these scenarios was calculated and inserted in the dynamic model to get the vibration responses. The sensitivity of the previously mentioned indicators was again investigated.

The results show that those parameters have different sensitivity and trends based on the number of cracks, the cracks severity, and whether they are consecutive or nonconsecutive. For the first and second scenarios, most of the parameters values were decreasing as the number of cracked teeth increases. However, the RMS value kept increasing as the number of cracks increases, and the peak value was not significantly affected as the CLP was constant. Looking at the third and fourth scenarios results, it can be concluded that almost all the indicators increases at first due to the effect of the crack severity but then they start decreasing again as the number of cracks further increase. Exempt from that, the RMS and peak amplitude which were increasing with respect to the growth in severity and number of cracks. It can be observed that the effect of the number of cracks on the statistical indicator parameters is more significant, resulting in a dramatic decrease in the sensitivity of the indicators to the crack severity. Therefore, the time-domain statistical parameters could be misleading if not considered appropriately, as their trends and values vary according to the scenario studied.

Finally, the peak and the number of sidebands for the frequency domain signal applied to the original and residual signal were investigated. The peak of the residual signal spectrum for the first two scenarios was found to be increasing linearly with the number of cracks. However, looking at the peak value for the third and fourth scenarios was increasing with approximately a third degree polynomial trend. It was observed that the number of peaks in the residual spectrum of the second scenario, between 4 and 5 kHz, can be utilized to predict the number of consecutive cracks. This study has the potential to improve the early detection of gear tooth cracks as it was found that the spectral amplitude indicator is the most sensitive to the number and severity of cracks.

7.2 Future Work and Recommendations

The following recommendations are suggested as future work for this study which can support the conclusions stated and also add to this knowledge area of gear tooth cracks detection.

- Conducting time-frequency and cepstrum analysis to get more information about the faults
- Validating the results obtained in this study by experimental work
- Studying other crack propagation scenarios with multiple cracks
- Investigating multiple cracks located on both the gear and the pinion, such as the case of coincidence when a cracked tooth on the pinion meets with a cracked tooth on the gear
- Using expert systems (Artificial Neural Network or Fuzzy Logic) to predict the gear faults
- Studying other wear types like chipped or missing teeth
- Considering the effect of lubrication and realistic mesh damping in the model

REFERENCES

[1] "Gearboxes | North East Garages," 2016. [Online]. Available: http://www.negarages.co.uk/gearboxes.html. [Accessed: 22-Apr-2016].

[2] "KHK - Gear manufacturer," 2016. [Online]. Available: http://khkgears.net/. [Accessed: 22-Apr-2016].

[3] J. R. Davis, *Gear Materials, Properties, and Manufacture*, 1st ed. Materials Park, Ohio: ASM International, 2005.

[4] "Spur Gears, Hewitt-Topham.co.uk," 2016. [Online]. Available: http://www.hewitt-topham.co.uk/spur-gears.html. [Accessed: 25-Apr-2016].

[5] "Gear Set Types," 2016. [Online]. Available: https://people.rit.edu/afeme/igd/gearsets.html. [Accessed: 25-Apr-2016].

[6] G. M. Maitra, *Handbook of Gear Design*, 1st ed. New Delhi: Mc. Graw Hill, 1994.

[7] "Helical Gear Manufacturer," 2016. [Online]. Available: http://www.prakashgears.com/helical-gears.htm. [Accessed: 25-Apr-2016].

[8] "Gear cutting capacity | LMR Gear cutting," 2016. [Online]. Available: http://www.lmrgeartech.com/capacity. [Accessed: 25-Apr-2016].

[9] "Helical And Double Helical Gear," 2016. [Online]. Available: http://www.indiabizclub.com/qxzpmd/products.php?q=;9z9zaxma9zzq05qrt;Helical+And+Double+Helical+Gear;Mumbai;engineering;India. [Accessed: 25-Apr-2016].

[10] I. Dudás, *Manufacturing geometry for constant pitch helicoidal surfaces*. Elsevier, 2004.

[11] "How Gears Work," 2000. [Online]. Available:

http://science.howstuffworks.com/transport/engines-equipment/gear5.htm. [Accessed: 25-Apr-2016].

[12] I. Law, *Gears and gear cutting*, 1st ed. England: Argus Books Ltd, 1988.

[13] “hypoid reduction gear.” [Online]. Available: http://www.pearltrees.com/franky180487/differential-reduction-gears/id10359541/item100882382. [Accessed: 16-Jun-2016].

[14] “RACK AND PINION SYSTEM,” 2016. [Online]. Available: https://iescjmechanisms.wikispaces.com/RACK+AND+PINION+SYSTEM. [Accessed: 25-Apr-2016].

[15] A. Litvin, Faydor; Fuentes, *Gear geometry and applied theory*, 2nd ed. Cambridge University Press, 1994.

[16] “Gear Profile Details.” [Online]. Available: https://pythonhosted.org/Cnc25D/gear_profile_details.html. [Accessed: 27-Apr-2016].

[17] “The Cycloid Family of Curves.” [Online]. Available: http://curvebank.calstatela.edu/cycloidmaple/cycloid.htm. [Accessed: 27-Apr-2016].

[18] S. Wu, *Gearbox Dynamic Simulation and Estimation of Fault Growth*. Edmonton: University of Alberta, 2007.

[19] P. D. McFadden, *Analysis of the vibration of the input bevel pinion in RAN Wessex helicopter main rotor gearbox WAK143 prior to failure*. Melbourne: Defence Science and Technology Organisation Aeronautical Research Laboratories, 1985.

[20] D. G. Lewicki, “Crack propagation studies to determine benign or catsatrophic

failure modes for Aerospace Thin-Rim Gears," Case Western Reserve University, 1996.

[21] D. G. Lewicki, "Gear Crack Propagation Path Studies Guidelines for UltraSafe Design," *J. Am. Helicopter Soc.*, vol. 47, no. 1, pp. 64–72, 2001.

[22] D. G. Lewicki and R. Ballarini, "Effect of Rim Thickness on Gear Crack Propagation Path," vol. 119, no. March, 1996.

[23] R. B. Randall, N. Sawalhi, and M. D. Coats, "A comparison of methods for separation of deterministic and random signals," *Int. J. Cond. Monit.*, vol. 1, no. 1, pp. 11–19, 2011.

[24] A. Parey and N. Tandon, *Fault Detection of Spur Gears Using Vibration Monitoring*. Saarbrücken, Germany: LAP Lambert Academic Publishing, 2010.

[25] I. Howard, S. Jia, and J. Wang, "The dynamic modelling of a spur gear in mesh including friction and a crack," *Mech. Syst. Signal Process.*, vol. 15, no. 5, pp. 831–853, 2001.

[26] F. Cura, A. Mura, and C. Rosso, "Investigation about crack propagation paths in thin rim gears," *Frat. ed Integrita Strutt.*, vol. 30, pp. 446–453, 2014.

[27] J. Kramberger, M. Šraml, S. Glodež, J. Flašker, and I. Potrč, "Computational model for the analysis of bending fatigue in gears," *Comput. Struct.*, vol. 82, no. 23–26, pp. 2261–2269, 2004.

[28] F. Chaari, T. Fakhfakh, and M. Haddar, "Analytical modelling of spur gear tooth crack and influence on gearmesh stiffness," *Eur. J. Mech. A/Solids*, vol. 28, no. 3, pp. 461–468, 2009.

[29] S. Wu, M. J. Zuo, and A. Parey, "Simulation of spur gear dynamics and estimation of fault growth," *J. Sound Vib.*, vol. 317, no. 3–5, pp. 608–624, 2008.

[30] O. D. Mohammed, M. Rantatalo, J. O. Aidanpää, and U. Kumar, “Vibration signal analysis for gear fault diagnosis with various crack progression scenarios,” *Mech. Syst. Signal Process.*, vol. 41, no. 1–2, pp. 176–195, 2013.

[31] X. Tian, *Dynamic Simulation for System Response of Gearbox Including Localized Gear Faults*. Edmonton: University of Alberta, 2004.

[32] Z. Chen and Y. Shao, “Dynamic simulation of spur gear with tooth root crack propagating along tooth width and crack depth,” *Eng. Fail. Anal.*, vol. 18, no. 8, pp. 2149–2164, 2011.

[33] O. D. Mohammed, M. Rantatalo, and U. Kumar, “Analytical Crack Propagation Scenario for Gear Teeth and Time-Varying Gear Mesh Stiffness,” vol. 6, no. 8, pp. 1106–1111, 2012.

[34] W. Yu, Y. Shao, and C. K. Mechefske, “The effects of spur gear tooth spatial crack propagation on gear mesh stiffness,” *Eng. Fail. Anal.*, vol. 54, pp. 103–119, 2015.

[35] H. Ma, J. Zeng, R. Feng, X. Pang, Q. Wang, and B. Wen, “Review on dynamics of cracked gear systems,” *Eng. Fail. Anal.*, vol. 55, pp. 224–245, 2015.

[36] S. Zouari, M. Maatar, T. Fakhfakh, and M. Haddar, “Three-dimensional analyses by finite element method of a spur gear: Effect of cracks in the teeth foot on the mesh stiffness,” *J. Fail. Anal. Prev.*, vol. 7, no. 6, pp. 475–481, 2007.

[37] O. D. Mohammed, M. Rantatalo, and J. O. Aidanpää, “Improving mesh stiffness calculation of cracked gears for the purpose of vibration-based fault analysis,” *Eng. Fail. Anal.*, vol. 34, pp. 235–251, 2013.

[38] D. C. H. Yang and Z. S. Sun, “A Rotary Model for Spur Gear Dynamics,” *J. Mech. Transm. Autom. Des.*, vol. 107, no. 4, pp. 529–535, Dec. 1985.

[39] S. Sirichai, *Torsional properties of spur gears in mesh using nonlinear finite element analysis*. Perth: Curtin University of Technology, 1999.

[40] R. Ma and Y. Chen, “Research on the dynamic mechanism of the gear system with local crack and spalling failure,” *Eng. Fail. Anal.*, vol. 26, pp. 12–20, 2012.

[41] O. D. Mohammed, M. Rantatalo, and J.-O. Aidanpää, “Dynamic modelling of a one-stage spur gear system and vibration-based tooth crack detection analysis,” *Mech. Syst. Signal Process.*, vol. 54–55, pp. 293–305, Mar. 2015.

[42] W. Bartelmus, “Mathematical modelling and computer simulations as an aid to gearbox diagnostics,” *Mech. Syst. Signal Process.*, vol. 15, no. 5, pp. 855–871, Sep. 2001.

[43] S. Sassi, B. Badri, and M. Thomas, “Tracking surface degradation of ball bearings by means of new time domain scalar indicators,” *Int. J. COMADEM*, vol. 11, no. 3, pp. 36–45, 2008.

[44] O. D. Mohammed and M. Rantatalo, “Performance of time domain indicators for gear tooth root crack detection and their noise-sensitivity,” in *Advances in Condition Monitoring of Machinery in Non-Stationary Operations*, vol. IV, G. Dalpiaz, Ed. Springer, 2014, pp. 303–312.

[45] L. Liu and D. J. Pines, “The Influence of Gear Design Parameters on Gear Tooth Damage Detection Sensitivity,” *J. Mech. Des.*, vol. 124, no. 4, pp. 794–804, Nov. 2002.

[46] R. M. Stewart, *Some Useful Data Analysis Techniques for Gearbox Diagnostics*. University of Southampton, 1977.

[47] O. Mohammed and M. Rantatalo, “Residual Signal Techniques Used for Gear Fault Detection,” in *Current Trends in Reliability, Availability, Maintainability*

and Safety: An Industry Perspective, Springer International Publishing, 2016, pp. 157–163.

[48] "Nomenclature and Comparative Sizes of Gear Teeth." [Online]. Available: http://www.globalspec.com/reference/68260/203279/gearing. [Accessed: 28-Apr-2016].

[49] V. Chennu, "Gear Terminology," 2015. [Online]. Available: http://me-mechanicalengineering.com/gear-terminology/. [Accessed: 01-Jan-2016].

[50] L. F. Shampine and M. W. Reichelt, "The MATLAB ODE Suite," *SIAM J. Sci. Comput.*, vol. 18, no. 1, pp. 1–22, 1997.

[51] H. Ma, X. Pang, R. Feng, R. Song, and B. Wen, "Fault features analysis of cracked gear considering the effects of the extended tooth contact," *Eng. Fail. Anal.*, vol. 48, pp. 105–120, 2015.

[52] G. Dalpiaz, A. Rivola, and R. Rubini, "Effectiveness and sensitivity of vibration processing techniques for local fault detection in gears," *Mech. Syst. Signal Process.*, vol. 14, no. 3, pp. 387–412, 2000.

APPENDIX: CONSECUTIVE CRACKS IDENTIFICATION

Spectrum of the residual signal obtained for 2nd scenario

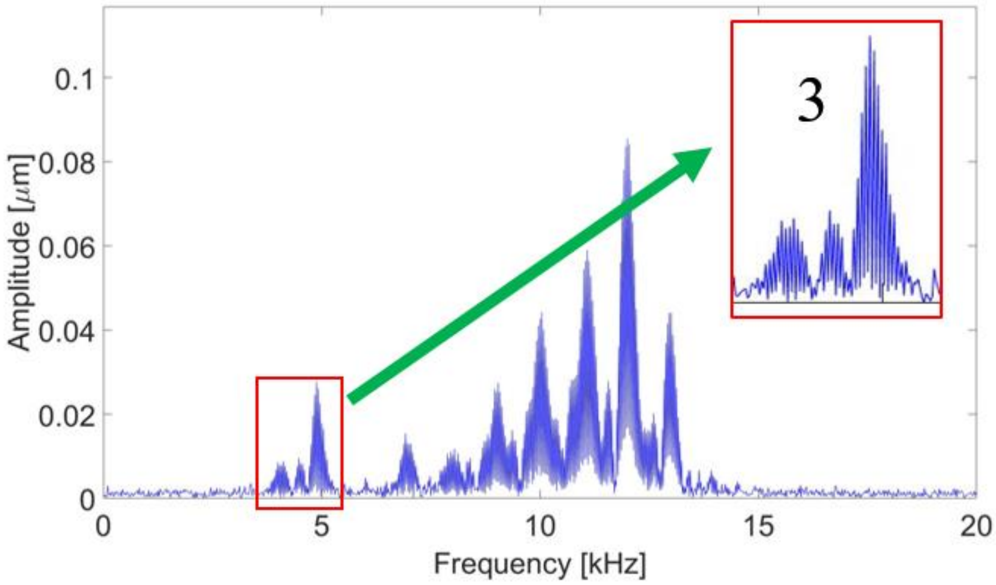

Three consecutive cracked teeth with 30% CLP

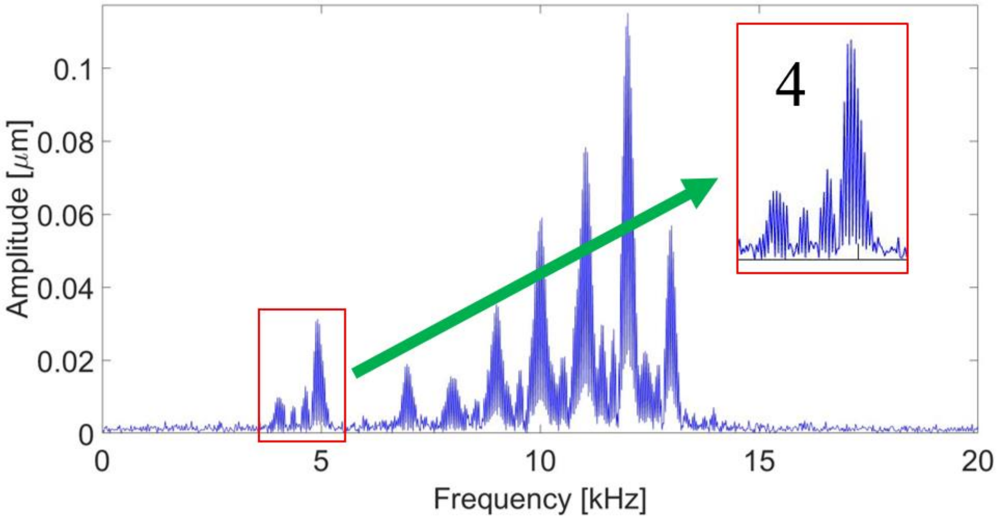

Four consecutive cracked teeth with 30% CLP

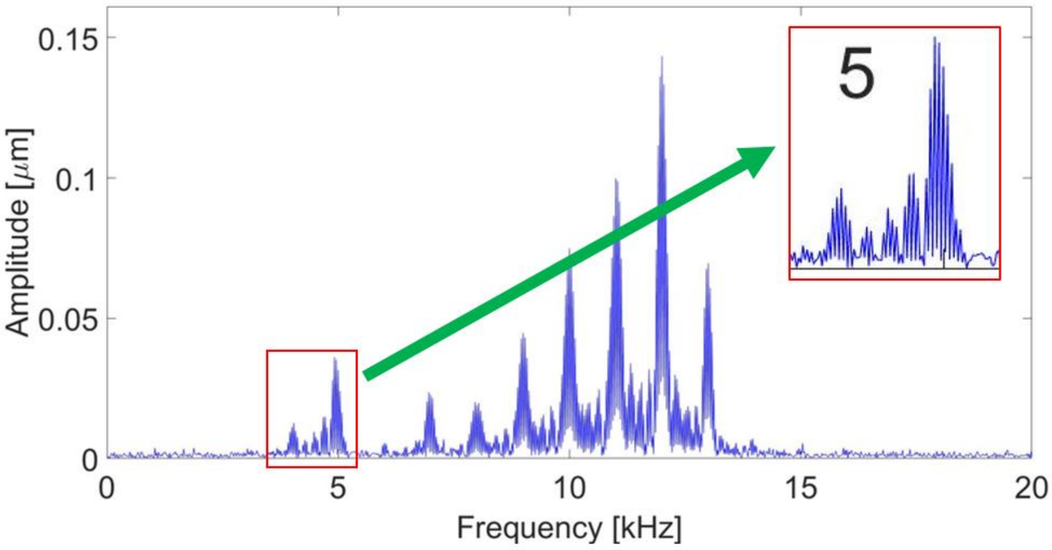

Five consecutive cracked teeth with 30% CLP

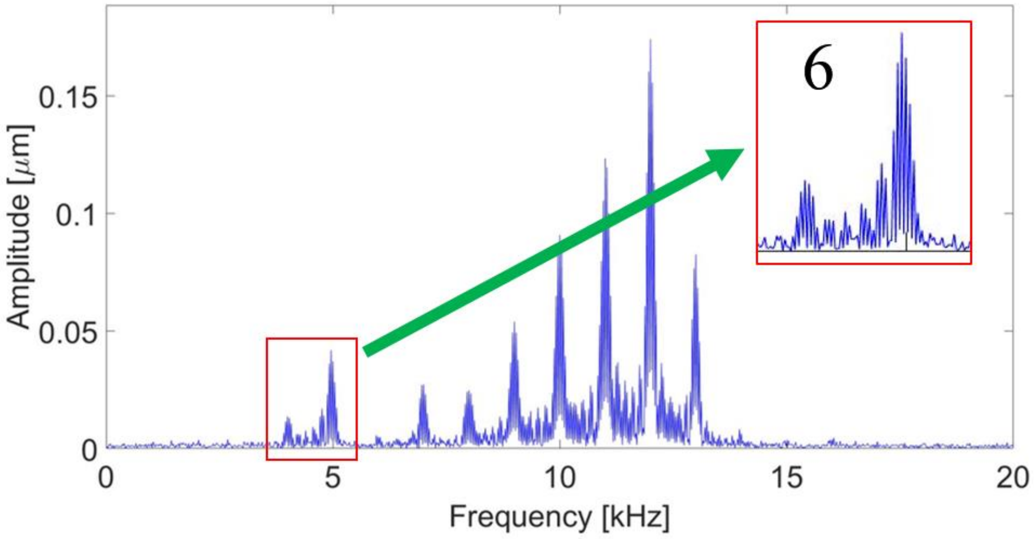

Six consecutive cracked teeth with 30% CLP